BENEMÉRITA UNIVERSIDAD AUTÓNOMA DE PUEBLA

INSTITUTO DE FÍSICA “LUIS RIVERA TERRAZAS”

“STUDY OF CRITICAL DISORDERED SYSTEMS COUPLED TO THE CONTINUUM”

TESIS

QUE PARA OBTENER EL GRADO DE

DOCTOR EN CIENCIAS (FÍSICA)

PRESENTA:

NAHUM CALDERÓN CHÁVEZ

DIRECTOR DE TESIS

DR. GIUSEPPE LUCA CELARDO

CO-DIRECTOR DE TESIS

DR. JOSÉ ANTONIO MÉNDEZ BERMÚDEZ

No. de CVU: 215570898

MARZO, 2020

Abstract

In this thesis, we study paradigmatic quantum systems coupled to external environments which can be unbounded or bounded. An unbounded external environment can be characterized by few decay channels, where the excitation can be lost. Due to the competition of the states of the system to decay in few channels of the external environment, cooperative effects such as superradiance and subradiance can be induced. Together with the coupling to an unbounded environment, we also consider a bounded external environment. Such coupling will induce a transition to a gapped regime, where the ground state is separated from the other excited states.

In order to study the effect of the coupling to external environments on quantum transport, we intend to analyze three different models.

The first model that we consider is the Power-law Banded Random Matrix (PBRM) model. The PBRM represents 1D tight-binding chains with long-range random hopping. This model shows a metal-insulator transition and a rich variety of multifractal properties at the critical point; also, due to its lower dimensionality, it is easier to analyze than other paradigmatic models having metal-insulator transitions, such as the 3D Anderson model. We investigate the effect of the coupling to a common decay channel on the structure of the eigenfunctions of the system through their multifractal dimensions. Since the coupling to a common decay channel induces a superradiant transition, we study separately the properties of superradiant and subradiant states. Our results show that the coupling to an external environment can drastically change the multifractal properties of the system.

The second model that we consider is the Picket Fence model in which the energy levels are assumed equally spaced. By coupling this model to an unbounded external environment a superradiant phase transition has been proved to occur. On the other side, by coupling this model to a bounded external environment we obtain the discrete Bardeen-Cooper-Schrieffer model of Superconductivity. We unify both situations by studying the effect of both kinds of couplings on the emergence of energy gaps in the system, which can provide robustness to disorder to the transport properties of the system.

The third model that we consider is the 1D Anderson model, which represents 1D tight-binding chains in presence of disorder characterized by the disorder strength W. Contrary to the 3D Anderson model, this model does not have a metal-insulator transition as the disorder strength W is varied. Nevertheless a finite-size transition can still be defined. For weak disorder, below of the finite-size critical disorder, the eigenfunctions of the system are delocalized and the transmission is large and weakly dependent on the disorder strength W. While above the critical disorder the eigenfunctions of the system become exponentially localized in space so that transport is exponentially suppressed with the system size. We consider the coupling of the 1D Anderson model to both an unbounded and a bounded external environments. We show how both kinds of couplings can greatly enhance the transport efficiency of this model. We also analyze the shape of the eigenfunctions on different disorder regimes for both kinds of couplings. The results presented show a non-trivial effects arising from both kinds of couplings, such as a disorder-independent transport regime.

Acknowledgments

Quiero dar las gracias al Consejo Nacional de Ciencia y Tecnología (CONACyT) por la beca otorgada para la realización del doctorado de una duración oficial de 48 meses y por la beca mixta para una estancia académica durante 9 meses en Brescia, Italia.

Agradezco a la Benemérita Universidad Autónoma de Puebla y al Instituto de Física "Ing. Luis Rivera Terrazas" por la oportunidad de continuar los estudios del doctorado y por el uso de las estaciones de trabajo donde realicé parte de los cálculos númericos presentados en esta tesis.

Tambien agradezco a mi madre Josefina y a mi esposa Linda por el apoyo de estos 7 meses de retraso.

Quiero agradecer a los miembros del Comité Revisor de la tesis: Dra. Minerva González Melchor, Dr. Eduardo Jonathan Torres Herrera y al Dr. Elías López Cruz por sus observaciones para la mejora de este trabajo y dar seguimiento a mi trabajo en los Avances de Tesis. Gracias por las comentarios del Dr. Thomas Gorin que sirvieron para mejorar significativamente el capítulo 2.

Agradezco ampliamente a mis asesores: Dr. José Antonio Méndez Bermúdez y Dr. Giuseppe Luca Celardo por su liderazgo en este trabajo de investigación y por la constante colaboración durante el doctorado.

Al Prof. Fausto Borgonovi y Francesco Mattioti de la Università Cattolica del Sacro Cuore en Brescia, Italia por la ayuda recibida y la guía durante mi estancia académica durante 9 meses.

Al personal administrativo del Instituto y en especial a la Lic. Lucrecia Hernández Ramos, Lic. Mónica Hernández Ramos por su apoyo en todos mis trámites y estar pendiente de los estudiantes y a Lic. Luis Rojas Martínez por toda la ayuda brindada para el uso óptimo de las computadoras y servidores del Instituto.

Quiero agradecer a mis amigos Lili, Lalo, Pedro Luis, Jerónimo y Luis Carlos y también agradecer a parte de mi familia Israel, Yazmin, Fabiola y Absalón.

Finalmente, deseo dar los agradecimientos más importantes, sinceros y amorosos para Jatziri, Sarai, Josefina, Angela y Linda por su amor sincero, comprensión y apoyo incondicional durante esta etapa.

Quiero poner como recordatorio en este trabajo, fue mi culpa y aprendí de mi error. Estoy agradecido con todas ustedes por siempre.

Dedicado a mi familia y especialmente a mi esposa Linda

Contents

Chapter 1

Introduction

Understanding the quantum transport regime is fundamental for developing quantum devices, such as building efficient quantum channels for energy transport, harvesting sun light more efficiently or creating dissipative-less energy transmission. For these reasons quantum transport is at the center of investigations in a vast variety of fields, such as in exciton devices [1], light-harvesting devices [2], cold atomic clouds [3] and mesoscopic devices [4].

One of the main interest in the field of quantum transport is the analysis of transport properties of a quantum system in presence of a coupling to external environments. These external environments can be present in realistic situations such as light-harvesting complexes [2] or ion-trap experiments [5], but they can also be present in engineered quantum systems in order to control their transport properties, such as in molecular chains in optical cavities [6].

The interaction with external environments can change the transport properties of quantum systems in a dramatic way. In particular, an external environment can mediate long-range interactions between the components of a quantum system.

In this thesis, we study paradigmatic quantum systems coupled to external environments which can be unbounded or bounded. An unbounded external environment can be characterized by few decay channels, where the excitation can be lost. Due to the competition of the states of the system to decay in few channels of the external environment, cooperative effects such as superradiance and subradiance can be induced. Superradiance indicates the existence of collective states which decay very fast into the environment, much faster than the single components of a given system. Subradiance indicates the opposite effect, where collective states decay very slowly into the environment. Such effects have been found experimentally in many realistic systems [6, 7]. A transition to a superradiant regime can be induced as the intensity of the coupling with the external environment is tuned. Thus the presence of an unbounded external environment enrich the phase diagram of the system considerably. Specifically, the coupling to an unbounded environment will also induce a non-Hermitian long-range hopping in the system which can sensibly affect its transport properties. Indeed, an excitation or particle can be lost in the unbounded external environment and it can also be re-absorbed by a far way site.

Together with the coupling to an unbounded environment, we also consider a bounded external environment, such as the coupling to a cavity mode [1]. Such coupling will induce a transition to a gapped regime, where the ground state is separated from the other excited states. Also the coupling to a bounded external environment can induce a long-range Hermitian interaction in the system, with several consequences of its transport properties. Indeed, in a chain coupled to a one mode cavity with large wavelength, the cavity mode acts as an external site coupled to all the sites of the chain. This external site induces an effective all-to-all hopping between the sites of the chain.

In order to study the effect of the coupling to external environments on quantum transport, we

intend to analyze three different models.

The first model that we consider is the Power-law Banded Random Matrix model (PBRM) [8, 9]. The PBRM represents 1D tight-binding chains with long-range random hopping. This model presents several interesting features: it shows a metal-insulator transition and a rich variety of multifractal properties at the critical point; also, due to its lower dimensionality, it is easier to analyze than other paradigmatic models having metal-insulator transitions, such as the 3D Anderson model [10]. For these reasons this model has attracted a lot of attention in the previous years [8, 9, 11, 12]. Nevertheless the effect of opening the system by coupling it to an unbounded environment has never been studied with respect to its multifractal properties. In Chapter 2 we aim to do precisely this. We investigate the effect of the coupling to a common decay channel on the structure of the eigenfunctions of the system through their multifractal dimensions. Since the coupling to a common decay channel induces a superradiant transition, we study separately the properties of superradiant and subradiant states. Our results show that the coupling to an external environment can drastically change the multifractal properties of the system.

The second model that we consider is the Picket Fence model in which the energy levels are assumed equally spaced. By coupling this model to an unbounded environment a superradiant phase transition has been proved to occur [13]. On the other side, by coupling this model to a bounded environment we obtain the discrete Bardeen-Cooper-Schrieffer model of Superconductivity [14]. In this sense this model is perfect to study the coupling to both an unbounded and bounded environments since both situations have been already considered in the literature. In Chapter 3 we unify both situations by studying the effect of both kinds of couplings on the emergence of energy gaps in the system. The results of Chapter 3, which highlight a formal analogy between superradiance and superconductivity, have been recently published in Ref. [15].

The third model that we consider is the 1D Anderson model [16], which represents 1D tight-binding chains in presence of disorder characterized by the strength W. Contrary to the 3D Anderson model, this model does not have a metal-insulator transition as the disorder strength is varied. Nevertheless a finite-size transition can still be defined. For weak disorder, below of the finite-size critical disorder, the eigenfunctions of the system are delocalized and the transmission is large and weakly dependent on the disorder strength W. While above the critical disorder the eigenfunctions of the system become exponentially localized in space so that transport is exponentially suppressed with the system size. In Chapter 4 we consider the coupling of the 1D Anderson model to both an unbounded and a bounded environments. Both kinds of environments can induce a long-range interaction in the system: a non-Hermitian long-range hopping for the case of the coupling to an unbounded environment and a long-range Hermitian hopping for the case of the coupling to a bounded environment. We show how both kinds of couplings can greatly enhance the transport efficiency of this model.

Recently the interplay of disorder and superradiance has been analyzed in a 1D and 3D Anderson models attached to one decay channel [16]. In such models two transitions are present: a metal-insulator transition induced by disorder and a superradiant transition induced by the coupling to the external environment. Remarkably, it was noted that superradiant and subradiant states respond to disorder in different ways: while subradiant states behave similarly to those of the isolated system, the superradiant states show robustness to disorder and become localized only when the disorder is comparable with their decay widths. Moreover, also the effect of a bounded environment inducing a long-range Hermitian hopping has been considered in the literature in the framework of the Anderson model [17]. It was shown that the presence of long-range hopping in a 1D Anderson model can induce energy gaps and novel cooperative effects, such as *Cooperative Shielding*. These energy gaps can provide robustness to disorder to the transport properties of the system. In Chapter 4, the effect on the transport properties of the 1D Anderson model are analyzed in detail as the coupling with the external environment and the disorder are changed. We also analyze the shape of the eigenfunctions on different disorder regimes for both kinds of couplings. This detailed study has never been done

before and the results presented in this Chapter clearly show the non-trivial effects arising from both kinds of couplings, such as a disorder-independent transport regime.

Chapter 2

PBRM model at criticality coupled to one common channel

Quantum transport is often analyzed in lattice models where an excitation or particle can hop from site to site. A well known example is the 3D Anderson model [10], where the hopping is nearest-neighbour and the site energies are random, making the system disordered. In the 3D Anderson model a metal-insulator transition (MIT) is achieved as the disorder strength is varied. Indeed below a critical disorder, the wave functions of the system are extended and transport is either ballistic or diffusive. Above such critical disorder, the wave functions become exponentially localized in space and transport is exponentially suppressed with the system size. At the critical disorder, the eigenfunctions display a multifractal structure [18, 19, 20].

The multifractal structure of the states is usually quantified by its multifractal dimensions D_q. From these multifractal dimensions, the correlation dimension D_2 plays the most relevant role as it manifests in physical observables. As examples of this observables we can quote the conductance distribution [21, 22], the wave packet dynamics and the diffusion coefficient [23].

Recently, the interplay of disorder and superradiance has been analyzed in a 3D Anderson model attached to one decay channel [16]. In such model, two transitions are present: a metal-insulator transition induced by disorder and a superradiant transition induced by the coupling to the external environment. Remarkably it was noted that superradiant and subradiant states respond to disorder in different ways: while subradiant states behave similarly to those of the isolated system, superradiant states show robustness to disorder and become localized only when disorder is comparable with their decay widths.

In order to analyze the interplay of the multifractal dimensions with the coupling at the MIT, we will study a different model: the Power-law Banded Random Matrix (PBRM) model [8, 9]. We will analyze in detail this model in the following section.

2.1 PBRM model

The PBRM model describes one dimensional (1D) tight-binding chains of length N with long-range random hoppings. This model is represented by $N \times N$ real symmetric random matrices whose elements are statistically independent random variables characterized by a normal distribution with

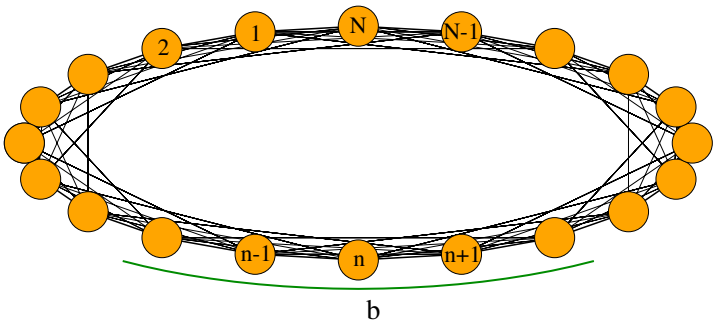

Figure 2.1: Scheme of periodic PBRM model with N sites where each site, indicated by orange circles, is coupled with all others; i.e., the hopping is of infinite range. The parameter b modulates the random long-range interaction. Here $b \sim 2$.

zero mean and a variance given by $\langle |H_{mm}|^2 \rangle = 1$ and

$$\langle |H_{mn}|^2 \rangle = \frac{1}{2} \frac{1}{1 + [\sin(\pi |m-n|/N)/(\pi b/N)]^{2\mu}} \,. \tag{2.1}$$

Here, μ and b are the model parameters. The PBRM model of Eq. (2.1) is in its periodic version; i.e., the 1D chain is in a ring geometry. In Fig. 2.1 we show a scheme of the PBRM model with N sites where the hopping is of infinite range but modulated by the parameter b. Indeed, as in realistic physical systems, the hopping amplitudes decrease with the distance between components.

The PBRM model, as shown in Eq. (2.1), depends on the two control parameters μ and b. The power-law decay μ induces a disorder-driven metal-insulator transition (MIT) [8, 9, 11, 12, 24, 25, 26, 27]: When $\mu > 1$ ($\mu < 1$) the PBRM model is in the insulating (metallic) phase, so its eigenstates are localized (delocalized); here the MIT occurs at $\mu = 1$. Indeed, it has been shown [8, 28, 29, 30, 31, 32, 33, 34] that the PBRM model exhibits a broad spectrum of critical properties at the MIT. Regardless of the value of μ, the effective bandwidth b remains as a free parameter able to tune the localization properties of the PBRM model.

One of the most relevant characteristics of the PBRM model at the MIT is that its eigenstates are multifractal objects. Indeed, at the MIT, the eigenstates of the PBRM model may transit from strong multifractals to weak multifractals [8, 12] by moving the bandwidth form $b \ll 1$ to $b \gg 1$, respectively, with $b \in (0, \infty)$.

In the following, we will focus on the PBRM model at criticality, i.e., we fix $\mu = 1$ and consider the parameter b as a free parameter.

The multifractality of the normalized eigenstates Ψ of the PBRM model can be characterized by the set of multifractal dimensions D_q, which are defined by the scaling of the inverse of the average participation numbers of the eigenstates with the chain size N [29]:

$$\left\langle \sum_{i=1}^{N} |\Psi_i|^{2q} \right\rangle \sim N^{-(q-1)D_q}, \tag{2.2}$$

where $\langle \cdots \rangle$ is the average over some eigenstates on an energy window and over random configurations of the PBRM model. Let us note, the normalized eigenstates Ψ of the PBRM model form an orthonormal basis. For strongly localized eigenstates the participation numbers do not scale with the system size N, i.e., $D_q \to 0$ for all q; while extended states always feel the entire system, i.e. $D_q \to d$ for all q where d is the dimension of the system, which for the PBRM model is $d = 1$. However, notice that

D_1, the so called information dimension, cannot be computed from Eq. (2.2). D_1 is defined through the scaling of the average information entropy with the logarithm of the system size N [28]:

$$\left\langle -\sum_{i=1}^{N} |\Psi_i|^2 \ln |\Psi_i|^2 \right\rangle \sim D_1 \ln N. \tag{2.3}$$

One of the goals of this thesis project is to study the effects that the *opening* of the PBRM model to an external environment has on the multifractal properties of the eigenstates. We approach this problem by analyzing the multifractal dimensions D_q of an *open* PBRM model in two different scattering setups: One in which all sites of the chain, represented by the PBRM model, are attached to a common one-mode channel, and a second one in which one site of the chain is coupled to a one-mode channel.

2.2 Open quantum systems

Open quantum systems can be modeled using the non-Hermitian effective Hamiltonian approach [35, 36] in which a discrete quantum system is coupled to an external environment characterized by a continuum of states. The coupling to the continuum induces a decay width Γ in the discrete states of the internal system. Here, Γ is inversely proportional to the lifetime $\tau \sim 1/\Gamma$. When the coupling is small, all the eigenstates acquire a decay width Γ proportional to the amplitude of the coupling strength γ. As the coupling is increased, a critical value is reached where the decay widths structure suffer a significant change and the system shows maximal coupling to the external environment. Above this critical value, some eigenstates have a non-zero decay width Γ_{SR} (known as superradiant states) while the other states have a decay width Γ_{Sub} which is approximately zero (subradiant states). This phenomena is called superradiance transition (ST) [37].

As stated above, the coupling to the continuum can be taken into account by the non-Hermitian effective Hamiltonian H_{eff}. We present a standard derivation of H_{eff} [36].

Let us consider a discrete quantum system P, interacting with another system Q, which represents the external environment. We assume that the subspace P is spanned by N_P discrete states $|i\rangle$, while the subsystem Q by N_q states $|c, E\rangle$, where $c = 1, \ldots, M$ is a discrete quantum number, labeling the decay channels, and E is another discrete quantum number, representing the energy (we will take the continuum limit of this quantum number later).
Let us consider the projectors, within the Hilbert space of the total system $P+Q$, on the two subsystems:

$$P = \sum_{i=1}^{N_P} |i\rangle \langle i| , \quad Q = \sum_{c=1}^{M} \sum_{E=1}^{N_Q} |c, E\rangle \langle c, E| . \tag{2.4}$$

Under the orthogonality conditions $\langle i|j\rangle = \delta_{i,j}$, $\langle c, E|c', E'\rangle = \delta_{c,c'}\delta_{E-E'}$, $\langle i|c, E\rangle = 0$, we can rewrite the total Hamiltonian of the system as

$$H = H_0 + V = \begin{pmatrix} \mathrm{H}_{PP} & 0 \\ 0 & \mathrm{H}_{QQ} \end{pmatrix} + \begin{pmatrix} 0 & \mathrm{H}_{PQ} \\ \mathrm{H}_{QP} & 0 \end{pmatrix} , \tag{2.5}$$

where $H_{PP} = PHP$, $H_{PQ} = PHQ$ and similarly for the other terms.
Using Eq. (2.5) and the fact that $|\Psi\rangle = (P + Q)|\Psi\rangle$, the stationary Schrödinger equation for the total system read as

$$(H_{PP} + H_{QQ} + H_{PQ} + H_{QP})|\Psi\rangle = E(P + Q)|\Psi\rangle . \tag{2.6}$$

Using the properties of the operators, namely: $PP = P$, $QQ = Q$, $PQ = QP = 0$, Eq. (2.6) is

$$(E - H_{PP})P|\Psi\rangle + (E - H_{QQ})Q|\Psi\rangle = H_{PQ}Q|\Psi\rangle + H_{QP}P|\Psi\rangle . \tag{2.7}$$

From multiplication of Eq. (2.7) by P and Q from the left, we obtain respectively

$$(E - H_{PP})P\,|\Psi\rangle = H_{PQ}Q\,|\Psi\rangle \tag{2.8}$$
$$(E - H_{QQ})Q\,|\Psi\rangle = H_{QP}P\,|\Psi\rangle\ . \tag{2.9}$$

Our main purpose is to write the Schrödinger equation (2.6) projected into the internal subspace, so we have to eliminate the states, $Q\,|\Psi\rangle$. In order to do this, from Eq. (2.9) we get $Q\,|\Psi\rangle = (E - H_{QQ})^{-1}H_{QP}P\,|\Psi\rangle$, we put into Eq. (2.8). This substitution leads to

$$H_{\text{eff}}P\,|\Psi\rangle = EP\,|\Psi\rangle\ , \tag{2.10}$$

where

$$H_{\text{eff}} = H_{PP} + H_{PQ}\frac{1}{E - H_{QQ} + i\epsilon}H_{QP} \tag{2.11}$$

is the effective Hamiltonian, which can be written in an explicit form considering the orthogonality conditions of the states in the subsystems P and Q. Without loss of generality, we assume that the total Hamiltonian is diagonal on the subsystem Q:

$$\langle c, E|H|c', E'\rangle = E\delta_{c,c'}\delta_{E-E'}\ .$$

Using the projectors, Eq. (2.4), we have

$$H_{\text{eff}} = \sum_{i,j}|i\rangle\,\langle i|H|j\rangle\,\langle j| + \sum_{c,E'}\sum_{i,j}|i\rangle\,\langle i|H|c,E'\rangle\,\frac{1}{E - E' + i\epsilon}\,\langle c,E'|H|j\rangle\,\langle j|\ .$$

Let us now define the transition amplitudes between the discrete states of the internal subsystem P and the states of the environment Q:

$$A_i^c(E') = \langle i|H|c,E'\rangle\ . \tag{2.12}$$

Taking the continuum limit

$$\sum_{c,E'} \to \sum_c \int dE'$$

and using the identity

$$\lim_{\epsilon\to 0^+}\int dx\frac{f(x)}{x \pm i\epsilon} = \text{Pv}\int dx\frac{f(x)}{x} \mp i\pi f(0)\,,$$

the non-Hermitian Hamiltonian can be written as

$$H_{\text{eff}}(E) = H_{PP} + \Delta(E) \mp \frac{i}{2}Q(E)\,, \tag{2.13}$$

where

$$Q_{i,j}(E) = 2\pi\sum_c\int dE'\,A_i^c(E')(A_j^c(E'))^*\delta(E - E') = 2\pi\sum_c A_i^c(E)(A_j^c(E))^*$$

and

$$\Delta_{i,j}(E) = \sum_c \text{Pv}\int dE'\frac{A_i^c(E')(A_j^c(E'))^*}{E - E'}\,,$$

In what follows, we neglect the second Hermitian term in Eq. (2.13) because our interest is at the middle of the energy spectrum, where this term vanishes and we also neglect the E-dependence to simplify the Eq. (2.13).

So, the components of Eq. (2.13) read as follows

$$(H_{\text{eff}})_{k,l} = (H_{PP})_{k,l} - \frac{i}{2}\sum_{c(open)} A_k^c (A_l^c)^* \,, \tag{2.14}$$

where H_{PP} is the Hermitian Hamiltonian of the internal quantum system, which in our study is the PBRM model. The A_k^c are the transition amplitudes from the discrete states $|k\rangle$ to the continuum channels c. In this work, we have one decay channel, $c = 1$, and the coupling strength are equal, so that $A_k^1 = \sqrt{\gamma}$. Thus Eq. (2.14) can be written as

$$H_{\text{eff}} = H_0 - i\frac{\gamma}{2}Q \,, \tag{2.15}$$

where the matrix Q accounts for the external environment and H_0 is the Hamiltonian of the isolated system. The structure of the matrix Q is determined according to the different scattering setups.

The corresponding eigenstates $|r\rangle$ and $\langle\tilde{r}|$ of the non-Hermitian Hamiltonian form a bi-orthogonal basis:

$$H_{\text{eff}}\,|r\rangle = \mathcal{E}_r\,|r\rangle \quad \langle\tilde{r}|\,H_{\text{eff}} = \langle\tilde{r}|\,\mathcal{E}_r^* \,, \tag{2.16}$$

and its eigenenergies are complex numbers with the form

$$\mathcal{E}_r = E_r - \frac{i}{2}\Gamma_r \,, \tag{2.17}$$

corresponding to resonances centered at the energy E_r with the decay widths Γ_r; i.e. the quantity commonly used to study the transition to superradiance. Since H_{eff} is non-Hermitian, let us define the "non-Hermitian bra" as the transpose of the $|r\rangle$, i.e. $\langle r| := |r\rangle^t$ and $\Psi_i = \langle i|r\rangle$. We can rewritten the Eqs. (2.2) and (2.3) as

$$I_q \equiv \left\langle \sum_{i=1}^{N} |\Psi_i|^{2q} \Big/ \left|\sum_{i=1}^{N} |\Psi_i|^2\right|^q \right\rangle \sim N^{-(q-1)D_q} \tag{2.18}$$

and

$$I_1 \equiv \left\langle -\sum_{i=1}^{N} |\Psi_i|^2 \ln\left[|\Psi_i|^2 \Big/ \left|\sum_{i=1}^{N} |\Psi_i|^2\right|\right] \Big/ \left|\sum_{i=1}^{N} |\Psi_i|^2\right| \right\rangle \sim D_1 \ln N. \tag{2.19}$$

Note, $\sum_{i=1}^{N} |\Psi_i|^2 = 1$ for the Hermitian Hamiltonian. On the other hand for the non-Hermitian Hamiltian, this normalization represents the conditional probability to find an excitation in the system on a specific site, given that the excitation is found in the system and not in the unbounded external environment.

2.3 Scattering setups

As already mentioned above, in this work we consider two scattering setups:

- Scattering setup A: All sites of the chain, represented by the PBRM model, are coupled to a common one-mode channel; see Fig. 2.2. Here, the matrix Q in Eq. (2.15) is defined as $Q_{i,j} = 1$ $\forall\, i, j$.

- Scattering setup B: One site of the chain, represented by the PBRM model, is coupled to a one-mode channel; see Fig. 2.3. Here, the matrix Q in Eq. (2.15) is defined as $Q_{i,j} = \delta_{i,1}\delta_{j,1}$. Note that, since the chain represented by the PBRM model is in a ring geometry, all sites are *equivalent* bulk sites; so we can choose any site to attach the one-mode channel.

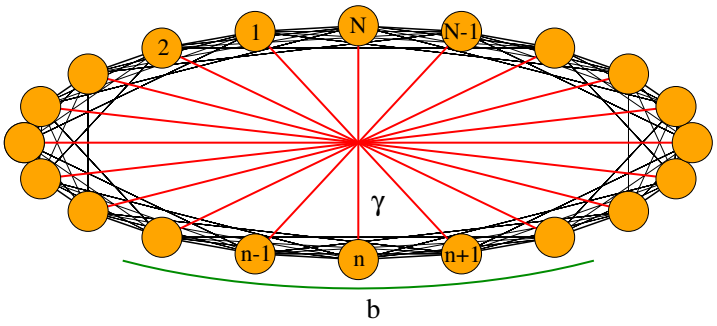

Figure 2.2: Scattering setup A: All sites of the chain, represented by the PBRM model, are coupled to a common one-mode channel, indicated by the red lines, with a coupling strength γ and the parameter b modulates the random long-range interaction.

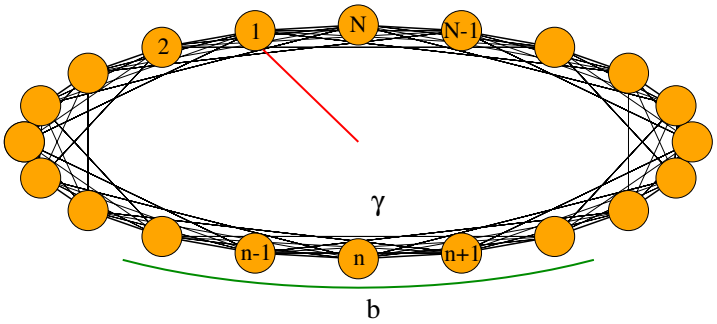

Figure 2.3: Scattering setup B: One site of the chain, represented by the PBRM model, is coupled to a one-mode channel, indicated by the red line, with a coupling strength γ and the parameter b modulates the random long-range interaction.

Since in both scattering setups we have only one-mode channel coupled to the chain, we expect only one superradiant state while the rest $N-1$ states become subradiant states above the superradiance transition.

Therefore, below, to study the transition to superradiance for the PBRM model in the two scattering setups, we use exact numerical diagonalization of the non-Hermitian effective Hamiltonian H_{eff} in Eq. (2.15) to obtain the average decay widths $\langle\Gamma\rangle$ from the imaginay part of the complex eigenvalues $\mathcal{E}$ of large ensembles of H_{eff} characterized by the set of parameters (γ, b, N). Note, the symbol $\langle\ldots\rangle$ indicates average over the disorder configurations, in addition to the average over the subradiant states.

We show the error bars of the average decay widths $\delta\Gamma$ in all simulations of $\langle\Gamma\rangle$ even if in some cases they are not visible since they are too small. The error bars $\delta\Gamma$ were computed from the standard deviation of the mean, i.e. $\delta\Gamma = \sigma_\Gamma/\sqrt{N_E}$ where σ_Γ is the standard deviation of the decay widths distribution and N_E is the size of the ensemble.

2.3.1 Preliminar analysis

2.3.1.1 Scattering setup A

On the one hand, when all sites of the chain are coupled to a common one-mode channel, the sum over all the decay widths Γ is equal to $N\gamma$ [16], i.e.,

$$\sum_{i=1}^{N} \Gamma_i = N\gamma \,,$$

thus

$$\langle \Gamma \rangle = \frac{1}{N} \sum_{i=1}^{N} \Gamma_i = \gamma \,, \tag{2.20}$$

i.e., the average of the all decay widths Γ equals the coupling strength γ and it is valid for all the couplings strength γ. Above the superradiance transition (ST), the superradiant state acquires all the decay width and the average decay width $\langle \Gamma \rangle_{\rm SR}$ is approximately equal to the coupling amplitude $N\gamma$, while the decay widths for the $N-1$ subradiant states are approximately zero and the average decay width $\langle \Gamma \rangle_{\rm Sub}$ is proportional to the inverse of the coupling strength γ.

The average decay width of the superradiant state $\langle \Gamma \rangle_{\rm SR}$ is the average of the largest decay width Γ of all the states for each random configuration, while the average of the $N-1$ subradiant states $\langle \Gamma \rangle_{\rm Sub}$ is the average of the remaining $N-1$ decay widths Γ in such random configuration.

Then, in Fig. 2.4, we show the average of the resonance widths $\langle \Gamma \rangle$ for both subradiant states and the superradiant state as a function of the coupling strength γ for the scattering setup A. Here, we used a chain of size $N = 1024$ and the parameters $b = \{0.01, 0.1, 1, 10, 100\}$. Recall that the states of the corresponding closed PBRM model are strong multifractals (almost localized states) for $b \ll 1$ and weak multifractals (almost extended states) for $b \gg 1$. We also include the case of the Gaussian Orthogonal Ensemble [1] (GOE) that we will use as reference since it is expected to be reproduced when $b \to N$.

From Fig. 2.4 we can observe that the average decay width $\langle \Gamma \rangle \sim \gamma$ for all the states below the ST for any value of b, while above ST the average decay width $\langle \Gamma \rangle_{\rm Sub} \sim 1/\gamma$ and it depends on the parameter b for the subradiant states. For the superradiant state, the average decay width $\langle \Gamma \rangle_{\rm SR} \sim N\gamma$ and it is independent of the parameter b.

2.3.1.2 Scattering setup B

On the other hand, when one site of the chain is coupled to a one-mode channel, the sum over all the decay widths Γ is equal to γ [16], i.e.,

$$\sum_{i=1}^{N} \Gamma_i = \gamma \,,$$

thus

$$\langle \Gamma \rangle = \frac{1}{N} \sum_{i=1}^{N} \Gamma_i = \frac{\gamma}{N} \,, \tag{2.21}$$

[1] The GOE is a random matrix ensemble formed by real symmetric random matrices H whose entries are statistically independent random variables drawn from a normal distribution with zero mean and variance $\langle || H_{ij}|^2 |= \rangle (1+\delta_{ij})/2$, see Ref. [38]. The GOE is commonly used to statistically represent Hamiltonian matrices corresponding to complex, chaotic, or disordered systems having time-reversal invariance.

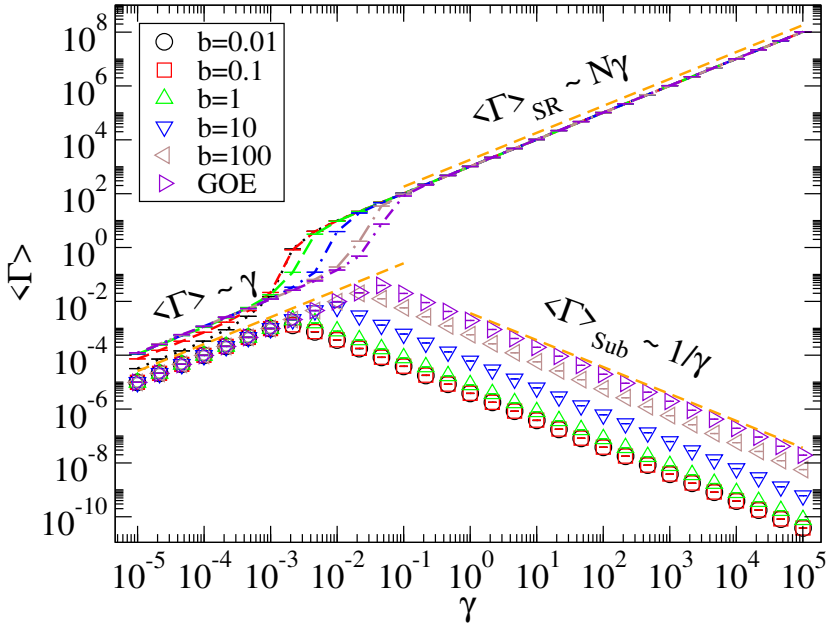

Figure 2.4: Average decay widths $\langle\Gamma\rangle$ *vs.* the coupling strength γ for the scattering setup A. Here $N = 1024$ and $b = \{0.01, 0.1, 1, 10, 100\}$. Lines and symbols are the average decay widths for the superradiant state and the subradiant states, respectively. We are also including the GOE limit. All averages are computed over 32 disorder configurations of H_{eff}.

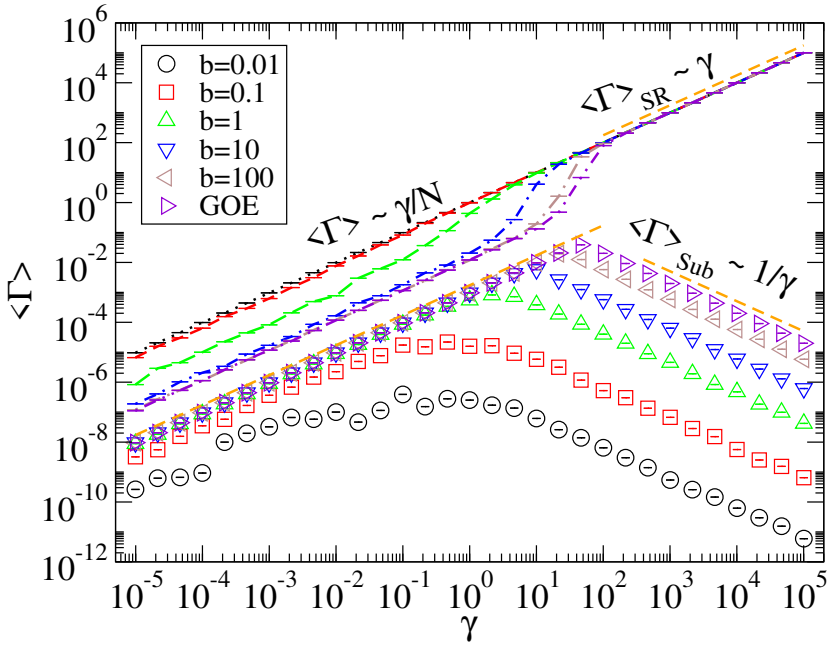

Figure 2.5: Same as in Fig. 2.4 for the scattering setup B.

i.e., the average of all the decay widths Γ equals the amplitude of the coupling strength γ normalized by the chain size N. Above the ST, the superradiant state acquires all the decay widths Γ and the average decay width $\langle\Gamma\rangle_{\rm SR}$ is approximately the coupling strength γ while the decay widths Γ for the $N-1$ subradiant states is approximately zero and the average decay widths $\langle\Gamma\rangle_{\rm Sub}$ is proportional to the inverse of the coupling strength γ.

Now in Fig. 2.5, we show the average of the resonance widths $\langle\Gamma\rangle$ for both subradiant states and the superradiant state as a function of the coupling strength γ for the scattering setup B. For comparison purposes, we use here the same parameters as in Fig. 2.4.

From Fig. 2.5 we can observe that the average decay widths $\langle\Gamma\rangle \sim \gamma/N$ for all the states below the ST with $b \geq 1$. While above ST, the average decay widths $\langle\Gamma\rangle_{\rm Sub} \sim 1/\gamma$ for the subradiant states and $\langle\Gamma\rangle_{\rm SR} \sim \gamma$ for the superradiant state as the coupling strength γ increases, like for the scattering setup A. Here, a larger coupling strength γ is needed to achieve the ST for a fixed value of b, as compared to the scattering setup A. For instance, for the scattering setup A with $b = 100$ the ST is reached for the coupling amplitude $\gamma \sim 10^{-2}$, while $\gamma \sim 10^{1}$ is needed to reach the ST for the scattering setup B.

In Fig. 2.6, we show the average resonance widths $\langle\Gamma\rangle_{\rm Sub}$ as a function of the coupling strength γ for the subradiant states for the system size $N = 1024$ and the parameters $b = \{1, 100\}$ comparing them with the Moldauer-Simonius relation [39]:

$$\langle\Gamma\rangle = \frac{D}{\pi} \ln\left|\frac{1+\kappa}{1-\kappa}\right|, \tag{2.22}$$

where D is the mean level spacing, which depends on the parameter b. We also observe that the Moldauer-Simonius relation predicts quite well the behavior of $\langle\Gamma\rangle_{\rm Sub}$ below the ST and it is slightly lower above the ST for both scattering setups. The agreement with the Moldauer-Simonius relation is good for all the parameters b considered. Note that the deviations above the ST are due to the fact that the critical coupling is not exactly $\gamma/D = 1$ but slightly larger.

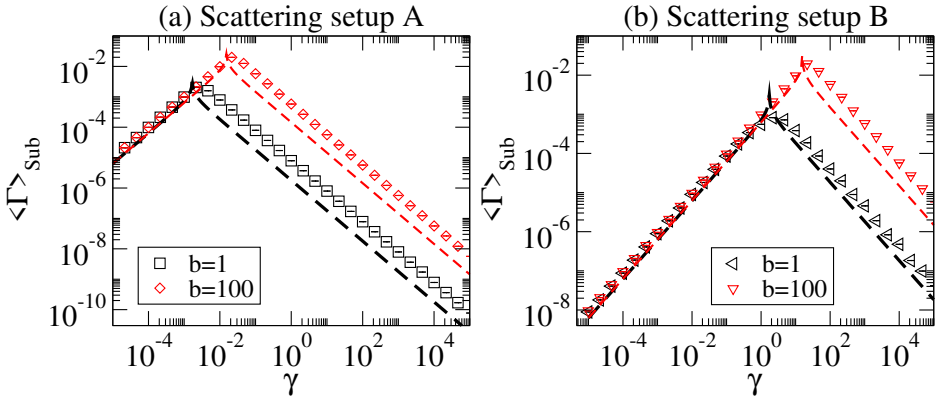

Figure 2.6: Average decay widths $\langle\Gamma\rangle_{\rm Sub}$ *vs.* the coupling strength γ for (a) the scattering setup A and (b) the scattering setup B. Here, we use the system size $N = 1024$ and the parameters $b = \{1, 100\}$. The symbols are the average decay widths for the subradiant states and the dashed lines indicate Eq. (2.22). All averages are computed over 32 disorder configurations of $H_{\rm eff}$.

The superradiant transition is expected to occur for $\langle\Gamma\rangle / D \simeq 1$ [37], where D is the mean level spacing of the isolated system represented by H_0 in Eq. (2.15). So, according to this condition and Eqs. (2.20) and (2.21) the superradiant transition for the scattering setup A occurs for

$$\frac{\langle\Gamma\rangle}{D} = \frac{\gamma}{D} \simeq 1 \,, \tag{2.23}$$

while for the scattering setup B it occurs for

$$\frac{\langle\Gamma\rangle}{D} = \frac{\gamma}{ND} \simeq 1 \,. \tag{2.24}$$

Equations (2.23) and (2.24) imply the knowledge of D for both scattering setups. Therefore, in the next subsection we will focus on it.

2.3.2 Mean level spacing

Here, in order to properly define the onset of the ST, we compute the mean level spacing D of the isolated PBRM model. D is defined as the mean distance between the neighboring eigenenergies, $D = E_{n+1} - E_n$, at the center of the energy spectrum where the density of the states is approximately constant [40].

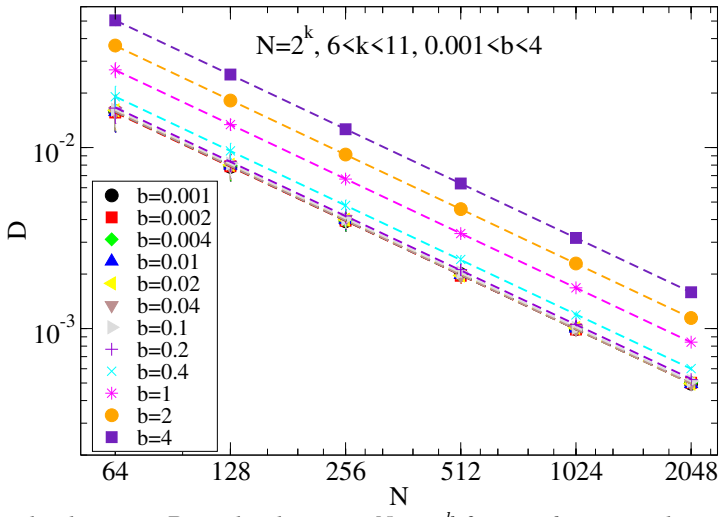

Figure 2.7: Mean level spacing D *vs.* the chain size $N = 2^k$ for $6 < k < 11$ and $0.001 \leq b \leq 4$. The dashed lines indicate linear fittings. The corresponding fitting parameters are reported in Fig. 2.9.

Then, in Figs. 2.7 and 2.8, we show the mean level spacing D as a function of the chain size N. In the range $0.001 \leq b \leq 4$ we used the chain sizes $N = 2^k$ with $6 < k < 11$ (i.e. $N = \{64, 128, 256, 512, 1024, 2048\}$, see Fig. 2.7) and for the range $10 \leq b \leq 1000$ we used $N = 2^k$ with $8 < k < 13$ (i.e. $N = \{256, 512, 1024, 2048, 4096, 8192\}$, see Fig. 2.8). [1] The mean level spacing D is performed over 2^{k-2} eigenvalues around the energy band center of 2^{15-k} disorder configurations N_r, so the ensemble size of the statistic is $N_r \times N = 2^{13}$.

[1] The error bars of the mean level spacing δD were computed from the standard deviation of the mean, i.e. $\delta D = \sigma_D / \sqrt{N_E}$ where σ_D is the standard deviation of the distribution of D and N_E is the size of the ensemble. Let us note that δD are very small for the shown results in this section.

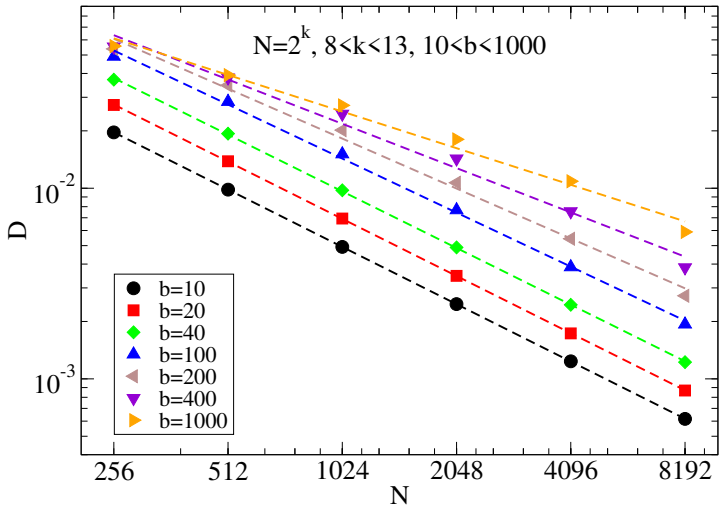

Figure 2.8: Same as in Fig. 2.7 apart of $8 \leq k \leq 13$ and $10 \leq b \leq 1000$.

As can be clearly seen from these figures, the data D *vs.* N follows power-law behavior of the type

$$D = AN^{-\alpha} \,. \tag{2.25}$$

Thus, we performed fittings of the data with Eq. (2.25), see dashed lines in Figs. 2.7 and 2.8. and report the fitting parameters in Fig. 2.9. The error bars $\delta\alpha$ and δA were computed from the linear fitting minimizing the chi-square function, $\chi^2(A,\alpha) = \sum_{i=0}^{N_i-1} \left(\frac{y_i - A - \alpha x_i}{\sigma_i} \right)^2$ where y_i, x_i, σ_i are $\ln D$, $\ln N$ and δD, respectively; and $\delta\alpha = \sqrt{S/\Delta_1}$, $\delta A = \sqrt{S_{xx}/\Delta_1}$ with $S = \sum_i \sigma_i^{-2}$, $S_{xx} = \sum_i x_i^2/\sigma_i^2$, $S_x = \sum_i x_i/\sigma_i^2$ and $\Delta_1 = SS_{xx} - S_x^2$ [41].

We can notice that (i) $\alpha \approx 1$ for $b \leq 20$, in agreement with linear chains with on-site disorder, as for instance the 1D Anderson model [16]; and (ii) $\alpha \approx 0.5$ for $b \gg 1$, corresponding to full random matrices [42]. Moreover we observe a transition region where $0.5 < \alpha < 1$ for intermediate values of b.

Thus, we will use Eq. (2.25) to set the onset of the superradiant transition in Eqs. (2.23) and (2.24)

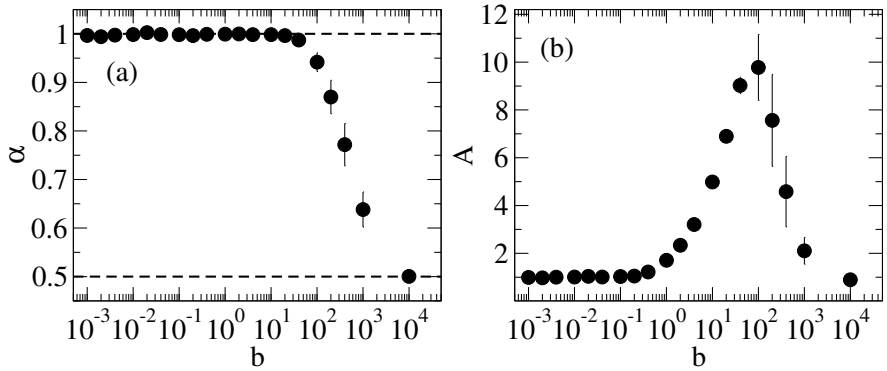

Figure 2.9: Fitting parameters (a) α and (b) A as function of bandwidth b, from the fittings of the data on Figs. 2.7 and 2.8 with Eq. (2.25).

for the scattering setups A and B, respectively.

2.4 Condition of the superradiant transition

Now, we can normalize the average decay widths $\langle\Gamma\rangle$ by the mean level spacing D, computed in the previous subsection, for the two scattering setups, to obtain the onset of the superradiant transition from Eqs. (2.23) and (2.24) for different chain sizes N and values of b.

Then, in Fig. 2.10 we show the normalized average decay width $\langle\Gamma\rangle/D$, both for superradiant and subradiant states, as a function of the coupling strength γ (normalized to D) for the scattering setup A. The averages were performed over 2^{k-3} eigenvectors with corresponding eigenvalues around the energy band center of 2^{15-k} disorder configurations.

We can notice that all the curves $\langle\Gamma\rangle_{\rm Sub}$ *vs.* γ fall on top of a single curve that below the ST behaves as $\langle\Gamma\rangle_{\rm Sub} \sim \gamma$, while above it follows $\langle\Gamma\rangle_{\rm Sub} \sim D^2/\gamma$; see black and red dashed lines in Fig. 2.10.

Meanwhile, in Fig. 2.11, we present the normalized average decay width $\langle\Gamma\rangle/D$, both for superradiant and subradiant states, as a function of the coupling strength γ (normalized by DN) for the scattering setup B, for the same parameters and statistics as in Fig. 2.10. Here, as well as for the scattering setup A, we observe that below the ST, $\langle\Gamma\rangle_{\rm Sub} \sim \gamma/N$, while above the ST, $\langle\Gamma\rangle_{\rm Sub} \sim D^2N/\gamma$.

From Figs. 2.10 and 2.11 we can observe that the behavior of the average decay width $\langle\Gamma\rangle_{\rm Sub}$ do not change for different chain sizes N if we properly normalize the coupling strengths for the scattering setup A as γ/D and for the scattering setup B as γ/DN. This is very important in order to be able to compute the multifractal dimensions D_q, since we need to scale the participation numbers of the eigenfunctions for the *open* PBRM model, for different chain sizes N and different values of b, always at the same coupling strength to the continuum.

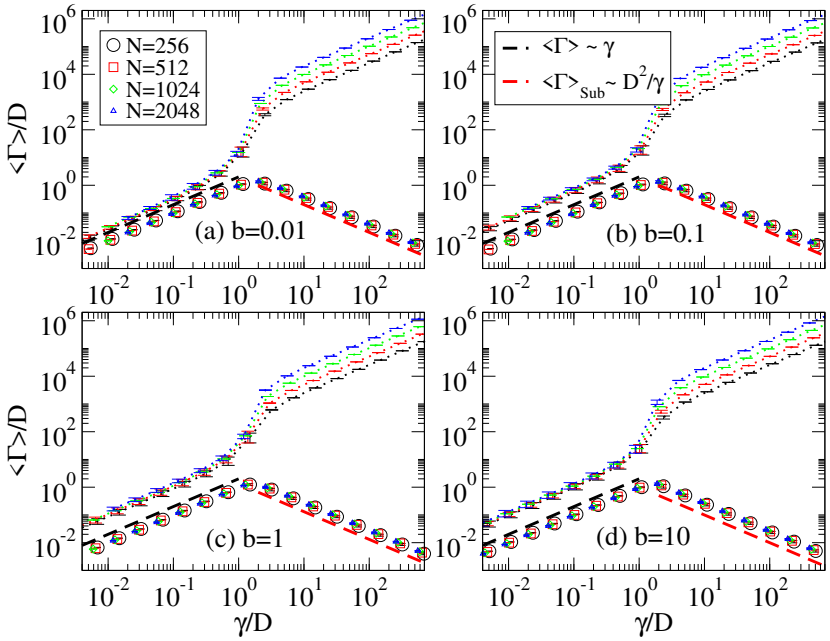

Figure 2.10: Average decay width $\langle\Gamma\rangle$ (normalized by D) *vs.* the coupling strength γ (normalized by D), for the scattering setup A. Here $b = \{0.01, 0.1, 1, 10\}$ and $N = \{256, 512, 1024, 2048\}$.

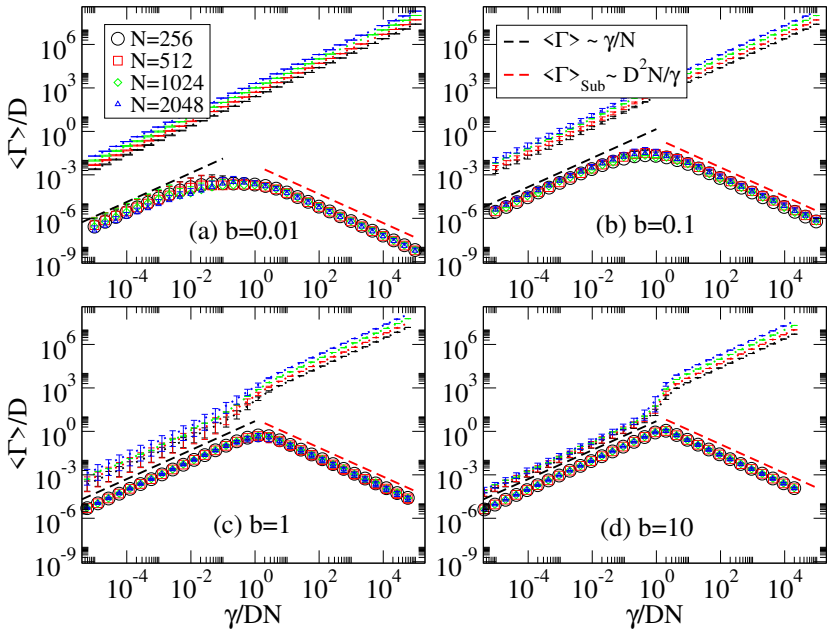

Figure 2.11: Same as in Fig. 2.10 for the scattering setup B with the coupling strength γ normalized by DN.

2.5 Multifractal dimensions D_q

As stated in the previous subsection, from Figs. 2.10 and 2.11 we can fix the coupling independently of the chain size N for fixed values of b and then compute the multifractal dimensions of the *open* PBRM model for both scattering setups.

So, we compute the multifractal dimensions D_q for subradiant and superradiant states, separately, for both scattering setups. The superradiant state corresponds to the eigenstate with largest decay width Γ and the remaining states $N-1$ are the subradiating states.

The multifractal dimensions D_q reported below were extracted from the linear fit of the logarithm of the inverse of the average participation numbers versus the logarithm of the system size N, see Eq. (2.18), while the information dimension D_1 was extracted from the linear fit of the average information entropy versus the logarithm of N, see Eq. (2.19). We used chain of sizes $N = 2^k$ with $6 \leq k \leq 11$. The averages were performed over 2^{k-3} eigenvectors with corresponding eigenvalues around the energy band center of 2^{15-k} disorder configurations.

For instance, in Fig. 2.12 we show the average participation number I_q, $q = \{1, 2\}$ and $b = 1$, with the coupling strength $\gamma/D = 1$ for the subradiant states in the scattering setup A. Here, the dashed lines are the linear fitting of D_q indicated in the legends.

The error bars of the average participation numbers δI_q were computed from the standard deviation of the mean, i.e. $\delta I_q = \sigma_I/\sqrt{N_E}$ where σ_I is the standard deviation of the distribution of the I_q and N_E is the size of the ensemble.

We show the error bars δD_q in all the simulations. The error bars δD_q were computed from the linear fitting of inverse of the $\ln I_q$ with $\ln N$ minimizing the chi-square function, $\chi^2(a, D_q) = \sum_{i=0}^{N_i-1} \left(\frac{y_i - a - D_q x_i}{\sigma_i} \right)^2$ where y_i, x_i, σ_i are the $\ln I_q$, $\ln N$ and δI_q, respectively; and $\delta D_q = \sqrt{S/\Delta_1}$ with $S = \sum_i \sigma_i^{-2}$, $S_{xx} = \sum_i x_i^2/\sigma_i^2$, $S_x = \sum_i x_i/\sigma_i^2$ and $\Delta_1 = SS_{xx} - S_x^2$ [41].

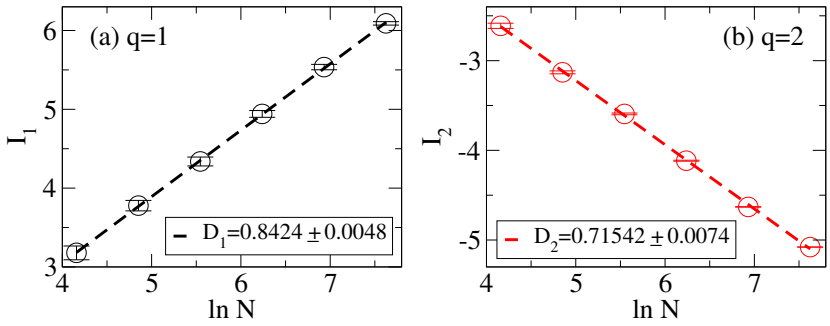

Figure 2.12: Average participation number I_q, $q = \{1, 2\}$, *vs.* the logarithm of the system size N with coupling strength $\gamma/D = 1$, $b = 1$, for the subradiant states in the scattering setup A. The dashed lines indicate the linear fitting where the slope is the corresponding D_q.

2.5.1 Scattering setup A

2.5.1.1 Subradiant states

In Fig. 2.13, we show some multifractal dimensions D_q for the subradiant states as a function of b for the coupling strengths $\gamma/D = \{10^{-3}, 1, 10^3\}$ for the scattering setup A. We are choosing $q = 0.6$, 1, 2, and 5 because (i) the corresponding D_q's have already been reported before for the closed PBRM model so we can compare with previous results, see the Ref. [28], and (ii) D_1 and D_2 are important

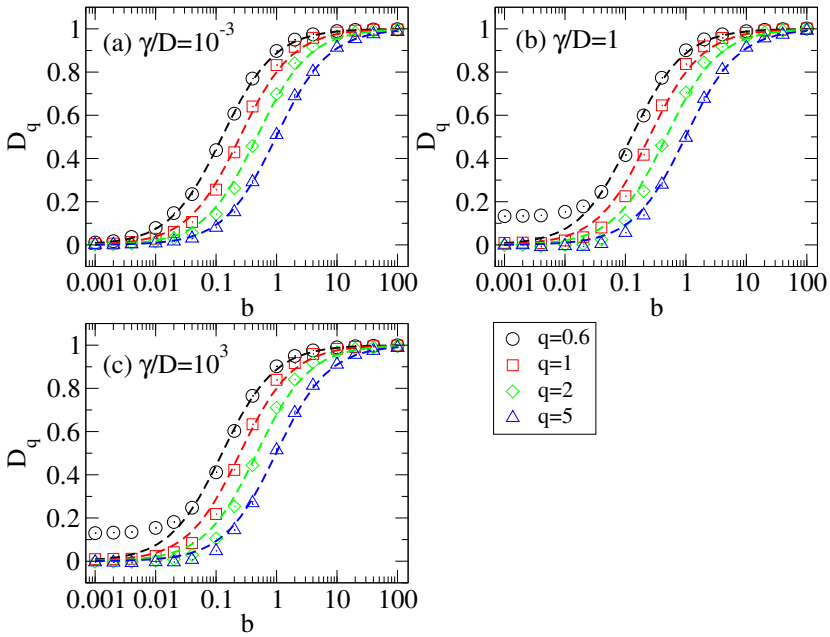

Figure 2.13: Multifractal dimensions D_q, $q = \{0.6, 1, 2, 5\}$, *vs.* the parameter b with coupling strengths $\gamma/D = \{10^{-3}, 1, 10^3\}$, for the subradiant states. The dashed curves indicate the D_q of the closed PBRM model.

fractal dimensions: the information dimension and the correlation dimension, respectively.

We can notice that the multifractal dimensions D_q do not change, in comparison with the D_q for the closed PBRM model, indicated by the dashed curves in Fig. 2.13; except for the multifractal dimension $D_{q=0.6}$ when $\gamma/D \geq 1$ and $b < 0.04$, see Figs. 2.13–(b) and 2.13–(c).

These results can be understood by recalling that subradiant states are mostly isolated regardless the coupling amplitude; i.e., they are almost not affected by the external environment. So that, the multifractal dimensions of the eigenstates of the complete effective Hamiltonian are similar to those of the isolated PBRM model.

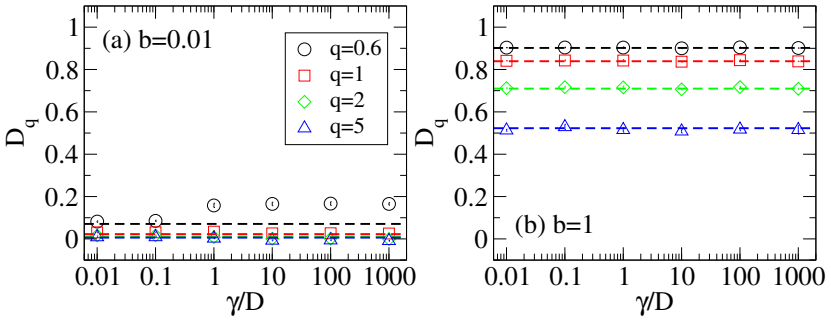

Figure 2.14: Multifractal dimensions D_q, $q = \{0.6, 1, 2, 5\}$, *vs.* the normalized coupling strength γ/D for $b = \{0.01, 1\}$ for the subradiant states. The dashed lines indicate the D_q of the closed PBRM model.

In order to complement the information of Fig. 2.13, in Fig. 2.14 we show the multifractal dimensions D_q as a function of the normalized coupling strength γ/D for $b = \{0.01, 1\}$. We can observe that the multifractal dimensions D_q for the subradiant states are independent of the coupling strength γ/D, except for $D_{q=0.6}$ for small values of b and $\gamma/D \geq 1$, as can be seen in Fig. 2.14–(a). The reason that the multifractal dimension of the subradiant states differs from the multifractal dimension of the closed system for small q can be explicated in the fact that these states have an hybrid nature. Indeed for small b where localization effect are more important, these states are constituted by an exponential localized peak with and extended tail, see chapter 4 for details. This implies a change on the multifractal dimension $D_{q=0.6}$ since the contribution of the extended tails are more important for small q than for large q.

2.5.1.2 Superradiant state

Now, in Fig. 2.15 we show the multifractal dimensions D_q of the superradiant state of the scattering setup A as a function of b for the coupling strengths $\gamma/D = \{1, 10^3\}$. Recall the superradiant state emerges at the superradiant transition (ST) for the coupling strength $\gamma/D = 1$. As can be clearly seen from this figure, the multifractal dimensions D_q of the superradiant state are strongly affected by the coupling to the continuum, as compared to the D_q's corresponding to the subradiant states; i.e. compare Figs. 2.13 and 2.15.

More specifically, at the superradiance transition, see Fig. 2.15–(a), and above it, see Fig. 2.15–(b), all the multifractal dimensions $D_q \to 1$ independently of the value of b. Since all the multifractal dimensions D_q are approximately equal to one at and above the ST, it means that the superradiant state becomes extended there.

Finally, in Fig. 2.16 we complete the information of Fig. 2.15 by plotting the multifractal dimensions D_q of the eigenstate with largest decay width Γ below the coupling strength $\gamma/D < 1$ and the superradiant state above the coupling strength $\gamma/D \geq 1$ of the scattering setup A now as a function of the normalized coupling strength. Thus, we verify the observations made above.

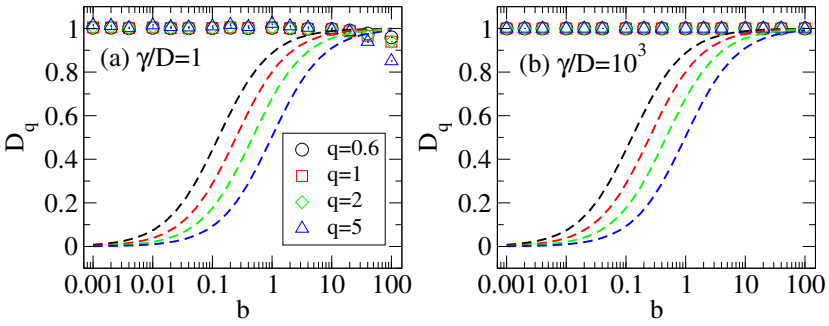

Figure 2.15: Same as in Fig. 2.13 for the superradiant state apart of the coupling strengths $\gamma/D = \{1, 10^3\}$.

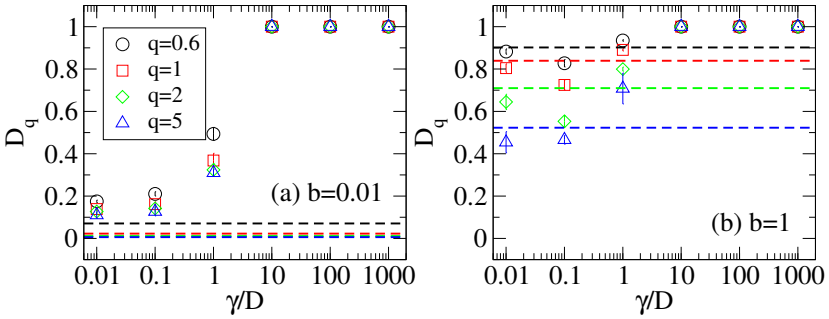

Figure 2.16: Same as in Fig. 2.14 for the superradiant state.

2.5.2 Scattering setup B

Now, as in the previous subsection, we perform an analysis of the multifractal dimensions D_q of the subradiant and superradiant states but for the scattering setup B.

2.5.2.1 Subradiant states

In Fig. 2.17, we show the multifractal dimensions D_q of the subradiant states of the scattering setup B as a function of b for the coupling strengths $\gamma/DN = \{10^{-3}, 1, 10^3\}$. Since coupling the PBRM model to the continuum through one site is less invasive than coupling it through all sites, the multifractal dimensions D_q of the subradiant states of the scattering setup B are practically the same as for the states of the closed PBRM model, whose D_q's are indicated by the dashed curves in Fig. 2.17.

Also, in Fig. 2.18 we plot the multifractal dimensions D_q of the subradiant states of the scattering setup B but as a function of the normalized coupling strength γ/DN for $b = \{0.01, 1\}$ and $q = \{0.6, 1, 2, 5\}$. We can see all the multifractal dimensions D_q are independent of the coupling strength γ/DN for all the values q studied. The horizontal dashed lines indicate the multifractal dimensions D_q of the states of the closed PBRM model.

2.5.2.2 Superradiant state

Now, in Fig. 2.19 we report some multifractal dimensions D_q of the superradiant state of the scattering setup B as a function of b, we use the coupling strengths $\gamma/DN = \{1, 10^3\}$. In the case of the superradiant state, the corresponding multifractal dimensions D_q are strongly affected by the coupling with the continuum, in contrast to the subradiant states.

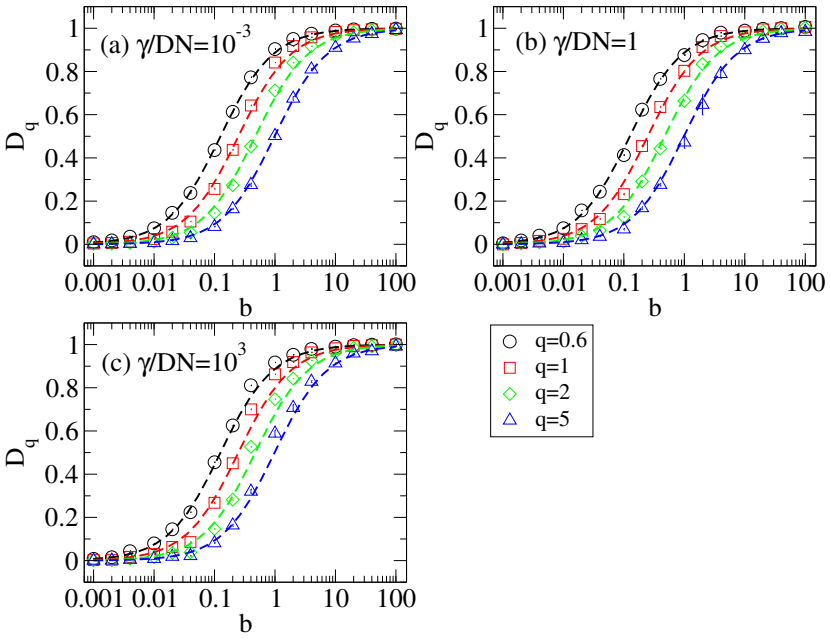

Figure 2.17: Multifractal dimensions D_q, $q = \{0.6, 1, 2, 5\}$, *vs.* the parameter b with coupling strengths $\gamma/DN = \{10^{-3}, 1, 10^3\}$, for the subradiant states. The dashed curves indicate the D_q of the closed PBRM model.

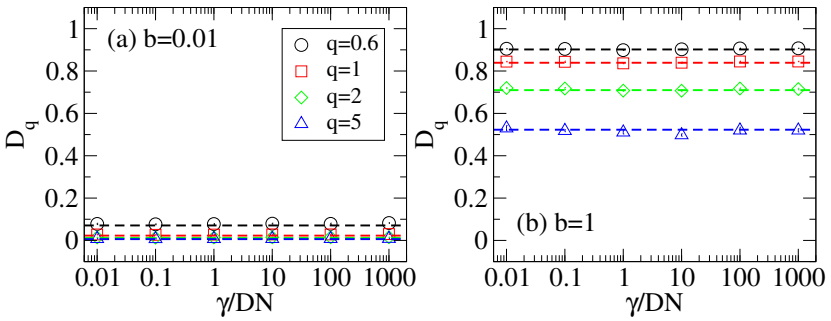

Figure 2.18: Multifractal dimensions D_q, $q = \{0.6, 1, 2, 5\}$, *vs.* the normalized coupling strength γ/DN for $b = \{0.01, 1\}$ for the subradiant states. The dashed lines indicate the D_q of the closed PBRM model.

Moreover, in Fig. 2.20 we present the multifractal dimensions D_q of the superradiant state of the scattering setup B but as a function of the normalized coupling strength γ/DN.

From both figures, Figs. 2.19 and 2.20, we can see that above the superradiant transition all the multifractal dimensions $D_q \to 0$ for the superradiant states of the scattering setup B, independently of the value of b. $D_q \approx 0$ means that the corresponding superradiant states are localized, in contrast to the superradiant states of the scattering setup A which are extended above the ST. Indeed, this situation was already expected since for the scattering setup B the one-mode channel is attached to a single site of the chain, thus above the ST transition the superradiant state is localized around that site.

From the results above we can conclude that the coupling of the PBRM model to the continuum

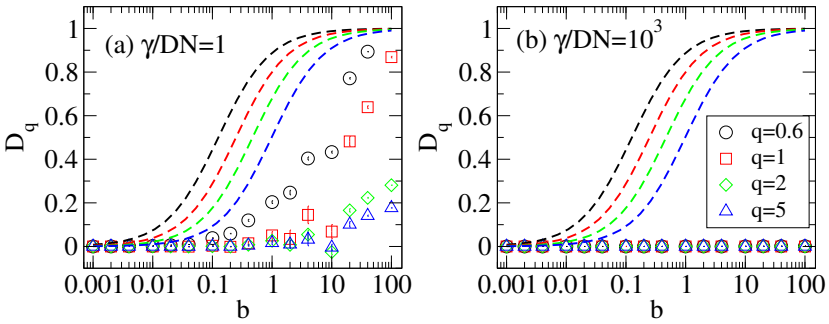

Figure 2.19: Same as in Fig. 2.17 for the superradiant state apart of the coupling strengths $\gamma/DN = \{1, 10^3\}$.

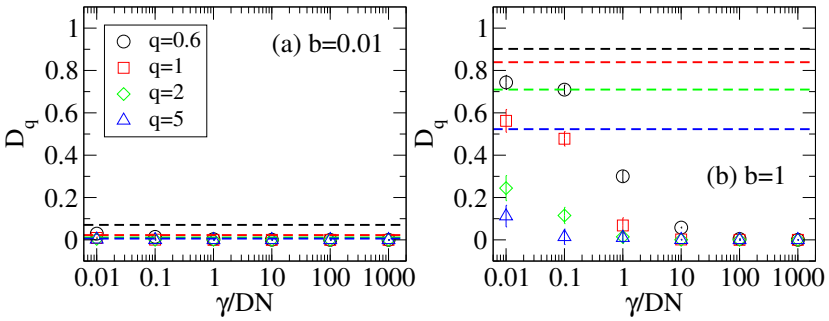

Figure 2.20: Same as in Fig. 2.18 for the superradiant state.

has a different effect on the properties of subradiant and superradiant states. While subradiant states are almost not affected by the coupling to the continuum, mainly in the scattering setup B where the multifractal dimensions D_q are practically the same as those of the states of the closed PBRM model, the superradiant states are strongly affected by the coupling; indeed, for the superradiant states $D_q \to 1$ for the scattering setup A and $D_q \to 0$ for the scattering setup B. One can say that while the multifractality of the subradiant states persists under the coupling to the continuum, the multifractality of the superradiant states is destroyed.

2.6 Probability $|\Psi|^2$ of the superradiant states

Since the multifractal dimensions D_q of the superradiant states Ψ are strongly affected by the coupling to the continuum, in this section we will have a closer look at their structure through their probability $|\Psi|^2$.

2.6.1 Scattering setup A

As shown in the previous subsection, in the scattering setup A, the superradiant state becomes extended (or delocalized) for any value of b, when the coupling strength is equal or larger than the onset of the superradiant transition, i.e. for $\gamma/D \geq 1$.

In Fig. 2.21 we verify the statement above by plotting the eigenfunction probability $|\Psi|^2$ for several superradiant states for a chain size $N = 1024$. In particular, see Fig. 2.21–(c) where we consider

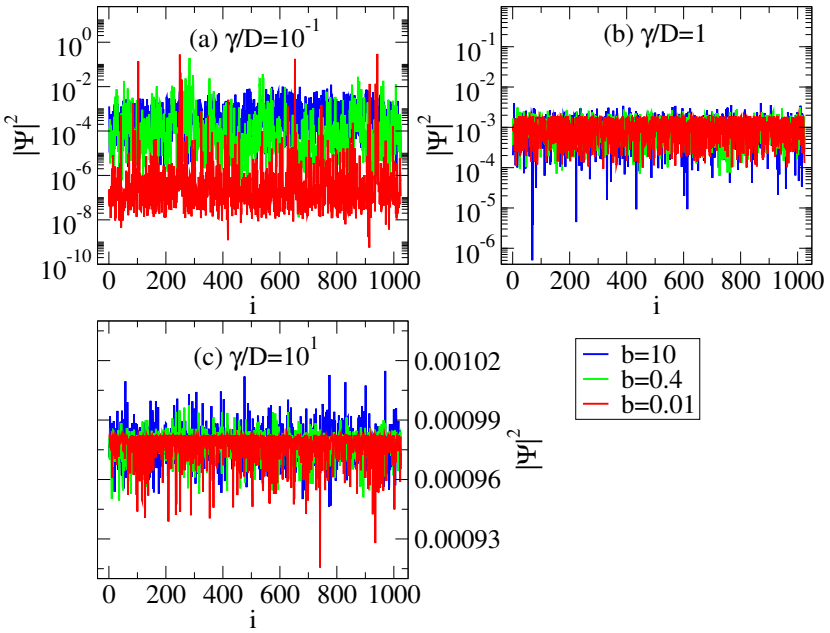

Figure 2.21: Eigenfunction probability $|\Psi|^2$ in the site basis i of typical superradiant states in the scattering setup A for the coupling strengths $\gamma/D = \{10^{-1}, 1, 10^1\}$ and $b = \{0.01, 0.4, 10\}$.

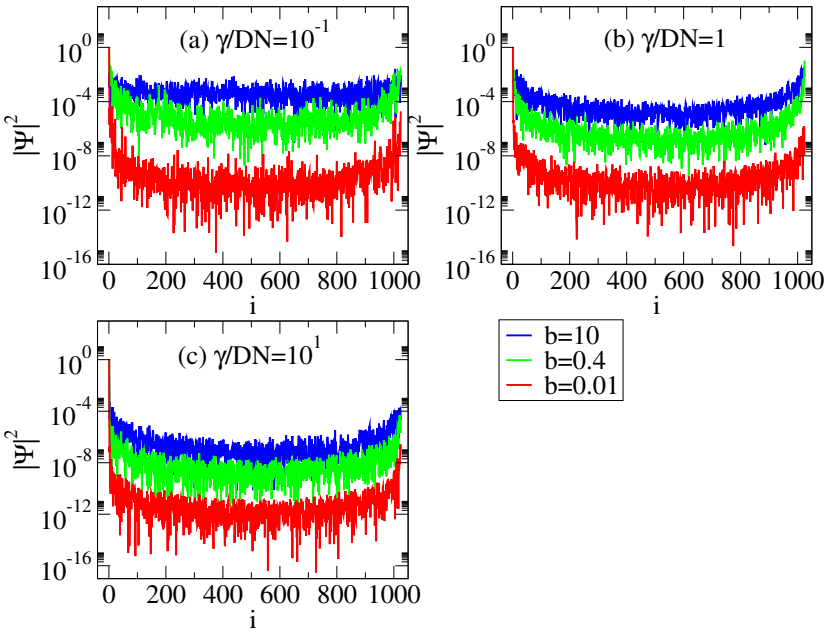

Figure 2.22: Same as in Fig. 2.21 for the scattering setup B apart of the coupling strengths $\gamma/DN = \{10^{-1}, 1, 10^1\}$.

$\gamma/D = 10 > 1$ and the states are clearly extended over the complete basis.

2.6.2 Scattering setup B

In contrast with the scattering setup A, in the scattering setup B, the superradiant state becomes localized for any value of b, when the coupling strength is equal or larger than the onset of the superradiant transition, i.e. for $\gamma/DN \geq 1$.

Then, in Fig. 2.22, we confirm the statement above by plotting the eigenfunction probability $|\Psi|^2$ for several superradiant states for a chain size $N = 1024$. In particular, see Fig. 2.22–(c) with the coupling strength $\gamma/DN = 10 > 1$, there states are clearly localized around the site $i = 1$, where the one-mode channel is attached.

2.7 Participation ratio PR

In order to study the interplay of the multifractal dimensions D_q and the coupling to one-mode channel we analyze the participation ratio of the superradiant and subradiant states of non-Hermitian effective Hamiltonian H_{eff} in Eq. (2.15), defined as,

$$\text{PR} = \left\langle \left| \sum_{i=1} |\langle i|\psi\rangle|^2 \right|^2 / \sum_{i=1} |\langle i|\psi\rangle|^4 \right\rangle \tag{2.26}$$

where the average is over disorder configurations. Note that for the case of non-Hermitian Hamiltonian, the PR indicates the number of sites over which the excitation is localized, provided it is in the system. For completely extended states, the $\text{PR} = N$ and for the completely localized states the $\text{PR} = 1$. Note that the participation ratio PR is related with the correlation dimension D_2 with the participation number I_2 with $q = 2$.

2.7.1 PR of the subradiant states

In Fig. 2.23, we show the PR as a function of the normalized coupling γ/D for the scattering setup A or γ/DN for the scattering setup B of the subradiant states for the system sizes $N = \{256, 512, 1024\}$ and $b = \{0.01, 0, 4, 10\}$.

From Figs. 2.13 and 2.17, we can see that D_2 has the same behavior as the closed PBRM model from localized to extended states as b increases. This behavior is confirmed with the PR in Fig. 2.23, for instance $b = 0.01$ in Figs. 2.23–(a) and 2.23–(b) the subradiant states are localized while for $b = 10$ in Figs. 2.23–(e) and 2.23–(f) the subradiant states become extended.

2.7.2 PR of the superradiant state

Now in Fig. 2.24, we show the PR of the superradiant state as a function of the normalized coupling γ/D for the scattering setup A or γ/DN for the scattering setup B. For comparison purposes, we use here the same parameters as in Fig. 2.23

From Figs. 2.15 and 2.19, we can see that the behavior of D_2 changes completely as the coupling increases and reaches the superradiant transition. We can see the superradiant state is extended for the scattering setup A and it is localized for the scattering setup B. This behavior in D_2 is confirmed in the Fig. 2.24, where the superradiant state becomes extended for any value of b when the normalized coupling strength $\gamma/D \geq 1$ in Figs. 2.24–(a), 2.24–(c) and 2.24–(e). While in Figs. 2.24–(b), 2.24–(d) and 2.24–(f) the superradiant state is localized for the normalized coupling strength $\gamma/DN \geq 1$.

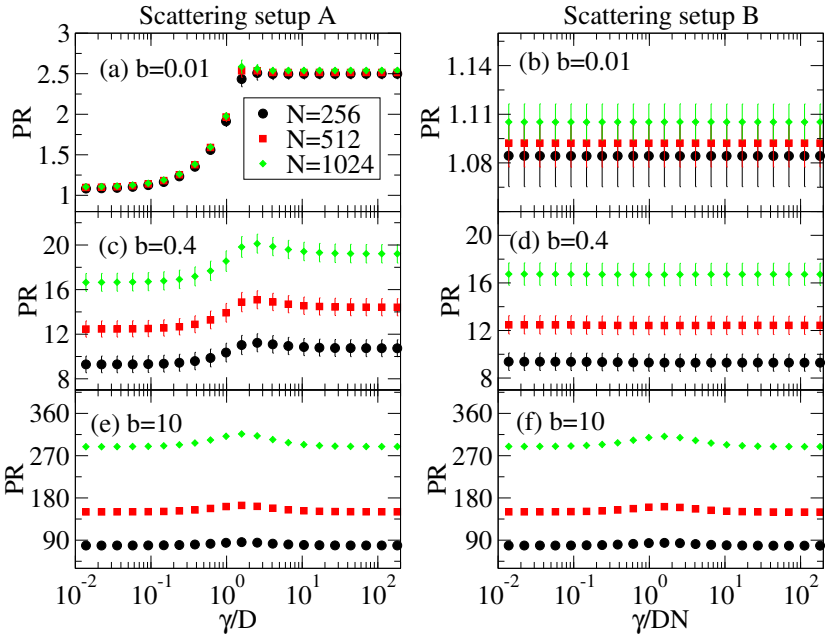

Figure 2.23: The participation ratio PR of the subradiant states *vs.* the normalized coupling strength γ/D for the scattering setup A or the normalized coupling strength γ/DN for the scattering setup B. Here, $N = \{256, 512, 1024\}$ and $b = \{0.01, 0.4, 10\}$.

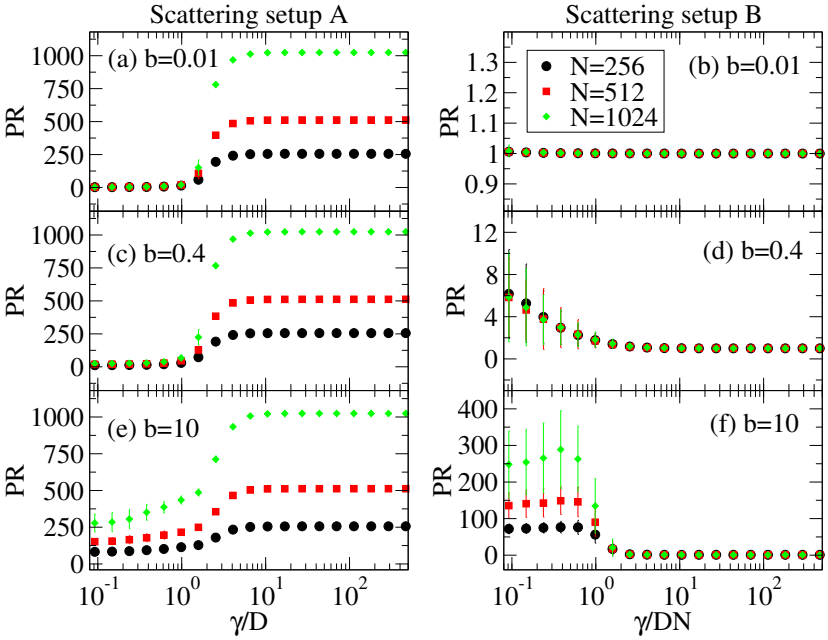

Figure 2.24: Same as in Fig. 2.23 for the superradiant state.

The participation ratio PR confirms the change in the nature of the multifractal dimension D_2 of

the superradiant state that becomes extended with the coupling $\gamma/D \geq 1$ for the scattering setup A or it becomes a localized state with the coupling $\gamma/DN \geq 1$ for the scattering setup B. It also confirms that the subradiant states are not affected by the coupling to one-mode channel and they behave like the closed PBRM model.

2.8 Multifractal dimensions D_q *vs.* the decay widths Γ

The set of multifractal dimensions D_q of a system is usually studied with the Eq. (2.18). When the system is coupled to a one-mode channel, the states of the system acquire decay widths Γ. Thus, it is possible to analyze the multifractal dimensions D_q as a function of these decay widths Γ. Summarizing the previous results, for the scattering setup A the subradiant states have the same multifractal dimensions D_q of the closed PBRM model apart of small q and small b, see Figs. 2.13–(c) and 2.14–(a), where the hybrid nature of the eigenstates arise. While for the superradiant state, its multifractal dimensions D_q are totally different, actually it becomes an extended state, see Fig. 2.15. On the other hand, for the scattering setup B the subradiant states have the same multifractal dimensions D_q of the closed PBRM model for all the values q and b, see Fig. 2.17. While the superradiant state becomes a localized state, see Fig. 2.19.

In this section, we study the multifractal dimensions D_q as a function of the decay widths Γ only for the scattering set up A. Let us stress that it is the first time that an analysis of D_q as a function of the decay widths of the eigenstates is performed. Indeed, we can ask the following question: Do we have a smooth dependence of the multifractal dimensions D_q of the system on the decay widths Γ, mainly at criticality?

In order to answer this question, we will consider values of b for which the subradiant states behave exactly like the closed system while the superradiant states are extended. We will focus on three different coupling regimes: below, above and at criticality.

For a fixed decay width Γ, the multifractal dimensions D_q reported below were extracted from the linear fit of the logarithm of the inverse of the average I_q versus the logarithm of the system size N while D_1 was extracted from the linear fit of the average information entropy versus the logarithm of the system size N, see Eq. (2.19). We used chains of sizes $N = 2^k$ with $6 \leq k \leq 11$. The averages were performed over 2^{k-2} eigenvectors (corresponding to the $1/4$ of states in the band center) and we used 2^{20-k} disorder configurations for each system size.

In Fig. 2.25 we show the multifractal dimensions D_q, $q = \{0.6, 1, 2, 5\}$ and $b = 0.1$, as a function of the decay widths Γ and fixed coupling strengths $\gamma/D = \{10^{-2}, 1, 10^2\}$.

We can observe that the D_q of the eigenstates with the smallest decay widths Γ are not influenced by the coupling with the external environment and they resemble the multifractal dimensions of the closed PBRM model, indicated with horizontal dashed lines in Fig. 2.25. The eigenstates with the largest widths Γ are more affected by the coupling to the external environment and their multifractal dimensions $D_q \to 1$ for $\gamma/D \geq 1$, see Fig. 2.25–(b) and 2.25–(c).

One can also observe that an important dependence on the decay widths Γ arises at criticality and above the ST. As the decay widths Γ grows, the multifractal dimensions D_q smoothly change until they approach one, i.e. the states become fully extended so they do not show a multifractal structure, for most superradiant states.

Note that in order to obtain these results, we increased the system size by keeping the coupling to the continuum γ/D fixed. For instance, the maximum decay width is constant in this case for different system sizes N.

Note that one may wonder whether this is the proper way to analyze the system. In order to answer this question, we also analyze the dependence of the multifractal dimensions, always keeping

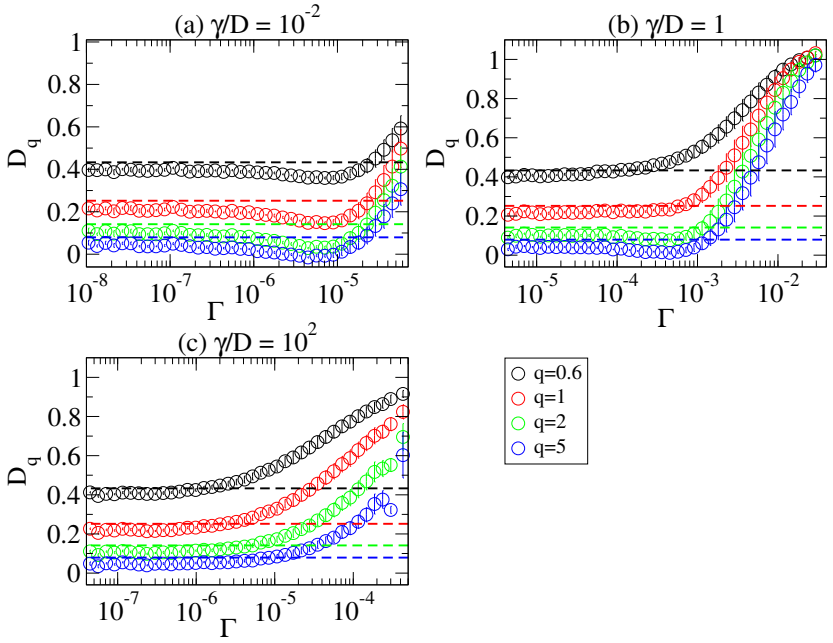

Figure 2.25: Multifractal dimensions D_q, $q = \{0.6, 1, 2, 5\}$, *vs.* the decay widths Γ for $b = 0.1$ and $\gamma/D = \{10^{-2}, 1, 10^{2}\}$ for the scattering setup A. The horizontal dashed lines indicate the D_q for the closed PBRM model.

γ/D fixed, as a function of Γ/D, where D is the mean level spacing computed for the closed system.

For simplicity, we focused on the case $q = 2$. We considered the average participation numbers I_2 and we computed $-\ln I_2/\ln N$, which in the limit of infinite system size, corresponds to the multifractal dimensions D_2. The arrows in Fig. 2.26 show in which direction this ratio increases with the system size N.

In Fig. 2.26, $-\ln I_2/\ln N$ is shown as a function of the normalized decay widths Γ/D (upper panels) and Γ (lower panels) for $b = 0.1$ and the couplings strength $\gamma/D = \{10^{-2}, 1, 10^{2}\}$. Here, the black dashed horizontal lines indicate the value of D_2 of the isolated PBRM model.

We observe that there is no universal scaling both for Γ nor Γ/D. For instance if we consider Γ/D, the subradiant states scale very well but the superradiant states do not, see Fig. 2.26–(c) where one can observe that the segregated superradiant states have different values of Γ/D. On the other side, if we consider the dependence on Γ alone, the subradiant states do not scale well with the system size, while the superradiant states scale perfectly well. Indeed their decay widths are totally independent of Γ above the ST transition, see Fig. 2.26–(f), which is exactly what one would expect if the coupling strength to the continuum is fixed as we change the system size.

This shows that neither of the two choices provide a good scaling for both the subradiant and superradiant states. For instance, in Fig. 2.26–(b), at criticality we observe that the subradiant states have a good scaling but the superradiant states do not. For this reason, in the future we intend to find the best way to analyze the multifractal dimensions D_q for this open system where the scaling with the system size N strongly depends on the decay widths Γ of the eigenstates and it is different for subradiant and superradiant states.

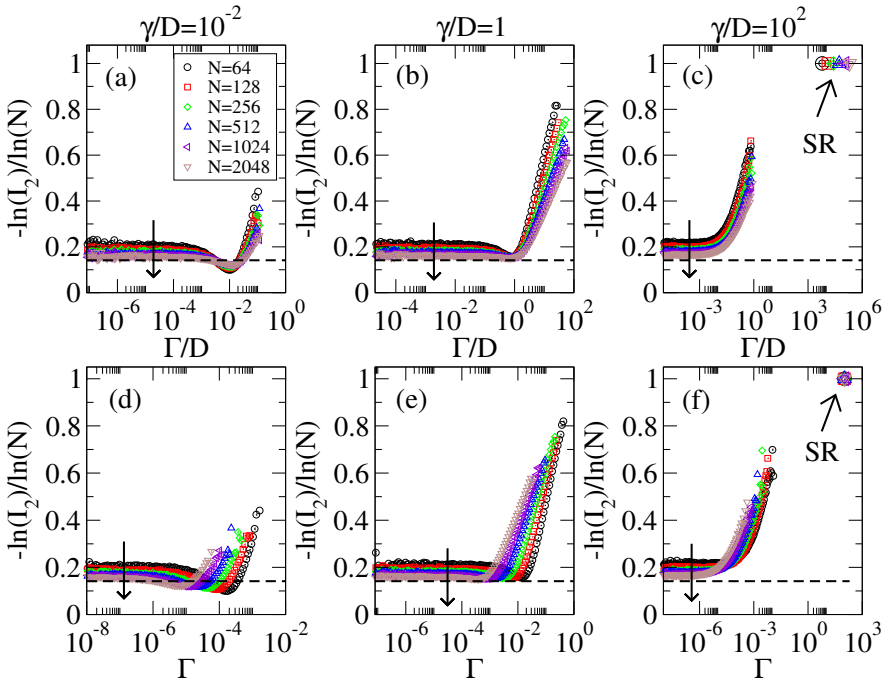

Figure 2.26: The ratio $-\ln I_2/\ln N$ *vs.* the normalized decay widths Γ/D (upper panels) and the ratio $-\ln I_2/\ln N$ *vs.* the decay widths Γ (lower panels) for $b = 0.1$, $N = \{2^6, 2^7, 2^8, 2^9, 2^{10}, 2^{11}\}$ and $\gamma/D = \{10^{-2}, 1, 10^2\}$ Here, the black dashed lines indicate D_2 for the isolated PBRM model.

2.9 Distribution of the decay widths

In this section, we will study the scattering properties of the PBRM model in the two scattering setups by analyzing the distribution of decay widths Γ. For the statistics of the decay widths Γ we use the eigenvalues around $E \approx 0$ corresponding to the 25% of the total spectra, the number of the data is 262144. Instead of using the decay widths Γ we decided to study the typical value of Γ: $\Gamma^{\rm typ} \equiv \exp\langle \ln \Gamma \rangle$ and the logarithm of the decay widths $\ln \Gamma$.

2.9.1 Scattering setup A

In Fig. 2.27 we show the distribution of the logarithm of the normalized decay widths $P(\ln \Gamma/\Gamma^{\rm typ})$ as a function of $\ln \Gamma/\Gamma^{\rm typ}$ when all the sites in the system are coupled to an one-mode channel for the chain sizes $N = \{64, 128, 256, 512, 1024\}$ and $b = \{0.1, 1, 10\}$. We observe a good scaling of $\ln P(\ln \Gamma/\Gamma^{\rm typ})$ with the chain size N and we found an universal distribution for each set of parameters $(b, \gamma/D)$ as $L \to \infty$.

2.9.2 Scattering setup B

Now, in Fig. 2.28 we show the distribution of the logarithm of the normalized decay widths $P(\ln \Gamma/\Gamma^{\rm typ})$ as a function of $\ln \Gamma/\Gamma^{\rm typ}$ when one site in the system is coupled to an one-mode channel with the

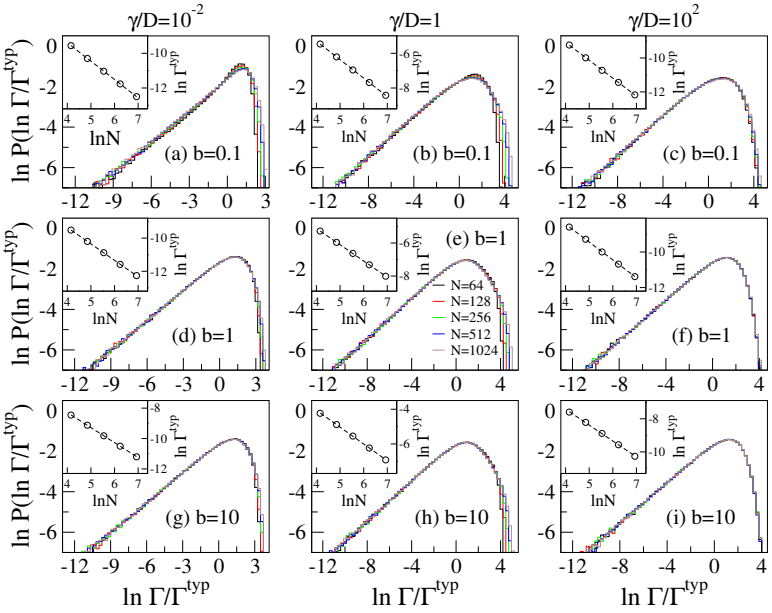

Figure 2.27: Distribution $\ln P(\ln \Gamma/\Gamma^{\mathrm{typ}})$ *vs.* $\ln \Gamma/\Gamma^{\mathrm{typ}}$ for $\gamma/D = \{10^{-2}, 1, 10^{2}\}$ and $b = \{0.1, 1, 10\}$ for the scattering setup A. In the insets the scaling $\Gamma^{\mathrm{typ}} \propto N^{-\nu}$ is shown together with a linear fitting. Here, $\Gamma^{\mathrm{typ}} \equiv \exp\langle \ln \Gamma \rangle$.

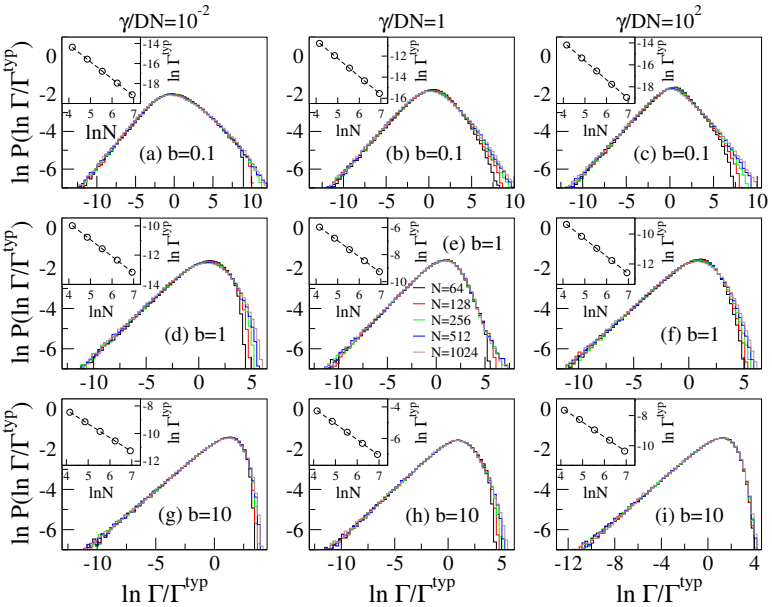

Figure 2.28: Same as in Fig. 2.27 for the scattering setup B.

same parameters as Fig. 2.27. Here, we also found a good scaling of $\ln P(\ln \Gamma/\Gamma^{\mathrm{typ}})$ and an universal distribution for the set of parameters $(b, \gamma/DN)$. The distributions for the case of the coupling strength $\gamma/DN = 1$ are in agreement with the results reported in Ref. [32].

From Figs. 2.27 and 2.28, in Fig. 2.29 we plot the exponent ν as a function of b where ν is extracted from the scaling $\Gamma^{\rm typ} \propto N^{-\nu}$ (see the insets in Figs. 2.27 and 2.28) for the coupling strengths $\gamma/D = \{10^{-2}, 1, 10^2\}$ in the scattering setup A and for the coupling strengths $\gamma/DN = \{10^{-2}, 1, 10^2\}$ in the scattering setup B. We found that the exponent ν is well approximated by $2 - D_2$ when only one site is coupled to an one-mode channel independently of the coupling strengths and follow the relation [32]

$$\Gamma^{\rm typ} \propto N^{-(2-D_2)} \tag{2.27}$$

and the exponent $\nu \approx 1$ when all the sites are coupled to an one-mode channel independently of the magnitude of the normalized coupling strength γ/D and we obtain the relation

$$\Gamma^{\rm typ} \propto N^{-1} \tag{2.28}$$

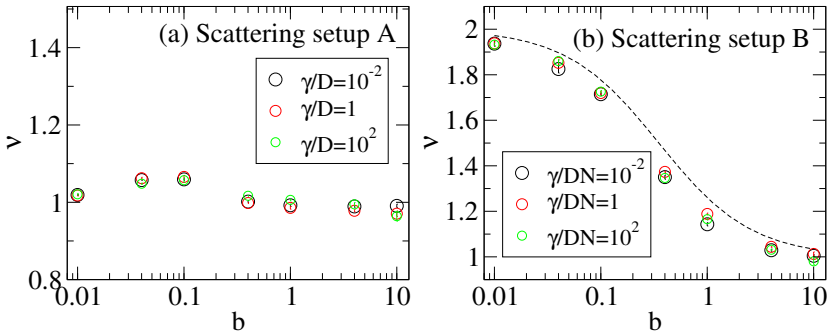

Figure 2.29: The exponent ν as a function of b extracted from the scaling $\Gamma^{\rm typ} \propto N^{-\nu}$ in Figs. 2.27 and 2.28. In panel (b) the dashed curve is $2 - D_2$ where D_2 was obtained from Eq. $D_2 \approx [1 + (\alpha_2 b)^{-1}]^{-1}$ with $\alpha_2 = 2.12146$.

In this section, we found a good scaling of $\ln P(\ln \Gamma/\Gamma^{\rm typ})$ and an universal distribution for the set of parameters $(b, \gamma/D)$ or $(b, \gamma/DN)$ for both scattering setups. For the scattering setup B, we are able to establish the relation $\Gamma^{\rm typ} \propto N^{-(2-D_2)}$ where $D_2 \approx [1 + (\alpha_2 b)^{-1}]^{-1}$ with $\alpha_2 = 2.12146$

2.10 Conclusions of Chapter 2

The PBRM model is a very rich model since for $\mu = 1$, which corresponds to a metal-insulator transition point, the multifractal dimensions D_q of the corresponding eigenfunctions can be continuously tuned by moving the parameter b. In this Chapter we have studied a 1D tight-binding chain (of length N with long-range random hoppings), represented by the PBRM model, when it is coupled to an unbounded external system characterized by a continuum of states. We have used two scattering setups: One where all sites of the chain are coupled to a common one-mode channel (scattering setup A); another where only one site of the chain is coupled to a one-mode channel (scattering setup B). In particular we have characterized the states of the open system by means of a set of multifractal dimensions D_q since it is well known that the eigenstates of the closed PBRM model are multifractal objects characterized by non-trivial sets of multifractal dimensions.

As an effect of the coupling to an external continuum of states, we have the emergence of subradiant and superradiant states. Since both types of states are expected to have different statistical properties, we analyzed them separately.

We have found that the multifractal dimensions D_q of the subradiant states of the open PBRM model are quite similar to those of the isolated model, apart for small q and small b in the scattering setup A. This explained this difference as due to the hybrid nature of the subradiant states and we plan to deepen the understanding of this effect in the future. However, the multifractal dimensions D_q of superradiant states undergo major changes above the superradiant transition: for the scattering setup A the superradiant state becomes extended for all values of the bandwidth b, that is $D_q \to 1$; while for the scattering setup B the superradiant state becomes localized, i.e. $D_q \to 0$. This is confirmed by the analysis that we have performed of the eigenfunction probability distribution of the superradiant states and their participation ratios PR.

We also studied the multifractal dimensions D_q as a function of the decay width Γ. We found that D_q for the subradiant states with the smallest decay widths Γ do not feel the influence of the coupling to the continuum and they resemble the states of the closed PBRM model. On the other hand, the states with largest decay widths Γ are drastically affected by the coupling. Indeed, for these states, $D_q \to 1$ for $\gamma/D \geq 1$.

The main result of this Chapter is that by opening the PBRM model we add a new degree of freedom to the multifractal dimensions D_q of the system. Indeed, D_q strongly depends on the decay widths Γ of the eigenstates. This effect is mainly visible at the ST transition where the D_q are not uniform for all states but strongly depend on Γ. Nevertheless more work in needed in the future to fully characterize the dependence of the multifractal dimensions D_q on the decay widths Γ.

Chapter 3

Real and imaginary energy gaps: a comparison between single excitation Superradiance and Superconductivity and robustness to disorder

Cooperative effects, which are at the basis of emergent properties [43], are at the center of research investigations in a vast variety of fields: emergent properties in highly correlated materials [44], cooperative emission in superconducting qubits [6], Superradiance in cold atomic clouds [3], cooperative shielding in long range interacting systems [17], collective excitations in semiconductors [45], plasmonic Dicke effect [46], biophysical systems [47, 48] and proposal of quantum devices which exploits cooperative effects [49]. Despite the great importance of emergent properties, a general unifying framework and a full understanding of cooperative effects has not been found yet. One of the most interesting properties of cooperative effects is their robustness to the noise induced by external environments. A well known example is Superconductivity, but other quantum emergent effects, such as Single Excitation Superradiance (SES), have also been shown to be robust to noise [16, 50]. This suggests that emergent properties could play an essential role in the successful development of scalable quantum devices able to operate at room temperature. Since cooperative effects represent a common mechanism to all these emergent phenomena, we believe that finding links between different cooperative effects will be fundamental to progress our understanding of emergence. As was suggested by U. Fano [51] a common mechanism underlies several collective phenomena, such as Superconductivity, plasmon excitation and giant resonances in nuclei. In particular a possible connection between Superradiance and Superconductivity has been discussed by M. Scully in Ref. [52].

In this Chapter, we perform a comparison between Superconductivity, i.e. the discrete Bardeen-Cooper-Schrieffer (BCS) model, and Single Excitation Superradiance (SES model). Superradiance is usually referred to the case of many excitations in an ensemble of N two level systems and to the existence of states which emit energy with an intensity proportional to N^2. On the other hand, SES refers to the possibility that a single excitation coherently shared by N two level systems can decay with a rate proportional to N, an effect defined as the Super of Superradiance in Ref. [53] due to the fact

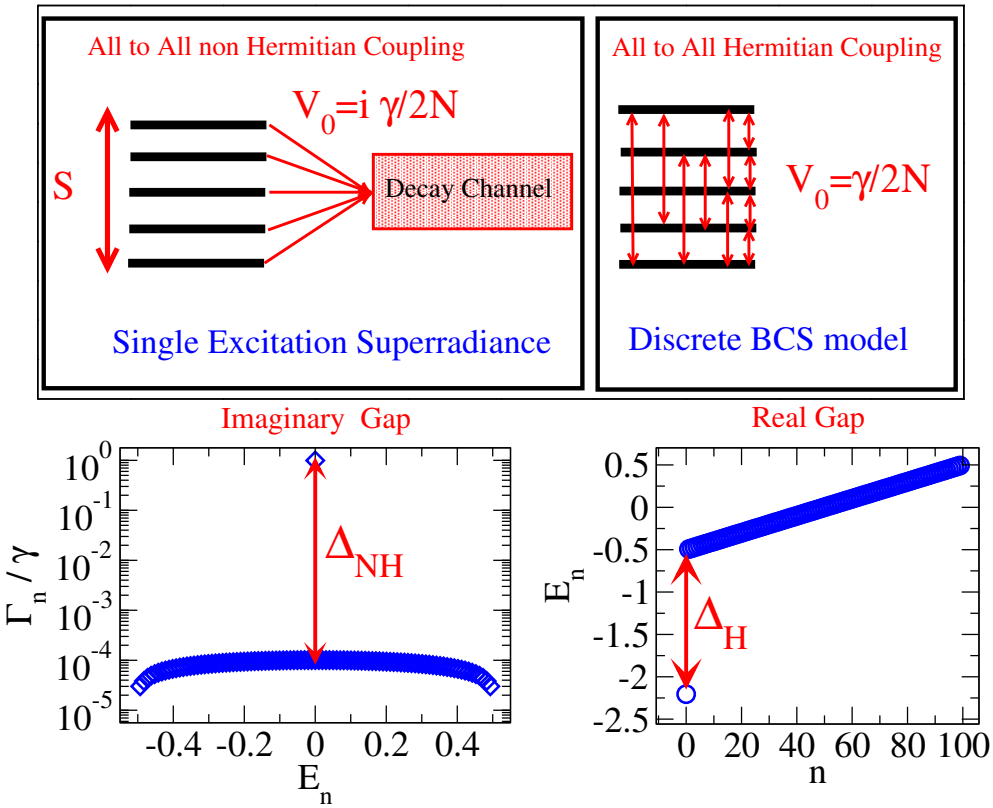

Figure 3.1: (Left upper panel) Paradigmatic model of SES: the coupling of equally spaced single particle energy levels to a common channel in the continuum induces a non-Hermitian all to all interaction between the energy levels described by the Hamiltonian in Eq. (3.1) with $V_0 = i\gamma/(2N)$. (Right upper panel) The discrete BCS model of Superconductivity where Cooper pair states are coupled by a Hermitian all to all interaction, see arrows between levels, described by the Hamiltonian in Eq. (3.1) with $V_0 = \gamma/(2N)$. (Lower left panel) Complex eigenvalues $E_n - i\Gamma_n/2$ for the SES model and the imaginary energy gap are shown. (Lower right panel) The eigenvalues E_n and the real energy gap are shown for the BCS model. Parameters are: $N = 100$, $S = 1$, $\gamma = 10\gamma_{\rm cr}^{\rm H,NH}$, where $\gamma_{\rm cr}^{\rm H,NH}$ is the critical coupling for the BCS/SES transition.

that SES involves a fully entangled state. Note that SES has been found experimentally in interacting two level system, such as cold atomic clouds [7] or in molecular aggregates [54].

Specifically, we analyze a paradigmatic model of SES, which has been studied in [13], see Fig. 3.1. In such model, the single excitation energy levels are assumed equally spaced and connected to a single decay channel in the continuum. Due to the fact that the system is open and the excitation can be lost in the common decay channel, the eigenvalues of the system are complex. When the resonances overlap, a Superradiance transition occurs: a Superradiant state acquires most of the decay width of the system, while the other $N - 1$ subradiant states decrease their own decay widths on increasing the coupling strength with the common decay channel. In the limit of large coupling to the continuum only the Superradiant state can decay. Here we will show that the Superradiance transition is connected with the emergence of an imaginary energy gap between the complex eigenvalues of the

system. Our aim is to investigate and compare the energy gaps arising in such paradigmatic model of Superradiance [13, 55] with the well-known energy gap present in a model of Superconductivity (the discrete BCS model [56, 57]), paying main attention to the robustness to disorder induced by the presence of a gap and to the kind of interaction which originates the gap.

The discrete BCS model is widely used to analyze Superconductivity in small metallic grains [56]. Moreover, the single particle (single Cooper pair) sector of the discrete BCS model had been studied in several papers [57]. In this case, the model is very similar to the model proposed by L. Cooper in his seminal paper [14] and its Hamiltonian reads:

$$H = H_0 + V = \sum_k E_k^0 \left|k\right\rangle \left\langle k\right| - V_0 \sum_{k,k'} \left|k\right\rangle \left\langle k'\right| \,, \tag{3.1}$$

where $|k\rangle$ is the Cooper pair state, E_k^0 is the unperturbed energy, usually taken as equally spaced (picket fence (PF) spectrum), and V_0 is the coupling between the Cooper pair states. The coupling is the same for all the states, similarly to what happens in models with an infinite range coupling in space, with the difference that here the coupling is in momentum space. The same model, see Fig. 3.1, is used to describe the Superradiance transition in a system where many levels are coupled to the same channel in the external environment [13]. The only but important difference is that for the case of Superradiance V_0 is a pure imaginary number. In this case $|k\rangle$ represents a single energy level or an atomic or molecular excitonic state in a specific point of the real space. For the case of Superradiance, the non-Hermitian Hamiltonian, originating from the imaginary coupling, takes into account the fact that the system can decay into the continuum but it also represents the coupling between the energy levels which modifies the spectral features of the system [58]. The limit of validity and the effectiveness of the effective non-Hermitian Hamiltonian description of the system has been investigated in Ref. [36]. In such systems a transition to Superradiance occurs above a critical coupling strength. In the Superradiant regime, when one superradiant state acquire most of the decay width of the system, a gap opens in the complex energy plane of the non-Hermitian Hamiltonian, see Fig. 3.1 lower left panel.

Note that the model presented in Eq. (3.1), apart from being relevant in studying cooperative effects, it is also relevant in describing realistic systems. For instance, for the hermitian case, this model can be reproduced in ion trap experiments with a tunable interaction range, including all-to-all coupling [5, 17]. On the other side, for the non-Hermitian case, this model is relevant in nuclear physics [58] and it could be also deviced in molecular systems [48].

3.1 Analytical results for N levels

Let us consider N equally spaced levels in an energy range S, coupled between each other with a constant coupling V_0, which can be real or imaginary. The Hamiltonian can thus be written as in Eq. (3.1), where for the energy we assume a PF distribution, namely

$$E_k^0 = k\delta = k\frac{S}{N} \,, \qquad k = -\frac{N}{2}, \ldots, \frac{N}{2} \,, \tag{3.2}$$

where $\delta = S/N$ is the level spacing. First, for the sake of clarity, we present the derivation of the Gap Equation [13, 14, 59], both for the Hermitian and non-Hermitian cases, which is equivalent to the Schrödinger Equation and it makes the computation of some eigenvalues much easier. For the derivation of the Gap Equation we follow [59], which presents a simplified version of the famous derivation by L. Cooper in his seminal paper [14].

We want to solve the Schrödinger Equation

$$H\left|\Psi\right\rangle = E\left|\Psi\right\rangle, \tag{3.3}$$

where $|\Psi\rangle$ is an eigenstate of the total Hamiltonian H and it can be expanded as

$$\left|\Psi\right\rangle = \sum_k a_k \left|k\right\rangle, \tag{3.4}$$

where $|k\rangle$ are eigenstates of H_0, satisfying

$$H_0\left|k\right\rangle = E_k^0\left|k\right\rangle . \tag{3.5}$$

Eq. (3.3) can be rewritten as

$$(H - H_0)\left|\Psi\right\rangle = V\left|\Psi\right\rangle . \tag{3.6}$$

Then, using the expansion (3.4), we get

$$(H - H_0)\sum_{k'} a_{k'}\left|k'\right\rangle = V\sum_{k'} a_{k'}\left|k'\right\rangle = \sum_{k'} a_{k'}V\left|k'\right\rangle . \tag{3.7}$$

Now let us project Eq. (3.7) on the state $\langle k|$. Defining $V_{kk'} = \langle k|V|k'\rangle$ we have

$$\langle k|\sum_{k'}(E - E_{k'}^0)a_{k'}\left|k'\right\rangle = \sum_{k'} a_{k'}V_{kk'} . \tag{3.8}$$

Now, since $\langle k|k'\rangle = \delta_{k,k'}$ and $V_{kk'} = -V_0\ \forall k, k'$ we get

$$\sum_{k'}(E - E_{k'}^0)a_{k'}\left\langle k|k'\right\rangle = (E - E_k^0)a_k = -V_0\sum_k a_k . \tag{3.9}$$

Defining $C \equiv \sum_k a_k$ we have

$$a_k = -\frac{V_0 C}{E - E_k^0} \tag{3.10}$$

so that

$$C = \sum_k a_k = -V_0\sum_k \frac{C}{E - E_k^0} . \tag{3.11}$$

Dividing by C we finally obtain the Gap Equation

$$1 = -V_0\sum_k \frac{1}{E - E_k^0} . \tag{3.12}$$

Eq. (3.12) has been obtained by simple linear manipulations of the Schrödinger equation, and so they are equivalent. Given the unperturbed eigenvalues E_k^0, there are N possible values of E which satisfy Eq. (3.12), which are the eigenvalues of H.

The term Gap Equation comes from the fact that it is commonly used to compute the gap between the ground state and the excited states. In the next sections we will compute the gap for the case $V_0 = \gamma/(2N)$ real (for Superconductivity) and for $V_0 = i\gamma/(2N)$ complex (for Superradiance). Note that in both cases we rescale the coupling by N as it is found in the discrete BCS model [56, 57]). The non rescaled case can be easily deduced by substituting γ with $N\gamma$ in the following results.

3.1.1 Hermitian case

Following Refs. [14, 57, 59], let us review the main results about the Gap Equation for the Hermitian case. Note that with respect to the BCS model, $1/\delta$ is the Density of States at the Fermi level, S in the Debye energy and V_0 the effective phonon mediated interaction. Let us now consider the Hermitian case, with $V_0 = \gamma/(2N)$. Recalling that the unperturbed spectrum is given by (3.2), we multiply both sides of (3.12) by $2S/\gamma$ to have

$$\frac{2S}{\gamma} = \sum_{k=-N/2}^{N/2} \frac{1}{k - E/\delta} \,. \tag{3.13}$$

A graphical solution of Eq. (3.13) is shown in Fig. 3.2 for $N = 5$. The r.h.s. of Eq. (3.13), shown as a continuous black line, is an unbounded function of E/δ having N asymptotes, corresponding to $E/\delta = -N/2, \ldots, N/2$ and shown as vertical black lines. The l.h.s., shown as dashed lines, is independent of E/δ. The solutions are given by the values of E where the r.h.s. intersects the l.h.s. and they are shown by full circles in Fig. 3.2.

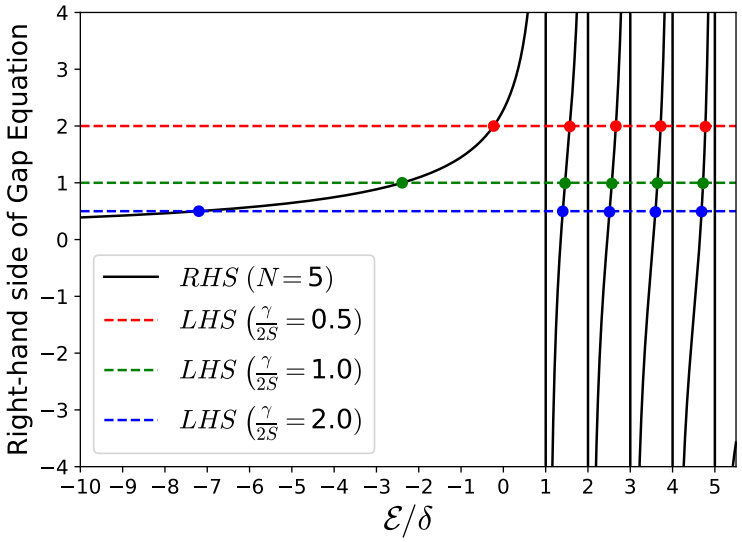

Figure 3.2: Graphical solution of Gap Equation (3.13) in the Hermitian case. The all-to-all coupling here is $V_0 = \gamma/(2N)$. We set $N = 5$.

From Fig. 3.2 one can see that there are $N = 5$ solutions to Eq. (3.13). Those solutions represent the eigenvalues E of the total Hamiltonian (3.1), divided by the level spacing $\delta = S/N$ of the unperturbed levels. Moreover, one can observe that, by increasing the ratio $\gamma/(2S)$ (so to increase the all-to-all coupling), the energy gap between the ground state and the first excited state increases, too. We are here interested in computing that gap in the limit $N \to \infty$ and keeping $S = $ const., so that the spacing δ of the unperturbed levels tends to 0. First of all, from Fig. 3.2 we can see that the energy of the excited states are all in the range $[-S/2, S/2]$ and, in particular, the first excited state lies in the interval $-S/2 + \delta < E_2 < -S/2 + 2\delta$. This implies that only the ground state E_1 can be less than $-S/2$ and that the energy of the first excited state E_2 tends to $-S/2$ when $\delta \to 0$. Now, let us focus on the energy of the ground state.

If $N \gg 1$, we can take the continuum limit for the Gap Equation (3.12)

$$1 = -\frac{\gamma}{2N}\int_{-S/2}^{S/2}\frac{N(x)dx}{E-x}, \tag{3.14}$$

where $N(x) = N/S$ is the density of states and it is constant for a PF level distribution. Then we can analytically solve the integral

$$1 = -\frac{\gamma}{2S}\int_{-S/2}^{S/2}\frac{dx}{E-x} = \frac{\gamma}{2S}\ln\frac{2E-S}{2E+S}, \tag{3.15}$$

noting that the above solution is valid only for $E < -S/2$. For what we stated before, the only state which satisfies this requirement is the ground state E_1. Then we have

$$E_1 = \frac{S}{2}\frac{1+e^{2S/\gamma}}{1-e^{2S/\gamma}}. \tag{3.16}$$

Now, let us recall that $E_2 \to -S/2$ when $N \to \infty$ and S does not depend on N (see [59] and the previous considerations on Fig. 3.2). We can then define the Hermitian Gap between the ground state and the first excited state as

$$\Delta_{\mathrm{H}} = E_2 - E_1 = -\frac{S}{2} - E_1 = \frac{S}{e^{2S/\gamma}-1}. \tag{3.17}$$

Note that the expression of the energy gap obtained is the same as the one obtained by L. Cooper [14], but it is slightly different from the BCS gap[1] [56, 57]. In the limit $S \ll \gamma/2$ Eq. (3.17) is approximated as

$$\Delta_{\mathrm{H}} \approx \frac{\gamma}{2}. \tag{3.18}$$

On the other hand, when $S \gg \gamma/2$, Eq. (3.17) becomes

$$\Delta_{\mathrm{H}} \approx S\, e^{-2S/\gamma} \tag{3.19}$$

On increasing γ, the energy gap Δ_{H} increases as well and, for some $\gamma = \gamma_{\mathrm{cr}}^{\mathrm{H}}$ it becomes equal to the unperturbed level spacing $\delta = S/N$. By setting $\Delta_{\mathrm{H}} = \delta$, it is easy to find that for $N \gg 1$,

$$\gamma_{\mathrm{cr}}^{\mathrm{H}} = \frac{2S}{\ln(N+1)} \approx \frac{2S}{\ln N}, \tag{3.20}$$

which defines the critical coupling at which a gap opens in the BCS model.

3.1.2 Non-Hermitian case

Superradiant state (Gap Equation) Now, let us consider the non-Hermitian case $V_0 = i\gamma/(2N)$. Starting from Eq. (3.12) we obtain a Gap Equation

$$1 = -\frac{i\gamma}{2N}\sum_k \frac{1}{\mathcal{E}-E_k^0}, \tag{3.21}$$

[1] In the BCS theory [59] and in Refs. [17, 56] the following expression for the gap is reported: $\Delta_{\mathrm{BCS}} = S/\sinh(2S/\gamma)$, which gives different results from Eq. (3.17) in some parameter range. In particular, when $S \gg \gamma/2$, Eq. (3.17) and Δ_{BCS} differ by a factor of 2, namely $\Delta_{\mathrm{H}} \approx S\, e^{-2S/\gamma}$ and $\Delta_{\mathrm{BCS}} \approx 2S\, e^{-2S/\gamma}$. On the other hand, in the opposite limit $S \ll \gamma/2$, both (3.17) and Δ_{BCS} have the same approximated expression $\Delta_{\mathrm{H}} \approx \Delta_{\mathrm{BCS}} \approx \gamma/2$. Nevertheless, both expressions predict that the gap closes in the limit $\gamma/S \to 0$.

where the eigenvalues are now complex,

$$\mathcal{E} = E - i\frac{\Gamma}{2}\,. \tag{3.22}$$

This complex equation splits into two real equations

$$\begin{cases} \displaystyle\sum_k \frac{E - E_k^0}{(E - E_k^0)^2 + \Gamma^2/4} = 0 \\ \displaystyle\sum_k \frac{\Gamma/2}{(E - E_k^0)^2 + \Gamma^2/4} = \frac{2N}{\gamma} \end{cases} \tag{3.23}$$

which have N solutions that depend on N and γ. In Fig. 3.3 we plot the complex eigenvalues in the plane $(E/\delta, \Gamma/\gamma)$ for $N = 6$ (upper panel) and $N = 7$ (lower panel), as a function of γ. In particular, we plot the trajectories of the eigenvalues starting from $\gamma = (2S/\pi)/10$ (open circles) up to $\gamma = 10(2S/\pi)$ (full circles). The value $\gamma = 2S/\pi$ marks the Superradiance transition, as we will show here below. When γ is small, see open circles in Fig. 3.3, the real parts of the eigenvalues are given by (3.2), while the imaginary part is $\Gamma_n \approx \gamma/N$ for all eigenvalues. On increasing γ, the spacing between the real parts of the eigenvalues decreases (a phenomenon called "pole attraction") up to a critical point $\gamma_{\rm SR}$, where we see a different behavior between $N = 6$ and $N = 7$.

For $N = 6$, in Fig. 3.3 upper panel, the two eigenvalues whose real part is closer to 0 collapse to the imaginary energy axis (so that $E_n = 0$ for both of them) when $\gamma > \gamma_{\rm SR}$. The widths of those two eigenvalues, however, have a different behavior because one increases with γ (and we call the respective state *Superradiant*) while the other one decreases with γ. For $\gamma \gg \gamma_{\rm SR}$ the total decay width of the system is concentrated in the superradiant state, while the other $N - 1$ states have a negligible decay width, and thus they are called *subradiant*.

For $N = 7$, in Fig. 3.3 lower panel, the behavior is similar to that of $N = 6$. For $\gamma \gg \gamma_{\rm SR}$ the total decay width of the system is concentrated into one superradiant state. The difference, with respect to $N = 6$, is that for $\gamma > \gamma_{\rm SR}$ only the Superradiant state has $E_{\rm SR} = 0$, while $E_n \neq 0$ for the subradiant states.

The same behavior seen for $N = 6$ has been observed for all even values of N, while the behavior observed for $N = 7$ has been seen for all odd values of N. In the following calculations we look for an analytical expression for the width $\Gamma_{\rm SR}$ of the superradiant state and for the critical coupling strength $\gamma_{\rm SR}$ and, based on the above discussion, we can set $E = 0$ in Eq. (3.23).

Moreover, in the limit $N \gg 1$ we approximate the PF spectrum (3.2) with a continuous energy distribution constant in the interval $[-S/2, S/2]$, so that we can solve the second equation in (3.23)

$$\frac{2N}{\gamma} = \frac{N}{S}\int_{-S/2}^{S/2} dx \frac{\Gamma/2}{x^2 + \Gamma^2/4} = \frac{2N}{S}\arctan\frac{S}{\Gamma}\,, \tag{3.24}$$

from which we get the width of the superradiant state

$$\Gamma_{\rm SR} = \frac{S}{\tan\frac{S}{\gamma}}\,. \tag{3.25}$$

This term is crucial to determine the energy gap in the complex plane between the superradiant and the closest subradiant state. Note that $\Gamma_{\rm SR}$ has to be positive, and this gives the condition of validity of Eq. (3.24), which is $\gamma \geq \frac{2S}{\pi}$.

Therefore the superradiant state exists only above a critical coupling strength which coincides with the so-called Superradiance transition (at $\gamma = \gamma_{\rm SR}$), as we will show below.

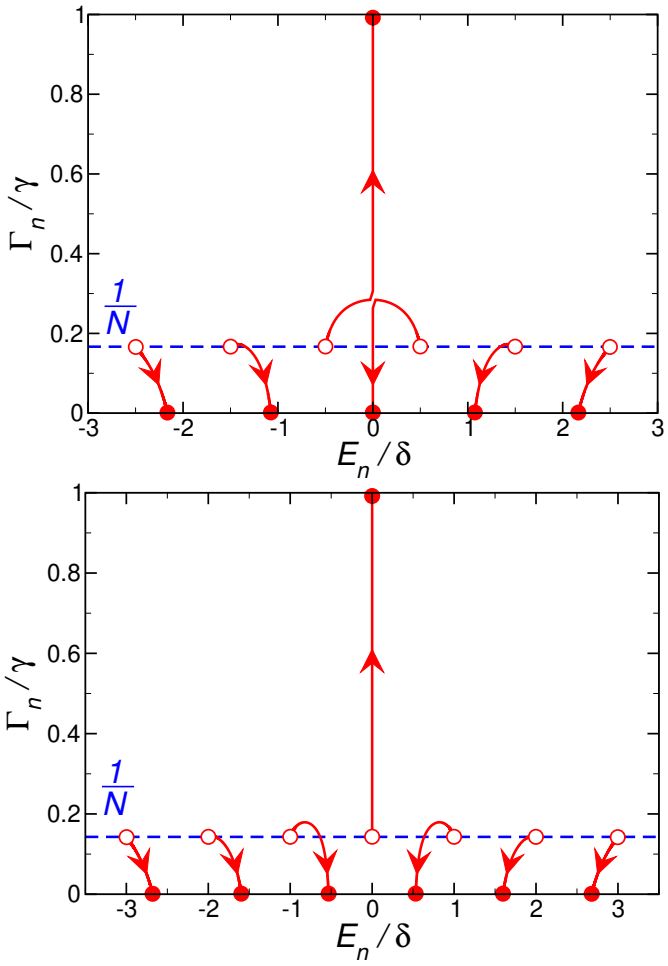

Figure 3.3: Complex eigenvalues (3.22) varying γ from $\gamma = (2S/\pi)/10$ (open circles) to $\gamma = 10(2S/\pi)$ (full circles). γ increases following the arrows. The dashed line marks the value $\Gamma_n = \gamma/N$. Parameters: $N = 6$ (upper panel) and $N = 7$ (lower panel).

Superradiant transition. In Ref. [13] the critical coupling at which a Superradiance transition occurs has been computed analytically by studying the dependence of the widths of the subradiant states on γ. Indeed below the Superradiance transition the widths of the subradiant states increase with γ, while above it, they decrease with γ. From Ref. [13] we have:

$$\gamma_{\rm SR} = \frac{2S}{\pi}\,. \tag{3.26}$$

Which is the same critical value of γ computed in the previous section.

Adapting the analytical results of Ref. [13] to our case (see Appendix A for details) the decay widths of all the eigenstates below the Superradiance transition are

$$\Gamma = \frac{S}{N\pi}\ln\left(\frac{1+\gamma/\gamma_{\rm SR}}{1-\gamma/\gamma_{\rm SR}}\right) \qquad \text{for } \gamma < \gamma_{\rm SR}\,, \tag{3.27}$$

while all the widths of the subradiant states above the Superradiance transition are

$$\Gamma_{\rm sub} = \frac{S}{N\pi} \ln\left(\frac{\gamma/\gamma_{\rm SR}+1}{\gamma/\gamma_{\rm SR}-1}\right) \qquad \text{for } \gamma > \gamma_{\rm SR}\,. \tag{3.28}$$

Note that the critical coupling parameter $\gamma_{\rm SR}$ is the point where the widths (3.27)-(3.28) are non-analytical.

Imaginary energy gap. The gap in the complex energy plane can be defined as

$$\Delta_{\rm NH} = \max_i \left\{ \min_{j\neq i} \left[\text{dist}\left(\mathcal{E}_i, \mathcal{E}_j\right)\right]\right\}, \tag{3.29}$$

where the distance in the complex plane between two eigenvalues is

$$\text{dist}\left(\mathcal{E}_i, \mathcal{E}_j\right) = \sqrt{\left(E_i - E_j\right)^2 + \frac{1}{4}\left(\Gamma_i - \Gamma_j\right)^2}\,. \tag{3.30}$$

We can use the previous analytical results given in Eqs. (3.27,3.28) to estimate such complex gap. For $\gamma < \gamma_{\rm SR}$, the widths of all the states are the same and the distance in real energy is constant and equal to δ, where δ is the level spacing in the PF model, see Eq. (3.2), so that we have $\Delta_{\rm NH} = \delta$ and no gap is present. On the other side in the superradiant regime $\gamma > \gamma_{\rm SR}$, we can estimate $\Delta_{\rm NH}$ as the distance in the complex plane between the superradiant eigenstate $\mathcal{E}_{\rm SR}$ and the closest subradiant state $\mathcal{E}_{\rm sub}$, see Appendix A for details, namely

$$\Delta_{\rm NH} = \sqrt{\left(E_{\rm SR} - E_{\rm sub}\right)^2 + \frac{1}{4}\left(\Gamma_{\rm SR} - \Gamma_{\rm sub}\right)^2}\,. \tag{3.31}$$

When $N \to \infty$ we have $\left(E_{\rm SR} - E_{\rm sub}\right) \approx \delta \to 0$ and $\Gamma_{\rm sub} \to 0$ (see (3.28)), so that the gap $\Delta_{\rm NH}$ is determined only by the decay width of the superradiant state (3.25),

$$\lim_{N\to\infty} \Delta_{\rm NH} = \frac{\Gamma_{\rm SR}}{2} = \frac{S}{2\tan\frac{S}{\gamma}}\,. \tag{3.32}$$

Now, we can define the critical value $\gamma_{\rm cr}^{\rm NH}$ as the value of γ at which the gap opens, i.e. by imposing $\Delta_{\rm NH} = \delta$. From Eq. (3.32), we then have

$$\gamma_{\rm cr}^{\rm NH} = \frac{S}{\arctan\frac{N}{2}}\,. \tag{3.33}$$

Note that this value is finite in the $N \to \infty$ limit,

$$\lim_{N\to\infty} \gamma_{\rm cr}^{\rm NH} = \frac{2S}{\pi}\,, \tag{3.34}$$

and it has the same value as $\gamma_{\rm SR}$ (see Eq. (3.26)). Our results demonstrate that the Superradiant transition, previously analyzed in Ref. [13], is equivalent to the emergence of a gap in the imaginary energy axis.

Moreover, we can approximate the gap for large γ, close to the transition and below the critical point, respectively, as

$$\Delta_{\rm NH} \approx \frac{\gamma}{2} \qquad \text{for } \gamma \gg \gamma_{\rm SR} \tag{3.35a}$$

$$\Delta_{\rm NH} \approx \frac{\pi S}{4}\left(\frac{\gamma}{\gamma_{\rm cr}^{\rm NH}} - 1\right) \qquad \text{for } \gamma \gtrsim \gamma_{\rm SR} \tag{3.35b}$$

$$\Delta_{\rm NH} = 0 \qquad \text{for } \gamma \leq \gamma_{\rm SR}\,. \tag{3.35c}$$

Note that for $\gamma \gg \gamma_{\rm SR}$ the complex energy gap of the superradiant model is identical to the real energy gap of the superconductivity model, see Eq. (3.18). On the other side, in the limit of large system sizes, the critical coupling for the emergence of a gapped state goes to zero for the BCS model, while for the SES model it remains finite.

3.2 Numerical results

Here we validate our previous analytical predictions with few numerical results.

In Fig. 3.4 the energy gap $\Delta_{\rm H,NH}$ is shown, both for the Hermitian and non-Hermitian cases, as a function of γ for different system sizes N. For the non-Hermitian case we define the energy gap using the distance in the complex plane, see Eqs. (3.29,3.30). Similarly, for the Hermitian case we define the gap as

$$\Delta_{\rm H} = \max_i \left\{ \min_{j\neq i} \left[{\rm dist}\left(E_i, E_j\right) \right] \right\} , \tag{3.36}$$

where ${\rm dist}\left(E_i, E_j\right) = |E_i - E_j|$ is the distance in the real axis (consistently with the non-Hermitian definition (3.30)).

With this definition, the presence of a finite and N independent $\Delta_{\rm H,NH}$ in some region of γ signals the existence of an energy gap in the spectrum. In contrast, we have no gap in the spectrum in the region of parameters where $\Delta_{\rm H,NH}$ goes to zero as N increases.

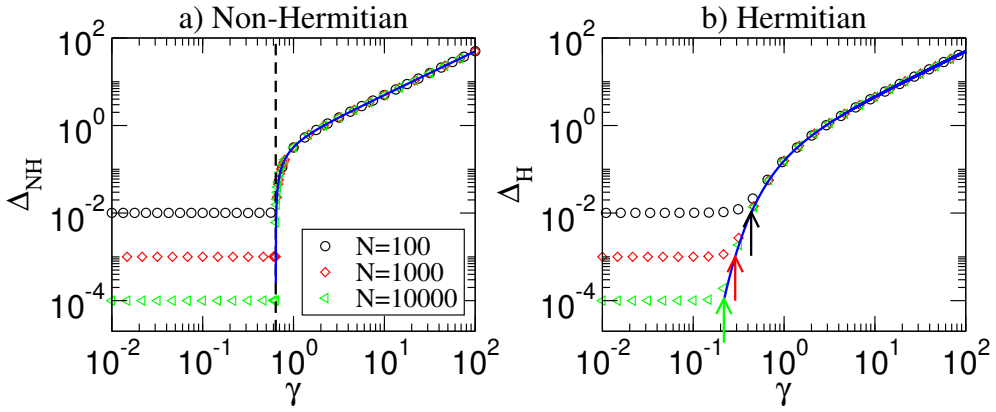

Figure 3.4: a) Gap $\Delta_{\rm NH}$ *vs.* the coupling parameter γ. Symbols are given by (3.29)-(3.30), while the continuous blue curve shows the analytical estimate (3.32). The dashed vertical line marks the critical coupling strength $\gamma_{\rm cr}^{\rm NH}$ from Eq. (3.34). b) Gap $\Delta_{\rm H}$ *vs.* the coupling parameter γ. Symbols are given by (3.36) while the continuous blue curve shows the analytical estimate (3.17). The arrows indicate the critical coupling strength $\gamma_{\rm cr}^{\rm H}$ from Eq. (3.20). Here, $S = 1$ and $N = \{100, 1000, 10000\}$.

The continuous blue curve in Fig. 3.4 indicates the analytical estimate of the energy gap $\Delta_{\rm H,NH}$ for both cases: Eq. (3.17) for the Hermitian case and Eq. (3.32) for the non-Hermitian one. The critical couplings strength $\gamma_{\rm cr}^{\rm H,NH}$ can be identified graphically as the values of γ above which the numerical data for $\Delta_{\rm H,NH}$ (symbols) coincide with the analytical estimates (continuous blue curves). In the figure our predictions of the critical couplings given in Eq. (3.34) (vertical dashed line in panel (a)) and Eq. (3.20) (arrows in panel (b)) are also shown.

Our analytical estimate for the energy gap works well above the critical γ for both Hermitian and non-Hermitian coupling, for all the values of N shown.

Interestingly we find that the critical γ is independent of N for large N in the non-Hermitian case, as we predicted in Eq. (3.34), while it decreases with N in the Hermitian case, according to our prediction (3.20). Moreover from Fig. 3.4 one can see that the transition to a gapped phase in the non-Hermitian case is much sharper than the transition in the Hermitian case. Note that for $\gamma < \gamma_{\rm cr}^{\rm H,NH}$ our estimate predicts that $\Delta_{\rm H,NH} \to 0$ for $\gamma \to 0$, while the numerical simulations show that $\Delta_{\rm H,NH} \to \delta = S/N$. This is clearly a finite size effect and it is not relevant since δ goes to zero when $N \to \infty$.

3.3 Imaginary energy gap and robustness to perturbations

We have shown the emergence of both Hermitian and non-Hermitian energy gaps in the spectrum of a Picket-Fence model. While, in the Hermitian case, it is well known that a energy gap between the ground state and the excited states makes the first more robust to perturbations, it is not trivial that an imaginary energy gap has the same effect on the gapped state. Thus, here we will apply perturbation theory to non-Hermitian systems and we will show how the distance in the complex plane is related to the robustness to perturbations. Then we will show numerically how the non-Hermitian energy gap makes the system robust to static disorder.

3.3.1 Non-Hermitian perturbative approach

Let us consider a perturbation D to the non-Hermitian Hamiltonian H, so that the total Hamiltonian of the system can be written as:

$$H_D = H + D\,, \tag{3.37}$$

where H is a generic non-Hermitian symmetric Hamiltonian.

Since H is non-Hermitian, its eigenfunctions are not orthogonal. First of all, let us define a "non-Hermitian bra", being the transpose of a ket

$$\langle\langle\psi| := (|\psi\rangle)^t\,. \tag{3.38}$$

Since the Hamiltonian is symmetric, the left eigenfunctions $\langle\langle\psi_i|$ are the "bra" of the right eigenfunctions $|\psi_i\rangle$, that is

$$H\,|\psi_i\rangle = \mathcal{E}_i\,|\psi_i\rangle \quad \text{and} \quad \langle\langle\psi_i|\,H = \mathcal{E}_i\langle\langle\psi_i|\,. \tag{3.39}$$

From here, the biorthogonality condition arises as

$$\langle\langle\psi_i|\psi_j\rangle = \delta_{ij}\,. \tag{3.40}$$

When the perturbation D is sufficiently small, a perturbative correction of the complex eigenvalues up to second order can be derived [50], and it has the expression

$$\overline{\mathcal{E}}_n \approx \mathcal{E}_n + \langle\langle\psi_n|D|\psi_n\rangle + \sum_{m\neq n} \frac{\langle\langle\psi_n|D|\psi_m\rangle^2}{\mathcal{E}_n - \mathcal{E}_m}\,. \tag{3.41}$$

From Eq. (3.41) it is clear that the strength of the perturbation is determined by the ratio of two complex numbers $z_1 = \langle\langle\psi_n|D|\psi_m\rangle^2$, $z_2 = \mathcal{E}_n - \mathcal{E}_m$.

This proves that a state separated by an energy gap in the complex plane from the rest of the spectrum is robust to perturbations as long as the gap is large compared to the modulus of the perturbations.

As a simple example of the above general calculations, let us consider a system made of two resonant sites, separated by a pure imaginary gap $i\gamma$, and perturbed with a coupling D. Note that this simple model has been used to describe experimental evidence of Dynamical "Quantum Phase Transition" in spin systems [60].

The corresponding non-Hermitian Hamiltonian is

$$H + D = \begin{pmatrix} E_0 & 0 \\ 0 & E_0 - i\gamma \end{pmatrix} + \begin{pmatrix} 0 & d \\ d & 0 \end{pmatrix}$$

and the eigenenergies $\overline{\mathcal{E}}_\pm$ of $H + D$ can be analytically obtained as

$$\overline{\mathcal{E}}_\pm = E_0 - \frac{i\gamma}{2} \pm \frac{i\gamma}{2}\sqrt{1 - \frac{4d^2}{\gamma^2}}\,. \tag{3.42}$$

Now, let us consider the case when $2d \ll \gamma$, i.e. the complex gap γ is much larger than the coupling d between the sites. Under this assumption we can expand the eigenenergies (3.42) to obtain

$$\overline{\mathcal{E}}_+ \approx E_0 - \frac{id^2}{\gamma}\,, \tag{3.43}$$

$$\overline{\mathcal{E}}_- \approx E_0 - i\gamma + \frac{id^2}{\gamma}\,. \tag{3.44}$$

The same result can be obtained by applying the perturbative expansion (3.41) and it shows that two unperturbed complex eigenenergies having the same real part but being distant in the imaginary axis can be robust to a perturbation, as long as the distance in the complex plane is much larger than the perturbation.

3.3.2 Robustness of superradiance to static diagonal disorder

In order to check that the previous results are valid in the model considered here beyond the perturbative regime, let us add to the the SES Hamiltonian

$$H = \sum_k E_k \left|k\right\rangle \left\langle k\right| - i\frac{\gamma}{2N}\sum_{k,k'} \left|k\right\rangle \left\langle k'\right|, \tag{3.45}$$

the static disorder

$$D = \sum_k \epsilon_k \left|k\right\rangle \left\langle k\right|\,, \tag{3.46}$$

where ϵ_k are random numbers uniformly distributed such that $\epsilon_k \in [-\xi/2, \xi/2]$. Here the parameter ξ is proportional to the standard deviation of the energy fluctuations introduced by D and it represents the disorder strength. In particular, our aim is to study the robustness of the superradiant state of the non-Hermitian case to such static disorder. In Fig. 3.5–(a) the width of the superradiant state $\Gamma_{\rm SR}$ divided by the average width $\langle\gamma\rangle = \gamma/N$ is shown *vs.* the disorder strength ξ for different values of γ larger than the critical $\gamma_{\rm cr}^{\rm NH}$. As one can see, the width of the superradiant state is larger than $\langle\gamma\rangle$ for small disorder ξ. Then, beyond some critical value of ξ, the width start to decrease with ξ, ultimately reaching $\Gamma_{\rm SR} = \langle\gamma\rangle = \gamma/N$ for $\xi \to \infty$. In order to quantify phenomenologically such critical disorder strength, let us define a critical value $\xi_{\rm cr}$ as the value of ξ beyond which the width of

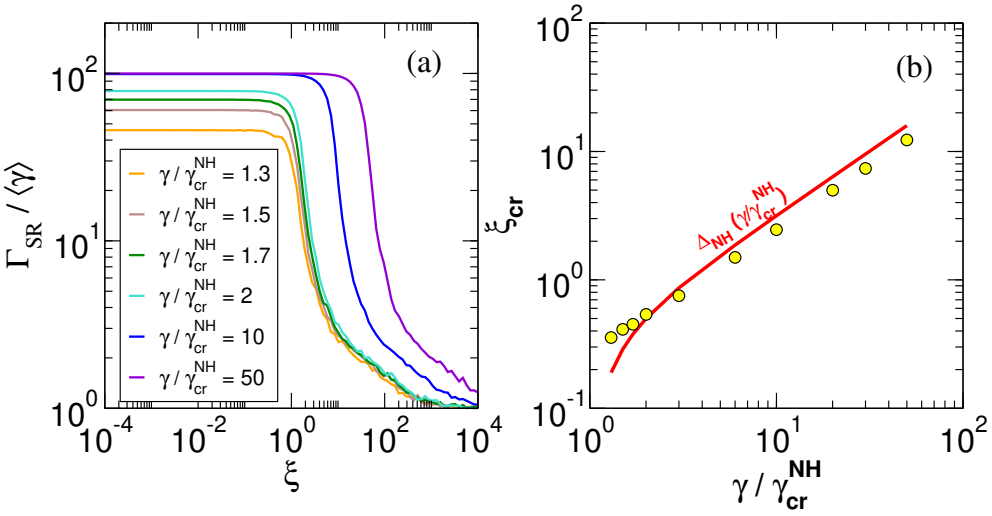

Figure 3.5: (a) Width of the superradiant state divided by the average width $\langle\gamma\rangle = \gamma/N$ *vs.* the disorder strength ξ as introduced in the Hamiltonian (3.37)-(3.45)-(3.46). (b) The critical value $\xi_{\rm cr}$ (see text) is plotted *vs.* $\gamma/\gamma_{\rm cr}^{\rm NH}$ as circles. The red line is the energy gap, as defined in Eq. (3.32). Parameters in both panels are $N = 100$, $S = 1$ and an average over 100 realizations of static disorder is performed.

the superradiant state is less than 95% of its value without disorder. In this sense, $\xi_{\rm cr}$ is proportional to the disorder strength needed to destroy superradiance. In the Fig. 3.5–(b) $\xi_{\rm cr}$ is plotted *vs.* the ratio $\gamma/\gamma_{\rm cr}^{\rm NH}$. In the same panel, the energy gap (3.32) is plotted as a comparison. As one can see, apart from small deviations where $\gamma \simeq \gamma_{\rm cr}^{\rm NH}$, the critical disorder $\xi_{\rm cr}$ increases with γ and it is approximately proportional to the non-Hermitian energy gap. This shows that the non-Hermitian energy gap makes superradiance robust to static disorder.

3.4 Relation between the gapped regime and the interaction range

In this section we want to extend our analysis to different ranges of interaction. In particular, we want to know if the emergence of the energy gap is a general outcome of long-range interactions in a PF model. Differently from the rest of the paper, here we focus only on the Hermitian case. Note that the Hermitian model is relevant in many realistic situations, such as ion traps [5, 17], where one-dimensional systems with tunable interaction range can be emulated.

We model an interaction of range α by the Hamiltonian term

$$V = -\frac{\gamma}{2v_{N,\alpha}} \sum_{\substack{k,k' \\ k\neq k'}} \frac{|k\rangle\langle k'|}{|k-k'|^{\alpha}}\,, \tag{3.47}$$

where $v_{N,\alpha}$ is a normalization constant and, since we are dealing with a one-dimensional system, we speak about "long-range interaction" for $0 \leq \alpha < 1$ and about "short-range interaction" for $\alpha > 1$. Note that in ion trap experiments [5] the exponent α can be tuned from 0 to 3. The case $\alpha = 1$ is

critical because α equals the dimension of the system and thus we will analyze it separately. The normalization constant $v_{N,\alpha}$ has been added in order to have an extensive Hamiltonian energy and to fix the spectrum of V as large as $\gamma/2$. For the case $\alpha = 0$, for example, we have $v_{N,0} = N$, which is exactly the Hermitian case studied in the previous sections. For $\alpha \neq 0$, $v_{N,\alpha}$ is determined by numerically diagonalizing V, and it has the following scaling with the system size (see Appendix A.1 for details):

$$v_{N,\alpha} \sim \begin{cases} N^{1-\alpha} & \text{for } \alpha < 1 \\ \ln N & \text{for } \alpha = 1 \\ \text{const.} & \text{for } \alpha > 1 \end{cases} . \tag{3.48}$$

In order to understand how the presence of a energy gap is connected to the range of the interaction, here we study numerically the presence of the gap Δ_{H} defined in Eq. (3.36). Let us remind that the presence of a finite and N-independent Δ_{H} in some region of γ signals the existence of an energy gap in the spectrum.

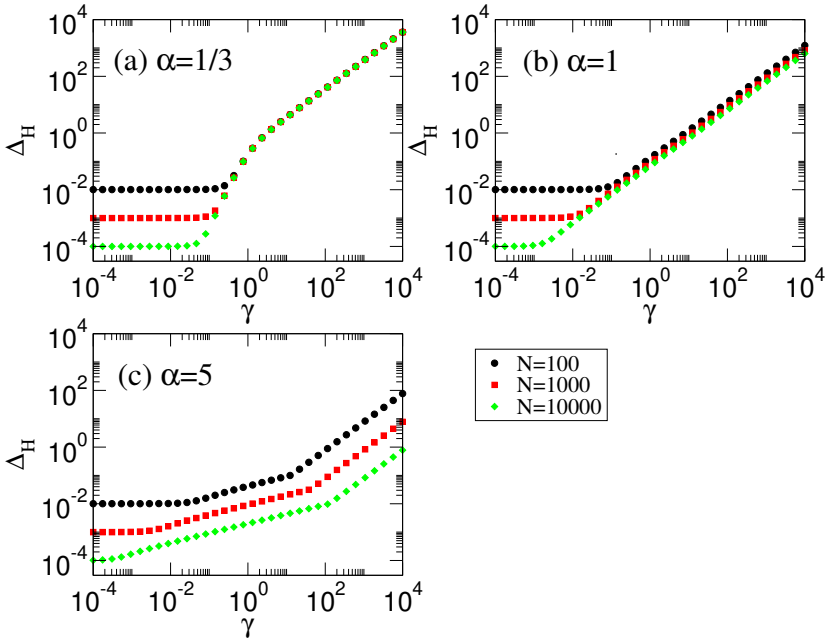

Figure 3.6: Gap Δ_{H}, as defined in (3.36), *vs.* the coupling parameter γ with the interaction (3.47). Here $S = 1$ and $N = \{100, 1000, 10000\}$.

In Fig. 3.6 we plot Δ_{H}, defined as in Eq. (3.36), as a function of γ for $\alpha = \{1/3, 1, 5\}$. The case $\alpha = 1/3$ shown in panel (a) corresponds to a long-range interaction and one can see that, similarly to the case $\alpha = 0$ (see Fig. 3.4–(b)), the energy gap is independent of the system size N for large γ. On the other hand, for short-range $\alpha = 5$ (panel (c)) Δ_{H} decreases with the system size for any value of γ and thus there is no gap for these two cases in the limit $N \to \infty$. For the critical range $\alpha = 1$ (panel (b)) the results are less clear and more analysis is needed to establish the non-existence of a gapped regime (as the data shown in the Figure seem to indicate).

From Fig. 3.6 one can see that $\gamma = 100$ represents a "strong-coupling" regime for the three values of α shown. Then, in Fig. 3.7 we plot Δ_{H} (symbols) *vs.* α for $\gamma = 100$ setting the same parameters and the same values of N as in Fig. 3.6. In Fig. 3.7 one can see two different regimes: (i) for $\alpha < 1$ (long range)) Δ_{H} is independent of N, representing a energy gap in the $N \to \infty$ limit; (ii) for $\alpha \gtrsim 1$ (short

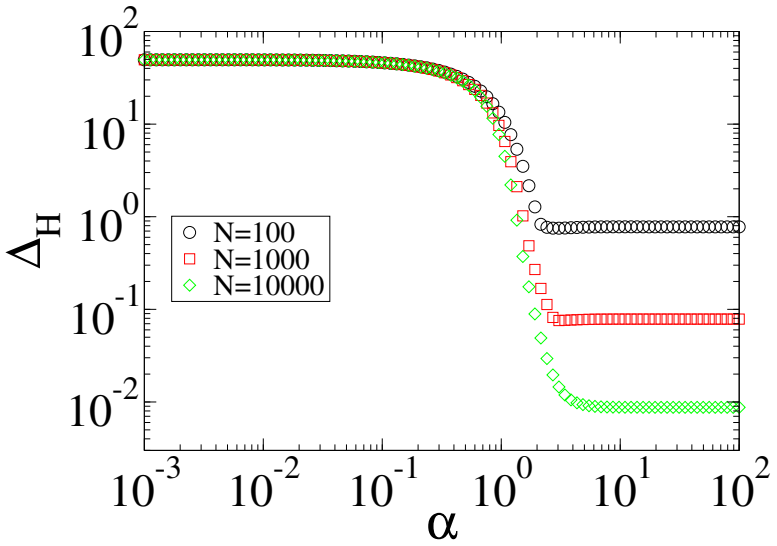

Figure 3.7: Gap Δ_{H} *vs.* the range of interaction α for $N = \{100, 1000, 10000\}$, where the symbols are given by Eq. (3.36). Here, $S = 1$ and $\gamma = 100$.

range) Δ_{H} decreases with N, meaning that there is no gap in the thermodynamic limit. Note that we checked that in the long range regime ($\alpha < 1$) the energy gap arises between the ground state and the first excited state, i.e. $\Delta_{\mathrm{H}} = E_2 - E_1$.

As a final remark we note that in this section we have analyzed the role of the interaction range just in the Hermitian case, because adding a variable range of the interaction in the non-Hermitian case is more difficult. The generalization to different ranges that we used for the Hermitian case, in fact, cannot be performed as it is for the non-Hermitian case without loss of consistency. Indeed, an imaginary interaction $V_{k,k'} = -i\gamma|k - k'|^{-\alpha}$ would lead to both positive and negative decay widths, while the decay widths of a non-Hermitian Hamiltonian are required to be all positive. Nevertheless let us note that in realistic molecular system the non-Hermitian interaction can have a complicated power law decay with the distance [61].

3.5 Conclusions of Chapter 3

We have compared two paradigmatic models for Superconductivity and Superradiance, focusing on the emergence of an energy gap in the real and complex plane, respectively. We show that an energy gap arises also in the Superradiance model in the complex plane, and we give an analytical estimate of that energy gap which agrees very well with our numerical simulations.

We show that the usual Superradiance transition can be interpreted as a transition to a gapped regime. Moreover in the large coupling limit the Superradiance and the Superconductivity gaps are mathematically the same, while they differ at criticality. Indeed, while the critical value for the emergence of Superconductivity depends on the system size, the critical value for the emergence of Superradiance is independent of the system size.

We have also shown that an energy gap in the complex plane can induce robustness to perturbations in the system, similarly to a gap in the real axis.

This result allows to interpret the robustness of Superradiance to disorder reported in several

previous publications in the literature as a consequence of the presence of an imaginary energy gap.

Finally, we analyze the role of the range of the interaction, showing that an energy gap emerges in the Hermitian system when the interaction is long-ranged.

In perspective, the relevance of these energy gaps to transport and other system properties will be analyzed. From a mathematical point of view, we have shown that the emergence of such gapped states can be connected with the long-range nature of the interaction. Indeed both the discrete BCS model and the SES model share a distance -independent coupling (all-to-all coupling). The connection of a gapped state with the long-range nature of the interaction has been also pointed out in Ref. [17].

Indeed, we analyze realistic models for quantum transport in presence of non-Hermitian and Hermitian interactions and to study the relevance of the gapped regime to the transport efficiency in Chapter 4.

Chapter 4

Transmission

In the Chapter 3 we demonstrated the emergence of a gap in the Picket-Fence model with Hermitian and non-Hermitian couplings. After a general introduction of the Anderson model, which is a tight-binding model in presence of onsite disorder where we define the finite size critical disorder in a linear chain in section 4.1.

We show the emergence of the energy gaps in this paradigmatic model for quantum transport in presence of additional long-range all-to-all hoppings for small and large disorder strengths in section 4.2. The all-to-all Hermitian coupling or the all-to-all non-Hermitian coupling are both realistic. For the Hermitian case such a coupling can be realized for instance in ion-traps [5], while for the non-Hermitian case one can think of a molecular chain in the small volume limit when the wavelength is much larger than the system size [61] (even if in this case, also Hermitian dipole-dipole terms would appear).

Thus, we introduce the mathematical formalism of the transmission in a linear chain and we derived an equation for the integrated transmission, we also present the general equation for variance of the eigenstates and the dynamical variance in a stationary distribution in section 4.3.

In sections 4.4 and 4.5, we study the transport properties for the Hermitian and non-Hermitian couplings with the figures of merit for transport that we analyze below in presence of the energy gap. We explain the different disorder regimes which emerge using the shape of the eigenfunctions for both couplings and we also derived expresions for the hybrid eigenstates which emerges in the superradiant regime using perturbation theory for the Hermitian coupling.

4.1 Anderson Model

Here we briefly review the Anderson model and the definition of the Anderson localization [62].

The Anderson model describes a particle which hops between neighbors sites of a linear chain with N sites in the presence of onsite disorder [16]. The Hamiltonian H_0 for the Anderson model can be written as

$$H_0 = \sum_{j=1}^{N} E_j \left|j\right\rangle \left\langle j\right| + \Omega \sum_{j=1}^{N-1} \left(\left|j\right\rangle \left\langle j+1\right| + \left|j+1\right\rangle \left\langle j\right|\right), \tag{4.1}$$

where E_i are random variables uniformly distributed in $[-\mathrm{W}/2, \mathrm{W}/2]$, W is the disorder parameter and Ω is the tunneling transition amplitude to nearest neighbors sites.

In this study, we assume a constant tunneling transition amplitude, i.e. $\Omega = 1$. In Fig. 4.1 we show a scheme of the Anderson model with N sites where the self-energies E_j are random.

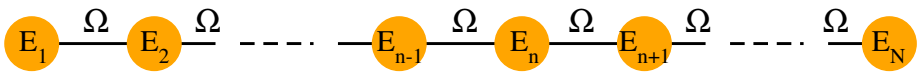

Figure 4.1: Scheme of a linear chain in the Anderson model with length N. The black lines represent the tunneling transition amplitude Ω and the orange circles are the sites in the linear chain with random self-energy E_n.

In the absence of disorder, $\mathrm{W} = 0$, the linear chain is ordered and the eigenstates are extended wave functions with the form [16]

$$\Psi_q(j) = \sqrt{\frac{2}{N+1}} \sin\left(\frac{\pi q}{N+1} j\right) \tag{4.2}$$

and the eigenvalues

$$E_q = -2\Omega \cos\left(\frac{\pi q}{N+1}\right), \tag{4.3}$$

where $q = 1, \ldots, N$ is a quantum number and $j = 1, \ldots, N$ is a discrete coordinate. In this case, the eigenvalues lie in the interval $[-2\Omega, 2\Omega]$ and the mean level spacing can be estimated as $D = 4\Omega/N$.

If $\mathrm{W} \neq 0$ the structure of the eigenstates change drastically: a 1D tight-binding chain with a random diagonal potential will cause all the eigenstates of the system to get localized exponentially, The envelope of the eigenstates $\Psi_q(j)$ decays exponentially from some point j_0 in space [63] as:

$$|\Psi_q(j)| \sim \exp\left(-\frac{|j - j_0|}{\xi}\right), \tag{4.4}$$

where ξ is the localization length of the eigenstate $\Psi_q(j)$. Even if all eigenstates are localized in the 1D Anderson model, for finite sizes, we can consider that the eigenstates are extended if $\xi > N$, while they are localized if $\xi < N$. From $\xi = N$ we can define a system size-dependent critical disorder $\mathrm{W}_{\mathrm{cr}}^{\mathrm{AT}}$.

For the 1D Anderson model with weak disorder, Thouless was the first to obtain a closed expression for ξ in terms of the variance σ^2 of the site energies distribution [64] as follows:

$$\xi = \frac{8(1 - (E/2\Omega)^2)}{\sigma^2}\Omega^2 . \tag{4.5}$$

The relation (4.5) is valid everywhere apart from the vicinity of the band edges $|E| = 2\Omega$ and the $E = 0$. In the case of an uniform distribution in $[-\mathrm{W}/2, \mathrm{W}/2]$ we have that the variance $\sigma^2 = \langle E_j^2 \rangle = \mathrm{W}^2/12$. For the energy $E = 0$ the Eq. (4.5) has the following expression [65]:

$$\xi(E = 0) = 105.2 \left(\frac{\Omega}{W}\right)^2 . \tag{4.6}$$

Using Eq. (4.6) and the condition for the critical disorder ($\xi = N$) we have a finite size critical disorder $\mathrm{W}_{\mathrm{cr}}^{\mathrm{AT}}$:

$$\mathrm{W}_{\mathrm{cr}}^{\mathrm{AT}} = \sqrt{\frac{105.2}{N}}\Omega \tag{4.7}$$

where Ω is the tunneling transition amplitude to nearest neighbor sites and N is the system size of the chain.

4.2 Anderson Model with long range hopping

Here we analyze the 1D Anderson model in presence of long range all-to-all hopping. For this purpose we add the coupling V_0 in the Hamiltonian (4.1) where the coupling V_0 can be real or imaginary. The total Hamiltonian H can be written as

$$H = \sum_{j=1}^{N} E_j \left|j\right\rangle \left\langle j\right| + \Omega \sum_{j=1}^{N-1} \left(\left|j\right\rangle \left\langle j+1\right| + \left|j+1\right\rangle \left\langle j\right|\right) - V_0 \sum_{j,j'} \left|j\right\rangle \left\langle j'\right| \tag{4.8}$$

Here, the Hermitian coupling $V_0 = \gamma/2$ is a real number and the non-Hermitian coupling $V_0 = i\gamma/2$ is a pure imaginary number where γ is the strength of the coupling for both cases.

4.2.1 Energies gaps

Here we analyze the emergence of an energy gap in the Anderson model with the addition of long range hopping. In order to analyze the emergence of an energy gap we follow the same procedure we used in Chapter 3. For the non-Hermitian coupling, see (3.29)-(3.30), we can define the gap as:

$$\Delta_{\mathrm{NH}} = \max_{i} \left\{ \min_{j \neq i} \left[\mathrm{dist}\left(\mathcal{E}_i, \mathcal{E}_j\right) \right] \right\} \tag{4.9}$$

where the distance in the complex plane between two eigenvalues is

$$\mathrm{dist}\left(\mathcal{E}_i, \mathcal{E}_j\right) = \sqrt{\left(E_i - E_j\right)^2 + \frac{1}{4}\left(\Gamma_i - \Gamma_j\right)^2}\,. \tag{4.10}$$

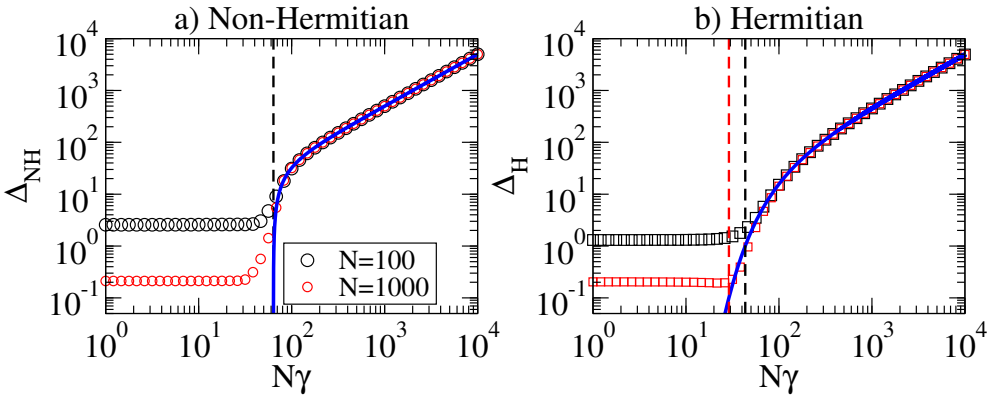

Figure 4.2: a) Gap Δ_{NH}, *vs.* the coupling parameter $N\gamma$. Symbols are computed numerically using the expressions (4.9)-(4.10), while the continuous blue curve shows the analytical estimate (3.32). The dashed vertical line marks the critical coupling strength $\gamma_{\mathrm{cr}}^{\mathrm{NH}}$ from Eq. (3.34). b) Gap Δ_{H}, *vs.* the coupling parameter $N\gamma$. Symbols are given by (4.11) while the continuous blue curve shows the analytical estimate (3.17). The dashed vertical lines indicate the critical coupling strength $\gamma_{\mathrm{cr}}^{\mathrm{H}}$ from Eq. (3.20). Here, $\mathrm{W} = 100$, $N = \{100, 1000, 4000\}$ and the number of disorder configurations is $N_r = 100$.

For the Hernmitian coupling, see (3.36), the gap is defined as follow:

$$\Delta_{\mathrm{H}} = \max_{i} \left\{ \min_{j \neq i} \left[\mathrm{dist}\left(E_i, E_j\right) \right] \right\} , \tag{4.11}$$

where $\mathrm{dist}\left(E_i, E_j\right) = |E_i - E_j|$ is the distance in the real axis.

We compute numerically the Eqs. (4.9) and (4.11) for each disorder configuration and then we average over the different disorder realization.

In Fig. 4.2 we show the energy gap $\Delta_{\mathrm{H,NH}}$, both for the Hermitian and non-Hermitian coupling, as a function of the coupling strength $N\gamma$ for different system sizes N and for the disorder $\mathrm{W} = 100$. For small couplings strength γ, the energy gaps $\Delta_{\mathrm{H,NH}}$ goes to zero as the system size N increases, on the other hand, for large coupling strength γ, the gap is independent of N above the critical coupling strength $\gamma_{\mathrm{cr}}^{\mathrm{H,NH}}$ (3.20) and (3.34). In this regime, the analytical expressions, see Eqs. (3.17) and (3.32), for the energy gaps $\Delta_{\mathrm{H,NH}}$ obtained in the Picket-Fence model are valid also for this model, in the case of large disorder, see continuous curves in Fig. 4.2.

In Fig. 4.3 we show the energy gap $\Delta_{\mathrm{H,NH}}$, both for the Hermitian and non-Hermitian coupling, as a function of the coupling strength $N\gamma$ for the small disorder $\mathrm{W} = 1$.

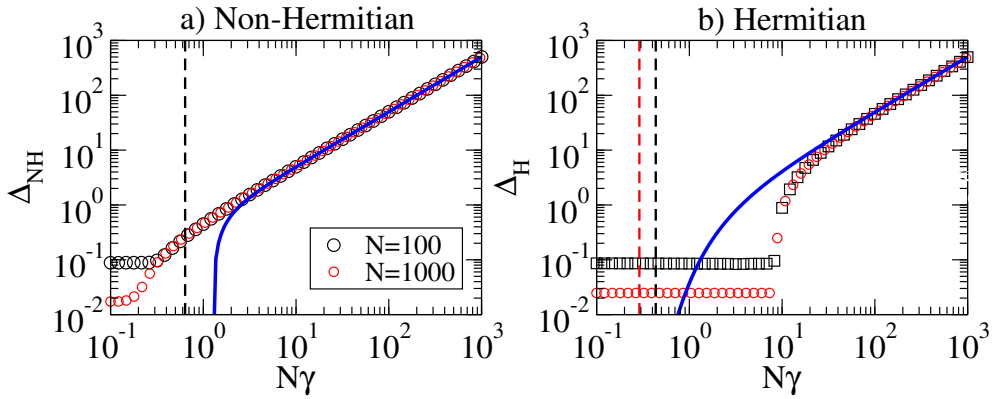

Figure 4.3: a) Gap Δ_{NH}, *vs.* the coupling parameter $N\gamma$. Symbols are given by (4.9)-(4.10), while the continuous blue curve shows the analytical estimate (3.32) using $\mathrm{S} = 2\Omega$. The dashed vertical line marks the critical coupling strength $\gamma_{\mathrm{cr}}^{\mathrm{NH}}$ from Eq. (3.34). b) Gap Δ_{H}, *vs.* the coupling parameter $N\gamma$. Symbols are given by (4.11) while the continuous blue curve shows the analytical estimate (3.17) using $\mathrm{S} = 2\Omega$. The dashed vertical lines indicate the critical coupling strength $\gamma_{\mathrm{cr}}^{\mathrm{H}}$ from Eq. (3.20). Here, $\mathrm{W} = 1$, $N = \{100, 1000\}$ and the number of disorder configurations is $N_r = 100$.

Here, the numerical results show deviations from the analytical equations around the critical coupling $\gamma_{\mathrm{cr}}^{\mathrm{H,NH}}$. On the other side, for large coupling strength, the analytical expression are still correct.

We demonstrated that the same type of gap that arises in the Picket-Fence model, also arises in this paradigmatic model when we add a Hermitian or non-Hermitian all-to-all couplings. In fact, in the large disorder limit, we find that the same formulas (3.17) and (3.32) for the gap in the Picket-Fence model can be applied in the Anderson model as we can see in the Fig. 4.2. In contrast, for small disorders we obtain deviations from these formulas around the critical disorder, as we can see in Fig. 4.3.

4.3 Tranport properties

Here we describe the figure of merit we used to characterize the transport properties of the system, such as the integrated transmission and the variance of the eigenstates.

4.3.1 Transmission

Transmission can be studied by coupling the first and the last site of the chain (i.e. sites 1 and N) to two different leads with coupling strength ν, so that the components of the Hamiltonian read [37]

$$(H_{\text{eff}})_{k,l} = (H)_{k,l} - \frac{i}{2}\nu(\delta_{k,1}\delta_{l,1} + \delta_{k,N}\delta_{l,N})\,, \tag{4.12}$$

where H is given in Eq. (4.8).

A pictorial representation of our transmission set-up is shown in Fig. 4.4, where it is shown an excitation which can hop among the chain sites.

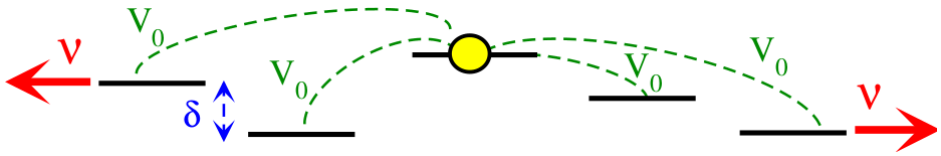

Figure 4.4: Pictorial representation of the transmission set-up. The black lines represent the Anderson model spectrum with a random level spacing δ while the yellow circle is an excitation which can hop to all the other states with an amplitude V_0 (green dashed lines). The excitation can then be collected by the leads at the edge states with an amplitude ν.

In general, the transmission $T^{a,b}(E)$ from channel a to channel b can be determined [37]:

$$T^{a,b}(E) = |Z^{a,b}(E)|^2 \tag{4.13}$$

where

$$Z^{a,b}(E) = \sum_{i,j=1}^{N} A_i^a \left(\frac{1}{E - H_{\text{eff}}}\right)_{i,j} A_j^b \tag{4.14}$$

is the transmission amplitude, H_{eff} is the effective non-Hermitian Hamiltonian in Eq. (4.12) and A_i^a are the decay amplitudes from the discrete internal states i to external states a. We can also write $T^{a,b}(E)$ in a different way, diagonalizing the Hamiltonian H_{eff}. Its eigenfunctions $|r\rangle$ and $\langle\tilde{r}|$ form a bi-orthogonal complete set,

$$H_{\text{eff}}\,|r\rangle = \mathcal{E}_r\,|r\rangle \quad \langle\tilde{r}|\,H_{\text{eff}} = \langle\tilde{r}|\,\mathcal{E}_r^*, \tag{4.15}$$

and its eigenenergies are complex numbers with the form

$$\mathcal{E}_r = E_r - \frac{i}{2}\Gamma_r\,, \tag{4.16}$$

corresponding to resonances centered at the energy E_r with the decay widths Γ_r. The decay amplitudes A_i^a are transformed according to

$$\mathcal{A}_r^a = \sum_i A_i^a \langle i|r\rangle \,, \quad \tilde{\mathcal{A}}_r^b = \sum_j \langle \tilde{r}|j\rangle \, A_j^b \;\; , \tag{4.17}$$

and the transmission amplitude $Z^{a,b}(E)$ are given by

$$Z^{a,b}(E) = \sum_{r=1}^{N} \mathcal{A}_r^a \frac{1}{E-\mathcal{E}_r} \tilde{\mathcal{A}}_r^b \,. \tag{4.18}$$

Note that the complex eigenvalues $\mathcal{E}$ of H_{eff} coincide with the poles of the transition amplitude $Z(E)$.

Since the excitation is collected by the leads at the edges of the chain, the amplitudes in Eq. (4.17) are $\mathcal{A}_r^a = \sqrt{\nu}\Psi_r^1$ and $\tilde{\mathcal{A}}_r^b = \sqrt{\nu}\Psi_r^{N*}$, i.e. the amplitude $\mathcal{A}_r^a$ is $\sqrt{\nu}$ times the first or the last component of the eigenfunction of the state r in the non-Hermitian Hamiltonian H_{eff} in Eq. (4.12). Moreover, the transmission amplitude $Z^{a,b}(E)$ in Eq. (4.18) becomes

$$Z^{a,b}(E) = \nu \sum_{r=1}^{N} \frac{\Psi_r^1 \Psi_r^{N*}}{E-\mathcal{E}_r} \tag{4.19}$$

where $\mathcal{E}_r = E_r - \frac{i}{2}\Gamma_r$. The conjugate of the transmission amplitude $Z^{a,b}(E)$ is

$$Z^{a,b}(E)^* = \nu \sum_{k=1}^{N} \frac{\Psi_k^{1*} \Psi_k^{N}}{E-\mathcal{E}_k^*} \tag{4.20}$$

and the transmission $T^{a,b}(E) = |Z^{a,b}(E)|^2 = Z^{a,b}(E) Z^{a,b}(E)^*$ is

$$T^{a,b}(E) = \nu^2 \sum_{r=1}^{N}\sum_{k=1}^{N} \frac{\Psi_r^1 \Psi_k^{1*} \Psi_k^N \Psi_r^{N*}}{(E-\mathcal{E}_r)(E-\mathcal{E}_k^*)} \,. \tag{4.21}$$

Let us integrate the Eq. (4.21) over all the energies, i.e. $T_{\text{int}} = \int_{-\infty}^{\infty} dE\, T^{a,b}(E)$. So, we get the integrated transmission T_{int} with the following expression

$$\begin{aligned} T_{\text{int}} &= \nu^2 \sum_{r=1}^{N}\sum_{k=1}^{N} \Psi_r^1 \Psi_k^{1*} \Psi_k^N \Psi_r^{N*} \int_{-\infty}^{\infty} \frac{dE}{(E-\mathcal{E}_r)(E-\mathcal{E}_k^*)} \\ &= 2\pi\nu^2 \sum_{r=1}^{N}\sum_{k=1}^{N} \frac{\Psi_r^1 \Psi_k^{1*} \Psi_k^N \Psi_r^{N*}}{(\Gamma_r+\Gamma_k)/2 - i(E_k - E_r)} \,. \end{aligned} \tag{4.22}$$

Let us note that the Eq. (4.22) is exact and it depends only with the amplitudes of the eigenfunctions at the edges of the chain and the complex eigenvalues $\mathcal{E}_r$ of H_{eff}. The integrated transmission T_{int} represents the overall transmission over a wide spectral energy band and for instance it is relevant for analyzing the transport under a large applied voltage: the shape of the current-voltage characteristic can sometimes be significantly different depending on the potential profile or the voltage drop. This is important in determining the maximum current of a transistor. [66].

For more detail of how the Eq. (4.22) depends with the coupling strength γ and the system size N see the appendix C.

4.3.2 Variance of the eigenstates

Another important figure of merit for the transport properties of the system is the average variance $\sigma^2(x)$ of the probability distributions in space of all the eigenstates of the Hamiltonian in Eq. (4.8).

The average variance is defined as $\sigma^2(x) = \frac{1}{N}\sum_{\alpha=1}^{N}\sigma_\alpha^2(x)$ where $\sigma_\alpha^2(x) \equiv \langle x_\alpha^2\rangle - \langle x_\alpha\rangle^2$. Note that the average square position and average position can be computed as:

$$\langle x_\alpha^2\rangle = \frac{\sum_i i^2 \mid \langle i|\alpha\rangle \mid^2}{\sum_i \mid \langle i|\alpha\rangle \mid^2}, \qquad \langle x_\alpha\rangle = \frac{\sum_i i \mid \langle i|\alpha\rangle \mid^2}{\sum_i \mid \langle i|\alpha\rangle \mid^2}\ . \tag{4.23}$$

where $|\alpha\rangle$ is a system eigenstate and the states $|i\rangle$ represent the site basis.

For the Hermitian case, we also compute the variance from dynamics considering an excitation localized on a single site in the middle of the chain and we simulate the dynamical evolution of the system numerically. The spread the initial localized excitation will reach a stationary distribution, from which we compute the variance of the position operator. For the expectation value of any operator A we can write:

$$\langle A\rangle = \langle\psi(t)|A|\psi(t)\rangle = \sum_{E,E'}\langle E|A|E'\rangle\langle E|\psi(0)\rangle\langle\psi(0)|E'\rangle e^{-i(E-E')t/\hbar}$$

The stationary value of $\langle A\rangle$ can be written as:

$$\langle A\rangle = \sum_E \langle E|A|E\rangle|\langle E|\psi(0)\rangle|^2$$

From the last expression, we have that if the fluctuations of the operator A for different eigenstates are negligible, then we can write:

$$\lim_{t\to\infty}\langle\psi(t)|A|\psi(t)\rangle = \frac{1}{N_E}\sum_E\langle E|A|E\rangle$$

where the last term represents an average over the eigenstates in a certain energy interval. If the characteristics of the eigenstates are uniform, than we can consider the average over all the eigenstates as we will do below.

Note that the average variance of all the eigenstates represents the variance of the stationary distribution obtained dynamically from the spreading of an initial excitation localized on a chain site.

From now, we will analyze the quantum transport properties in the Anderson model for both Hermitian and non-Hermitian coupling. We will analyze the consequences of the emergence of the energy gaps using on quantum transport using both the integrated transmission and the average variance of the eigenstates as figure of merit of transport efficiency. First, we will study the Hermitian coupling in Sec. 4.4 and then we will focus on the non-Hermitian coupling in Sec. 4.5.

4.4 Hermitian case

For the Hermitian coupling where $V_0 = \gamma/2$, the components of the effective Hamiltonian read:

$$(H_{\text{eff}})_{k,l} = (H_0)_{k,l} - \frac{\gamma}{2} - \frac{i}{2}\nu(\delta_{k,1}\delta_{l,1} + \delta_{k,N}\delta_{l,N})\,, \tag{4.24}$$

where H_0 is the Hamiltonian in the Anderson model in Eq. (4.1), the second term represents the off-diagonal Hermitian hopping with coupling strength γ and the third term represents the coupling strength ν to the leads.

4.4.1 Integrated transmission and the variance of the eigenstates

Here we analyze the transport properties of the Hermitian long range system as a function of disorder strength W. We will compare the transport properties (integrated transmission $T_{\rm int}$ and variance $\sigma^2(x)$ of all the eigenstates) with the transport properties of the Anderson model without the all-to-all coupling strength γ, where disorder strength W is known to induce an exponentially suppressed transmission above the finite size Anderson transition critical disorder $\mathrm{W}_{\rm cr}^{\rm AT}$, see Eq. (4.7).

We show that in presence of long range hopping, the emergence of an energy gap $\Delta_{\rm H}$ can donate robustness to disorder to the transport properties of the system. For instance, the transmission of the gapped ground state remains perfect, see appendix B, up to the critical disorder for which the energy gap $\Delta_{\rm H}$ disappears, which is $\mathrm{W}_{\rm cr}^{\rm H} = \gamma N \ln N/2$. Most interestingly, we will show that the presence of an energy gap $\Delta_{\rm H}$ in the ground state is able to donate robustness also to the excited states of the system. Moreover we will show the emergence of different transport regimes in different disorder ranges.

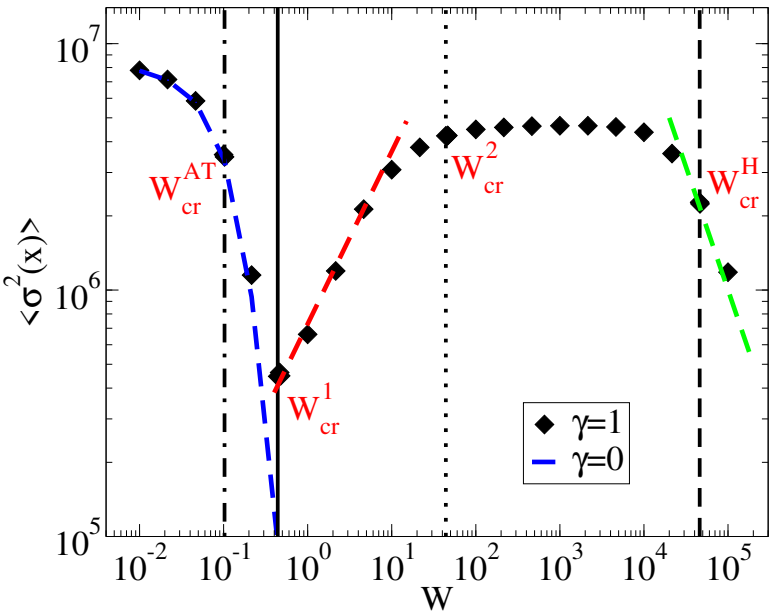

Figure 4.5: Average variance $\langle\sigma^2(x)\rangle$, see section 4.3.2, *vs.* disorder strength W for the coupling strength $\gamma = 1$ and the system size $N = 10000$. Here, $\Omega = 1$, $\nu = 0$, $N_r \times N = 10^5$ where N_r is the number of disorder configurations. The vertical lines mark the critical disorders strength $\mathrm{W}_{\rm cr}^{\rm AT}$, $\mathrm{W}_{\rm cr}^{1}$, $\mathrm{W}_{\rm cr}^{2}$ or $\mathrm{W}_{\rm cr}^{\rm H}$, see the description in section 4.4.2. The dashed blue curve shows the results for the Anderson model without long range hopping, $\gamma = 0$. The dashed red line goes like $\mathrm{W}^{0.7}$ and the dashed green line goes like W^{-1}.

4.4.1.1 Variance of the eigenstates

In Fig. 4.5 we show the average variance $\langle\sigma^2(x)\rangle$ as a function of the disorder strength W. The average variance has been computed over all the eigenstates, including the ground state. The parameters for the simulations were: system size $N = 10000$, coupling strength $\gamma = 1$ and the coupling strength to the leads $\nu = 1$. For this choice of parameters and in absence of disorder, we are in the gapped regime with an energy gap $\Delta_{\mathrm{H}} = 5000$ for $\mathrm{W} = 0$. As we increase the disorder W a transition to a non-gapped regime will occur at $\mathrm{W}_{\mathrm{cr}}^{\mathrm{H}} \approx 432051.70$, as mentioned above. The numerical results were obtained using Eq. (4.23) for the variance $\sigma^2(x)$.

Let's show the general behavior of the variance $\sigma^2(x)$ as the disorder strength W increases. We can observe 5 different transport regimes in Fig. 4.5 described below

1. For weak disorder $\mathrm{W} < \mathrm{W}_{\mathrm{cr}}^{\mathrm{AT}}$, the variance $\sigma^2(x)$ is very large and strongly dependent on disorder strength W.

2. Above the finite size Anderson transition critical disorder $\mathrm{W}_{\mathrm{cr}}^{\mathrm{AT}}$, the variance $\sigma^2(x)$ decays like in the Anderson model, see dashed blue curve, up to a critical disorder $\mathrm{W}_{\mathrm{cr}}^{1}$, at which the variance reaches a local minimum. We will define this critical disorder later.

3. For the disorder $\mathrm{W} > \mathrm{W}_{\mathrm{cr}}^{1}$, the variance $\sigma^2(x)$ increases with the disorder strength approximately as $\mathrm{W}^{0.7}$, up to another critical disorder $\mathrm{W}_{\mathrm{cr}}^{2}$, at which the variance reaches a plateau and it becomes independent of disorder. We will define this disorder threshold later.

4. The variance $\sigma^2(x)$ remains independent of the disorder up to the critical disorder strength $\mathrm{W}_{\mathrm{cr}}^{\mathrm{H}}$. Above this critical disorder the energy gap disappears [15].

5. Finally, we have the regime where the variance $\sigma^2(x)$ decreases as the disorder strength W increases. For $\mathrm{W} > \mathrm{W}_{\mathrm{cr}}^{\mathrm{H}}$, $\sigma^2(x)$ decays approximately as W^{-1}. This disorder range corresponds to the non-gapped regime.

4.4.1.2 Integrated transmission

In Fig. 4.6 we show the average integrated transmission $\langle T_{\mathrm{int}}\rangle$ as a function of the disorder strength W. The average integrated transmission $\langle T_{\mathrm{int}}\rangle$, see section 4.3.1. In Fig. 4.6, the same parameters of Fig. 4.5 have been used. The numerical results were obtained using Eq. (4.22).

We observe 5 different transport regimes also in Fig. 4.6 similarly to what we observed for the variance in Fig. 4.5. The different transport regimenes are described below:

1. For weak disorder, below of the disorder $\mathrm{W} < \mathrm{W}_{\mathrm{cr}}^{\mathrm{AT}}$ the integrated transmission T_{int} is large and weakly dependent on disorder strength W, see Fig. 4.6.

2. Above the finite size Anderson transition critical disorder $\mathrm{W}_{\mathrm{cr}}^{\mathrm{AT}}$, the integrated transmission T_{int} decays like in the Anderson model, see the dashed blue curve, up to the critical disorder $\mathrm{W}_{\mathrm{cr}}^{1}$, at which the integrated transmission T_{int} reaches a local minimum. We will define this critical disorder later.

3. For the disorder $\mathrm{W} > \mathrm{W}_{\mathrm{cr}}^{1}$, the integrated transmission T_{int} increases with the disorder strength W approximately as $\mathrm{W}^{0.3}$, up to the critical disorder $\mathrm{W}_{\mathrm{cr}}^{2}$. We will define this critical disorder later.

4. Then, we observe the regime where the integrated transmission T_{int} is independent of the disorder strength W up to the critical disorder $\mathrm{W}_{\mathrm{cr}}^{\mathrm{H}}$.

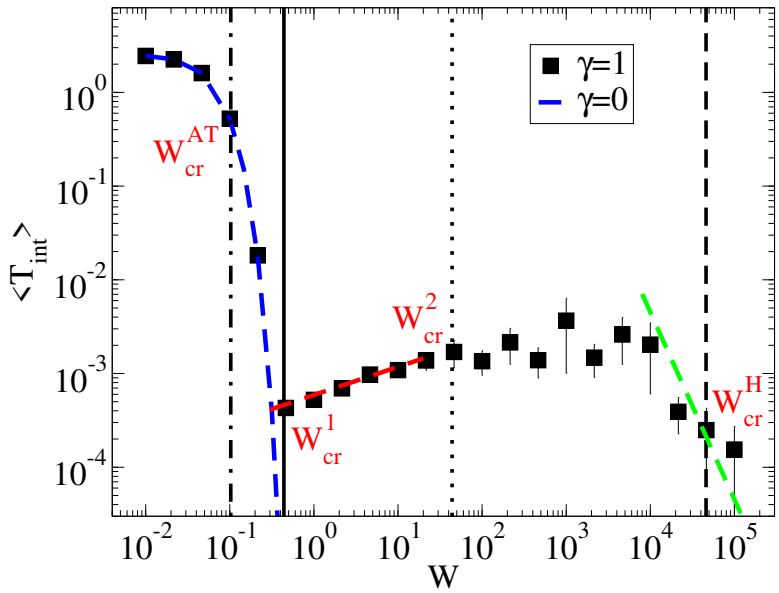

Figure 4.6: Average integrated transmission $\langle T_{\rm int}\rangle$ *vs.* the disorder strength W for the coupling strength $\gamma = 1$ and the system size $N = 10000$. Here, $\Omega = \nu = 1$, $N_r \times N = 5 \times 10^5$ where N_r is the number of disorder configurations. The vertical lines mark the critical disorders strength $\mathrm{W}_{\rm cr}^{\rm AT}$, $\mathrm{W}_{\rm cr}^{1}$, $\mathrm{W}_{\rm cr}^{2}$ or $\mathrm{W}_{\rm cr}^{\rm H}$, see the description in section 4.4.2. The dashed blue curve shows the results for the Anderson model without long range hopping, $\gamma = 0$. The dashed red line goes like $\mathrm{W}^{0.3}$ and the dashed green line goes like W^{-2}.

5. We have the regime where the integrated transmission $T_{\rm int}$ decreases as the disorder strength W increases. For $\mathrm{W} > \mathrm{W}_{\rm cr}^{\rm H}$, $T_{\rm int}$ decays approximately as W^{-2}. This disorder range corresponds to the non-gapped regime.

To summarize the results presented in this section, we can say that the behavior of the variance $\sigma^2(x)$ and of the integrated transmission $T_{\rm int}$ for the case of the Anderson model in presence of long rage hopping is very different from the behavior of the Anderson model without the long range hopping. Indeed for the Anderson model with $\gamma = 0$, see dashed blue curves in Figs. 4.5 and 4.6, $T_{\rm int}$ and the variance $\sigma^2(x)$ decay exponentially with the disorder. On the other hand, for $\gamma > 0$ these physical quantities do not decay exponentially above the critical disorder $\mathrm{W}_{\rm cr}^{1}$; in fact, we observe an improvement for $T_{\rm int}$ and $\sigma^2(x)$, as the disorder strength W increases, which is very counter-intuitive. Most interestingly, we also observe a disorder range below the critical disorder $\mathrm{W}_{\rm cr}^{\rm H}$ where $T_{\rm int}$ and $\sigma^2(x)$ are independent of the disorder.

4.4.2 Relationship between shape of eigenfunctions and transport properties

The analysis of the shape of the eigenfunctions will be essential to understand the transport properties of the system. Moreover, this analysis will allow us to to explain the different transport regimes discussed above and to analytically estimate the different critical disorders discussed in the previous section.

The dependence of the shape of the eigenfunctions on the disorder strength W in our model is much richer than what we have in the Anderson model in absence of long range hopping. Indeed in

the 1D Anderson model, the eigenfunctions are always exponentially localized, even if below the finite size Anderson transition critical disorder W_{cr}^{AT}, the localization length ξ is larger than the system size N, so that they behave as effectively extended wave functions. On the other hand, for $W > W_{cr}^{AT}$ their localized character fully emerges.

The situation is very different in presence of long range hopping as it has been recently reported in literature. For instance, the shape of eigenfunctions in 1D and 3D Anderson models with the addition of all-to-all non-Hermitian couplings, have been already analyzed in Refs. [16]. In the superradiant regime and above the finite size Anderson transition critical disorder W_{cr}^{AT}, the subradiant states of the system have been shown to have an hybrid nature, with an exponentially localized peak and an extended tail. The exponentially localized peak is identical to exponentially localized peak which characterizes the Anderson model without long range hopping. On the other side, the extended tail represent a plateau in the probability distribution of the eigenfunctions and it decreases as $1/N$ as we increase the system size N in the superradiant regime. Most interestingly, the plateau is independent of the disorder strength W in the superradiant regime.

Here we analyze in details how the shape of the eigenfunctions changes as a function of disorder. As we discussed in the previous Chapter the regime corresponding to the superradiant one in case of Hermitian coupling is the gapped regime, where the ground state plays the role of the superradiant state, while the excited states play the role of the subradiant states. We will show that in the gapped regime, the excited states have an hybrid nature, similarly to the subradiant states in Ref. [16].

For this purpose, we study the shape of the eigenfunctions $|\Psi\rangle$ in the site basis for different disorders, fixed γ and N and no coupling to the leads, i.e. $\nu = 0$.

The shape of the eigenfunctions have been obtained for each disorder configuration as follows:

1. We diagonalize the Hamiltonian (4.24),
2. We consider those eigenfunctions peaked within the 20% of sites around the middle of the chain.
3. We shift the position of those maximum values in the eigenfunctions so that all coincide.
4. We determine the average shape of the eigenfunctions by averaging their probability distributions.

In Fig. 4.7 we show the average shape of the eigenfunctions $\langle|\Psi|^2\rangle$ in the site basis k for the coupling strength $\gamma = 1$, system size $N = 100$ and different disorders W indicated in the legends. For the largest disorder shown in each panel, we also show the shape of the eigenfunctions for the Anderson model with $\gamma = 0$. By analyzing the shape of the eigenfunctions we can identify different disorder regimes which will be relevant to understand the transport properties of the system as we showed in the previous section.

We can identify the following disorder regimes:

1. ($W < W_{cr}^{AT}$) Below the finite size Anderson transition critical disorder, the localization length ξ of the eigenfunctions is larger than the systems size N, i.e. $\xi > N$, so that eigenfunctions are delocalized. The shape of the eigenfunctions is similar to the Anderson model in the absence of long-range coupling, see Fig. 4.7–(a).
2. ($W_{cr}^{AT} < W < W_{cr}^{1}$) Above the finite size Anderson transition critical disorder, the exponential peak becomes visible and the tails of the eigenfunctions decay more exponentially as the disorder strength W increases, see the vertical black arrow in Fig. 4.7–(b). In this regime the shape of the eigenfunctions are similar to the shape of the eigenfuctions of the standard Anderson model, up to a critical disorder strength. We can define this second critical disorder W_{cr}^{1} taking into consideration that the eigenfuctions of the excited states have an hybrid caracther as discovered in Ref. [16]. Indeed they present an exponentially localized peak with the same localization

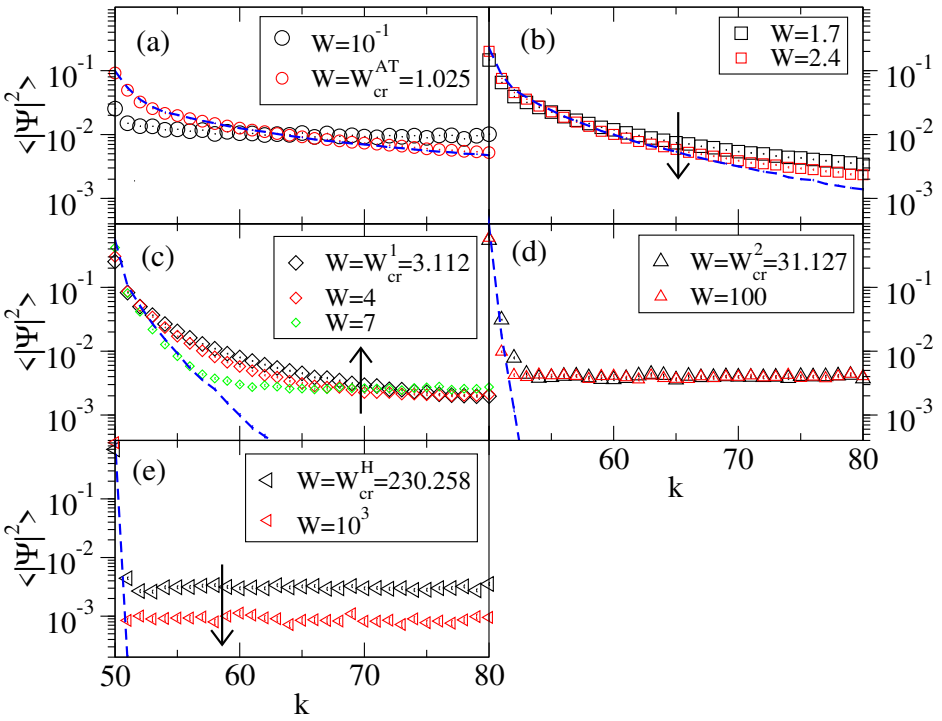

Figure 4.7: Average shape of the eigenfunctions $\langle|\Psi|^2\rangle$ *vs.* the site basis k. In each panel, different disorder regimes are shown: (a) $W \leq W_{cr}^{AT}$, (b) $W_{cr}^{AT} < W < W_{cr}^{1}$, (c) $W_{cr}^{1} \leq W < W_{cr}^{2}$, (d) $W_{cr}^{2} \leq W < W_{cr}^{H}$ and (e) $W \geq W_{cr}^{H}$. Here, $N = 100$, $\Omega = \gamma = 1$, the number of disorder configurations is $N_r = 1000$. The dashed blue curves indicate the shape of eigenfunctions for $\gamma = 0$.

length of the standard Anderson model, and an extended tail which decreases with the system size as $1/N$. Thus, we can estimate the critical disorder strength for which the eigenfuctions of the Anderson model with long range hopping will differ from the eigenfuction of the standard Anderson model, by finding the disorder strength for which the probability of the exponentially localized peak at the chain edges becomes equal to probability in the plateau. Considering that the plateau in the gapped regime decreases as $1/N$ and considering that the exponential peak at the chain edges is given by $\exp(-N/2\xi)$, we can determine W_{cr}^{1} by the following equation:

$$\exp\left(-\frac{N}{2\xi}\right) \approx \frac{1}{N} \Rightarrow -\frac{N}{2\xi} \approx -\ln N, \tag{4.25}$$

where the localization length ξ for $E = 0$ [65] is

$$\xi(E=0) = 105.2\left(\frac{\Omega}{W}\right)^2, \tag{4.26}$$

so that Eq. (4.25) becomes

$$-\frac{N}{210.4}\left(\frac{W_{cr}^{1}}{\Omega}\right)^2 \approx -\ln N \Rightarrow W_{cr}^{1} \approx \sqrt{\frac{210.4\ln N}{N}}\Omega\,. \tag{4.27}$$

3. ($\mathrm{W}_{\mathrm{cr}}^{1} \leq \mathrm{W} < \mathrm{W}_{\mathrm{cr}}^{2}$) Above the critical disorder $\mathrm{W}_{\mathrm{cr}}^{1}$, the excited states of the system have an hybrid nature constituted by an exponentially localized peak with an extended tail which represent the plateau in the probability distribution of the eigenfunctions. The amplitude of the extended tails increases as the disorder strength W increases, as indicated by the vertical black arrow in Fig. 4.7–(c). Moreover the peak of the shape of the eigenfuctions bem¡comes more and more localized on one site as the disorder increases.

   The third critical disorder can obtained by imposing that the probability on the closest site to the peak, to be equal to the probability in the pateau. Considering that the plateau in the gapped regime decreases as $1/N$ and it is independent of disorder, and considering that the exponential peak on the closest site is given by $\exp(-1/2\xi)$, we can determine $\mathrm{W}_{\mathrm{cr}}^{2}$ by the following equation:

$$\exp\left(-\frac{1}{2\xi}\right) \approx \frac{1}{N} \Rightarrow -\frac{1}{2\xi} \approx -\ln N \tag{4.28}$$

   so that Eq. (4.28) becomes

$$-\frac{1}{210.4}\left(\frac{\mathrm{W}_{\mathrm{cr}}^{2}}{\Omega}\right)^{2} \approx -\ln N \Rightarrow \mathrm{W}_{\mathrm{cr}}^{2} \approx \sqrt{210.4 \ln N}\Omega \tag{4.29}$$

4. ($\mathrm{W}_{\mathrm{cr}}^{2} \leq \mathrm{W} < \mathrm{W}_{\mathrm{cr}}^{\mathrm{H}}$) Above the critical disorder $\mathrm{W}_{\mathrm{cr}}^{2}$, the eigenfunction of the excited states are fully localized on one site with an extended tail which represent the plateau in the probability distribution of the eigenfunctions. The amplitude of the extended tails is independent of the disorders, see Fig. 4.7–(d).

5. ($\mathrm{W} \geq \mathrm{W}_{\mathrm{cr}}^{\mathrm{H}}$) Above the critical disorder $\mathrm{W}_{\mathrm{cr}}^{\mathrm{H}}$, the eigenfunction of the excited states are fully localized on one site with an extended tails which amplitude decreases as the disorder increases, see the vertical black arrow in Fig. 4.7–(e).

We have demonstrated the hybrid nature in the eigenfunctions of the excited states in the gapped regime, similar to the subradiant states in the case of all-to-all non-Hermitian couplings in the Refs. [16]. Moreover, the analysis of the shape of the eigenfunctions indicate a strong correlation with the transport properties of the system. Specifically, we observe that both the integrated transmission T_{int} and the variance $\sigma^2(x)$ are robust to disorder, in the same disorder range where the plateau of the eigenfunctions is independent of the disorder strength W. Thus, we can claim the plateau in the probability distribution of the eigenfunctions supports the robustness of transport properties in the gapped regime.

The analysis of the shape of the eigenfunctions also allowed us to determine the scaling with the parameters of the critical disorders which define the different transport regimes. In order to verify the scaling of the critical disorders, we analyze below the transport properties of the system for difference system sizes N.

In Figs. 4.8 and 4.9 we show the average variance $\langle\sigma^2(x)\rangle$ divided by N^2 and the average integrated transmission $\langle T_{\mathrm{int}}\rangle$ as a function of the disorder strength W for the same parameters (apart from the system size) as in Figs. 4.5 and 4.6. Note that with this scaling we have the same range of normalized variance for different systems size N.

We can observe the scaling of the critical disorders computed above work quite well for all the system sizes N shown. Note that the critical disorder shown in the figures are just an estimate and even if they reproduce correctly the scaling with the system size, some discrepancies are visible mainly for the critical disorder $\mathrm{W}_{\mathrm{cr}}^{\mathrm{H}}$.

Therefore, the presence of an energy gap Δ_{H} in the ground state is able to donate robustness to the excited states of the system and more counterintuitive it is able to induce a disorder regime where the

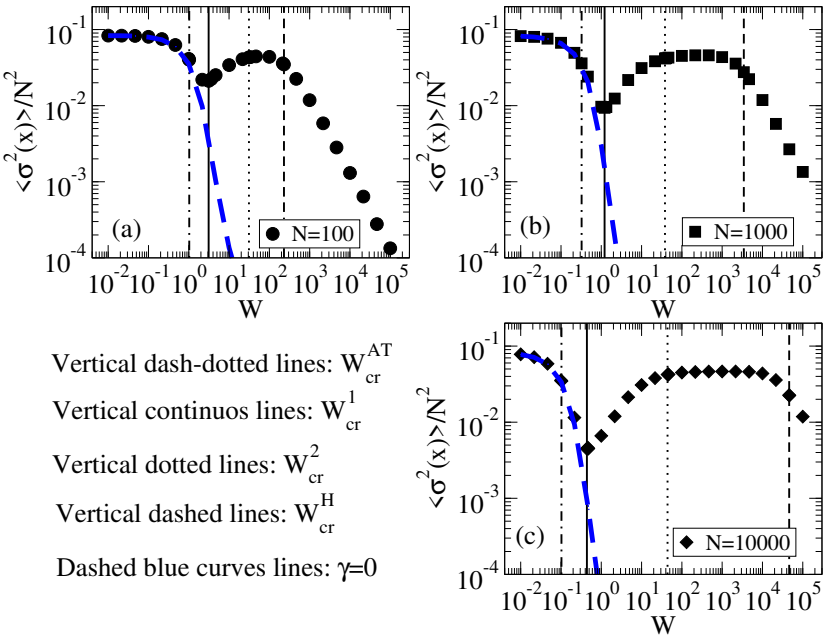

Figure 4.8: Average variance $\langle \sigma^2(x) \rangle$ normalized by N^2 *vs.* the disorder strength W for the coupling strength $\gamma = 1$, the system sizes (a) $N = 100$, (b) $N = 1000$ and (c) $N = 10000$. Here, $\Omega = 1$, $\nu = 0$, $N_r \times N = 10^5$, the vertical lines mark the critical disorder $\mathrm{W}_{\mathrm{cr}}^{\mathrm{AT}}$, $\mathrm{W}_{\mathrm{cr}}^{1}$, $\mathrm{W}_{\mathrm{cr}}^{2}$ or $\mathrm{W}_{\mathrm{cr}}^{\mathrm{H}}$ indicated in the legends for each system size N and the dashed blue curves is the case $\gamma = 0$.

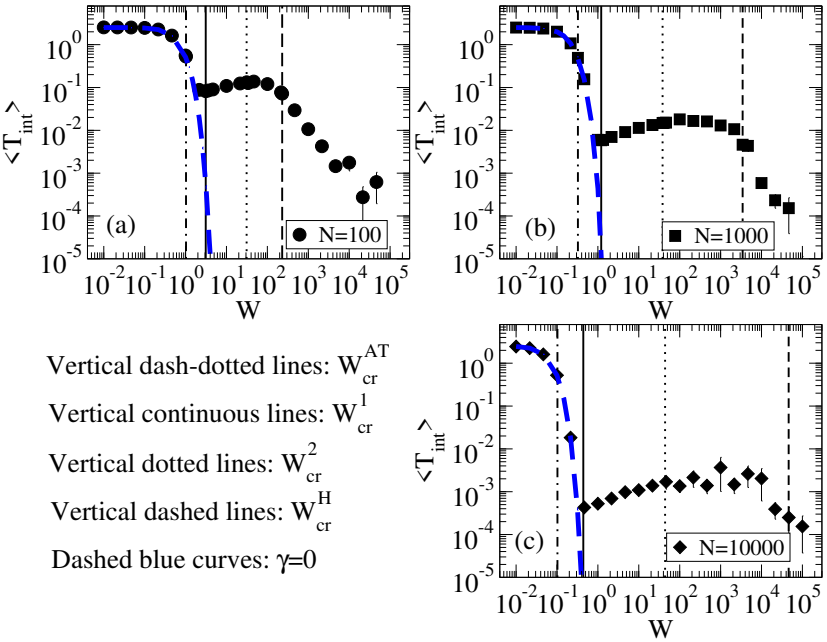

Figure 4.9: Same as in Fig. 4.8 for the average integrated transmission $\langle T_{\mathrm{int}} \rangle$.

integrated transmission T_{int} and the variance $\sigma^2(x)$ increases with disoder or they are independent of disorder.

4.4.3 Perturbation approach

Since we demonstrated that the shape of the eigenfunctions allows to understand the transport properties of the system, here we intend to derive a perturbative expression for the shape of the excited state eigenfunctions in presence of long range all-to-all Hermitian coupling in the gapped regime. For this purpose, we rewrite the Eq. (4.8) in its matricial form as follows

$$H = H_0 - \frac{\gamma}{2}Q + \frac{\gamma}{2}I \tag{4.30}$$

where Q is a full matrix with components 1 and I is the identity matrix. The Q matrix can be easily diagonalized. It has only two different eigenvalues. The first eigenvalue $-\dfrac{\gamma N}{2}$ corresponds to the lowest energy state, which is a fully non degenerated extended state $|d\rangle = \dfrac{1}{\sqrt{N}}(1,\ldots,1)^T$. While the second eigenvalues are zero, corresponds a $N-1$ degenerated subspaces spanned by all the states orthogonal to the lowest energy extended state.

Following [67], we can rewrite the Hamiltonian H in Eq. (4.30) in the basis of these eigenstates, using the transformation matrix V, which has as its columns the eigenstates of the matrix Q:

$$H = V^T H_0 V - \frac{\gamma}{2}V^T Q V + \frac{\gamma}{2}I = \begin{pmatrix} -\dfrac{\gamma}{2}(N-1) & \vec{h}^T \\ \vec{h} & \tilde{H} \end{pmatrix} . \tag{4.31}$$

Let us note that in the component $(1,1)$ of the Eq. (4.31) there should be also the sum over the unperturbed energies of all the sites, $\dfrac{1}{N}\sum_i E_i$ which is zero since the disorder fluctuations are random and uncorrelated. Here, the matrix elements of the $(N-1)\times(N-1)$ submatrix $\tilde{H}$ on the basis of the excited states of the matrix Q are

$$\begin{aligned} \tilde{H}_{\mu\nu} &= \langle\mu|H_0 - \frac{\gamma}{2}Q + \frac{\gamma}{2}I|\nu\rangle \\ &= \langle\mu|H_0|\nu\rangle - \langle\mu|\frac{\gamma}{2}Q|\nu\rangle + \frac{\gamma}{2}\delta_{\mu\nu} , \end{aligned}$$

the second term vanishes since the eigenvalues of the degenerated excited states are 0. If we rewrite the Hamiltonian H_0 in its basis $|n\rangle$, we get

$$\begin{aligned} \tilde{H}_{\mu\nu} &= \langle\mu|\left(\sum_n \epsilon_n |n\rangle\langle n|\right)|\nu\rangle + \frac{\gamma}{2}\delta_{\mu\nu} \\ &= \sum_n \epsilon_n \langle\mu|n\rangle\langle n|\nu\rangle + \frac{\gamma}{2}\delta_{\mu\nu} , \end{aligned} \tag{4.32}$$

where $\delta_{\mu\nu}$ is the Kronecker delta and $|n\rangle$ is an Anderson state with the eigenvalues ϵ_n which are distributed uniformly in the interval $[-\mathrm{W}/2, \mathrm{W}/2]$ for large disorder strength $\mathrm{W} \ll \Omega$. The components of the vector $\vec{h}$, with dimension $N-1$, in the basis of the eigenstates of the matrix Q are

$$h_\mu = \sum_n \epsilon_n \langle d|n\rangle\langle n|\mu\rangle \ . \tag{4.33}$$

Now, we diagonalize the submatrix $\tilde{H}$ and we call $|\mu\rangle$ its eigenstates with eigenvalues $\tilde{\epsilon}_\mu$, i.e.

$$\tilde{H}_{\mu\nu} = \tilde{\epsilon}_\mu \delta_{\mu\nu} \tag{4.34}$$

Note that the $|\mu\rangle$ eigenstates of $\tilde{H}$ are also eigenstates of Q since they belong to the $N-1$ degenerated subspace of the Q matrix.

If we multiply Eq. (4.32) by the components $\langle m|\mu'\rangle$ where $|\mu'\rangle$ is an eigenstate of the submatrix $\tilde{H}$ and $|m\rangle$ is an Anderson state, and then we sum over all the states μ', we obtain

$$\begin{aligned}
\sum_{\mu'} \tilde{H}_{\mu'\mu} \langle m|\alpha\rangle &= \sum_{\mu'}\sum_{n} \epsilon_n \langle \mu'|n\rangle \langle n|\mu\rangle \langle m|\mu'\rangle + \frac{\gamma}{2}\sum_{\mu'} \delta_{\mu'\mu} \langle m|\mu'\rangle \\
&= \sum_{n} \epsilon_n \langle n|\mu\rangle \langle m| \left(\sum_{\mu'} |\mu'\rangle \langle \mu'|\right) |n\rangle + \frac{\gamma}{2} \langle m|\mu\rangle \\
&= \sum_{n} \epsilon_n \langle n|\mu\rangle \langle m| \left(I - |d\rangle \langle d|\right) |n\rangle + \frac{\gamma}{2} \langle m|\mu\rangle \\
&= \sum_{n} \epsilon_n \langle n|\mu\rangle \left(\delta_{mn} - \langle m|d\rangle \langle d|n\rangle\right) + \frac{\gamma}{2} \langle m|\mu\rangle \\
&= (\epsilon_m + \frac{\gamma}{2}) \langle m|\mu\rangle - \sum_{n} \epsilon_n \langle d|n\rangle \langle n|\mu\rangle \langle m|d\rangle \\
&= (\epsilon_m + \frac{\gamma}{2}) \langle m|\mu\rangle - h_\mu \langle m|d\rangle \ .
\end{aligned} \tag{4.35}$$

On the other hand from Eq. (4.32), we get

$$\sum_{\mu'} \tilde{H}_{\mu'\mu} \langle m|\mu'\rangle = \sum_{\mu'} \tilde{\epsilon}_{\mu'} \delta_{\mu'\mu} \langle m|\mu'\rangle = \tilde{\epsilon}_\mu \langle m|\mu\rangle \ . \tag{4.36}$$

Comparing the Eqs. (4.35) and (4.36), we obtain

$$\tilde{\epsilon}_\mu \langle m|\mu\rangle = (\epsilon_m + \frac{\gamma}{2}) \langle m|\mu\rangle - h_\mu \langle m|d\rangle \ , \tag{4.37}$$

i.e.

$$|\mu\rangle = \frac{h_\mu}{H_0 + \gamma/2 - \tilde{\epsilon}_\mu} |d\rangle \ . \tag{4.38}$$

The Eq. (4.38) can be rewritten in the Anderson basis as follows

$$|\mu\rangle = h_\mu \sum_n \frac{\langle n|d\rangle}{\epsilon_n + \gamma/2 - \tilde{\epsilon}_\mu} |n\rangle = \frac{h_\mu}{\sqrt{N}} \sum_n \frac{\sum_j \langle n|j\rangle}{\epsilon_n + \gamma/2 - \tilde{\epsilon}_\mu} |n\rangle \tag{4.39}$$

where $|j\rangle$ is the site basis and the normalization coefficients h_μ are given by

$$h_\mu = \left(\sum_n \frac{\langle d|n\rangle \langle n|d\rangle}{(\epsilon_n + \gamma/2 - \tilde{\epsilon}_\mu)^2}\right)^{-1/2} \ . \tag{4.40}$$

In the gapped regime and for sufficiently large disorder $\mathrm{W}_{\mathrm{cr}}^2 < \mathrm{W} < \mathrm{W}_{\mathrm{cr}}^{\mathrm{H}}$ where the eigenstates have hybrid nature, we can assume that the Anderson eigenstates coincide with the site basis, see the

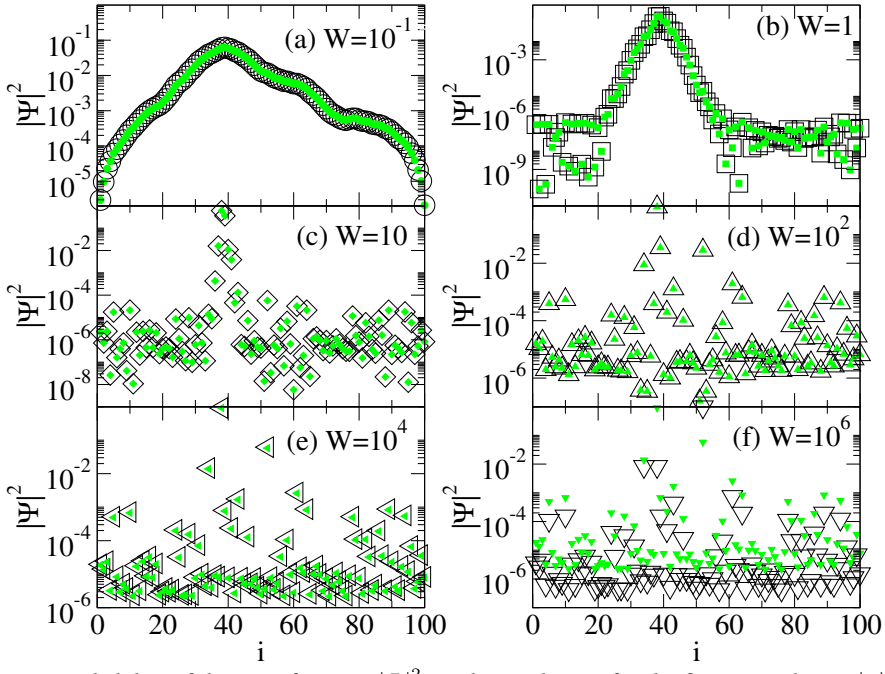

Figure 4.10: Probability of the eigenfunction $|\Psi|^2$ *vs.* the site basis i for the first excited state $|\mu\rangle$ and the disorders strength $\mathrm{W} = \{10^{-1}, 1, 10, 10^2, 10^4, 10^6\}$. Here, $N = 100$, $\gamma = 10^3$, $N_r = 1$, the black symbols indicate the probability of the eigenfunction of the total Hamiltonian H in Eq. (4.8) and the green symbols mark the probability of the eigenfunction obtained by the Eq. (4.39). Note that ST occurs at $\mathrm{W}_{\mathrm{cr}}^{\mathrm{H}} \sim 230258.5$ so we cannot expect agreement in panel (f).

Fig. 4.7–(d). So, the Eq. (4.39) with the normalization coefficients h_μ in Eq. (4.40) becomes

$$\begin{aligned} |\mu\rangle &\approx \left(\frac{1}{N}\sum_i \frac{1}{(\epsilon_i + \gamma/2 - \tilde{\epsilon}_\mu)^2}\right)^{-1/2} \frac{1}{\sqrt{N}}\sum_i \frac{1}{\epsilon_i + \gamma/2 - \tilde{\epsilon}_\mu}\,|i\rangle \\ &\approx \left(\sum_i \frac{1}{\left(\frac{(\epsilon_i - \tilde{\epsilon}_\mu)}{\mathrm{W}} + \frac{\gamma}{2\mathrm{W}}\right)^2}\right)^{-1/2} \sum_i \frac{1}{\frac{(\epsilon_i - \tilde{\epsilon}_\mu)}{\mathrm{W}} + \frac{\gamma}{2\mathrm{W}}}\,|i\rangle \end{aligned} \tag{4.41}$$

Our perturbative expression, although it does allow to compute the eigenstates analytically, it allows to explain many features of the shape of the eigenfunctions discussed above. Mainly the existance of a disorder independent plateau in the disorder range $\mathrm{W}_{\mathrm{cr}}^2 < \mathrm{W} < \mathrm{W}_{\mathrm{cr}}^{\mathrm{H}}$, as we discuss below. From Eq. (4.41) we can see that both the normalization coefficients and the weights on the site basis are independent of disorder for $\mathrm{W} \gg \gamma$ since both ϵ_i and $\tilde{\epsilon}_\mu$ are proportional to the disorder strength W for large disorder. This is an important results since our perturbative approach is able to explain the independence of the plateau from disorder in the disorder regime $\mathrm{W}_{\mathrm{cr}}^2 < \mathrm{W} < \mathrm{W}_{\mathrm{cr}}^{\mathrm{H}}$. Since the disorder strength W is uncorrelated from the sites, this also shows that we have a distant independent tail in the eigenfunctions of the system. Moreover, since $\frac{(\epsilon_i - \tilde{\epsilon}_\mu)}{\mathrm{W}}$ decreases as $1/N$, this also explains the dependence of the probability of the plateau on the system size for $\mathrm{W} \gg \gamma$.

4.4.3.1 Shape of the eigenfunction for the first excited state

Note that, even if we obtained a closed expression for the $|\mu\rangle$ states in Eq. (4.39), to compute them we still need to relay on numerical approaches. Indeed, we obtain the $|\mu\rangle$ states in the following way:

1. We diagonalize the Anderson model without the all-to-all Hermitian coupling to obtain the Anderson basis $|n\rangle$ and the eigenvalues ϵ_n.
2. We use the transformation matrix V, which has as its columns the eigenstates of the matrix Q in Eq. (4.30) to obtain the submatrix $\tilde{H}$.
3. We diagonalize $\tilde{H}$ to obtain the eigenvalues $\tilde{\epsilon}_\mu$ ordering them by energy.
4. From the knowledge of ϵ_n and $\tilde{\epsilon}_\mu$ and the eigenstates of the Anderson model $|n\rangle$ we can use Eq (4.39) to obtain the perturbative expression of the eigenstates $|\mu\rangle$.

Here we compare the perturbative eigenstates computed as described above, with the eigenstates of the total Hamiltonian in Eq. (4.8) computed by numerical diagonalization. For this purpose, in Fig. 4.10, we show the probability $|\Psi|^2$ for the first excited state as a function of the site basis i obtained by diagonalize the total Hamiltonian H in Eq. (4.8), see black symbols. Also, we show the corresponded probability $|\Psi|^2$ obtained by the perturbative approach using Eq. (4.39), see green symbols. The parameters for the results were: the disorders strength $\mathrm{W} = \{10^{-1}, 1, 10, 10^2, 10^4, 10^6\}$, the coupling strength $\gamma = 10^3$ and the system size $N = 100$.

Our perturbative approach works very well in all panels of Fig. 4.10, except in the panel (f) where the perturbation approach is not valid since the disorder $\mathrm{W} = 10^6$ is above the critical disorder $\mathrm{W}_{\mathrm{cr}}^{\mathrm{H}}$ and we are in the non-gapped regime.

4.4.3.2 Variance of the position operator on single eigenstates

In the previous section, we obtained the probability $|\Psi|^2$ of the first excited state, but we can use the Eq. (4.39) to compute the probability $|\Psi|^2$ for all the excited states in the gapped regime. From the knowledge of these eigenstates, we can calculate T_{int} and $\sigma^2(x)$.

In this section, we compute the variance $\sigma^2(x)$ with three different methods:

1. We diagonalize the total Hamitonian H in Eq. (4.8) and we compute the average variance $\sigma^2(x)$ over all the eigenstates $|\alpha\rangle$ of H.
2. We average the variance over all the states using the perturbative eigenstates $|\mu\rangle$ in Eq. (4.39) for the excited states, and using the expression $|d\rangle = \frac{1}{\sqrt{N}}(1, \ldots, 1)^T$ for the ground state,
3. We considered an excitation localized on a single site in the middle of the chain and we simulate the dynamical evolution of the system numerically. The spread the initial localized excitation will reach a stationary distribution, from which we compute the variance of the position operator.

In Fig. 4.11 we show the average variance $\langle\sigma^2(x)\rangle$ as a function of the disorder strength W for the system sizes $N = 100$ and the coupling strength $\gamma = 10^3$. We compare the variance $\sigma^2(x)$ obtained by diagonalize the total Hamiltonian H in Eq. (4.8) indicated with circles, by the perturbative approach in Eq. (4.39) indicated with squares and by the dynamical evolution, see dashed curves.

The results obtained by the perturbative approach are in good agreement with those obtained by diagonalizing the total Hamiltonian H for all disorder strengths below the critical disorder $\mathrm{W}_{\mathrm{cr}}^{\mathrm{H}}$. Above of this critical disorder, the perturbative approach is not valid and the results do not coincide with each other. On the other hand, the variance of the stationary distribution obtained dynamically is in fair agreement with the average variance over all the eigenstates in the whole disorder range considered.

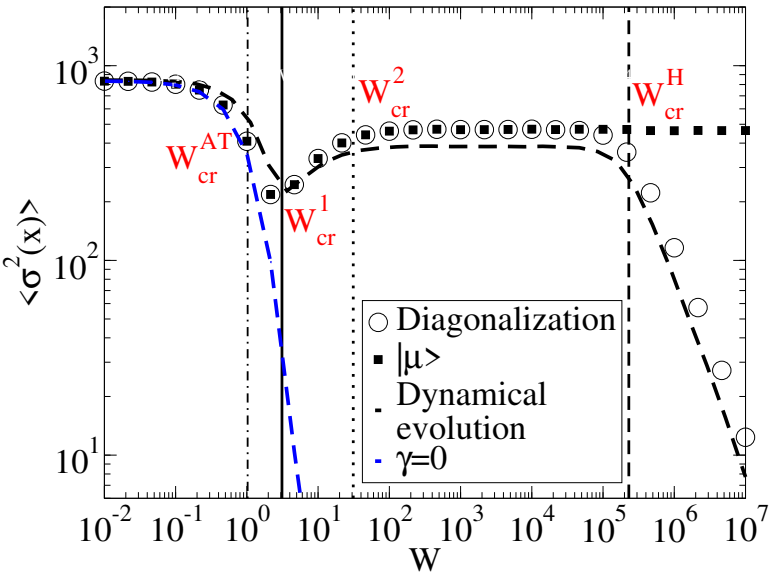

Figure 4.11: Average variance $\sigma^2(x)$ *vs.* the disorder strength W for the coupling strength $\gamma = 10^3$ and the system size $N = 100$. Here, $N_r \times N = 10^5$ where N_r is number of disorder configurations, the circles indicate the variance $\sigma^2(x)$ obtained by diagonalize the total Hamiltonian H in Eq. (4.8), the squares are obtained by the perturbative approach in Eq. (4.39) and the dashed curves are the variance of the stationary distribution obtained by dynamical evolution of a localized excitation. The vertical lines mark the critical disorders strength W^{AT}_{cr}, W^1_{cr}, W^2_{cr} or W^H_{cr}, see the description in section 4.4.2. The dashed blue curve shows the results for the Anderson model without long range hopping, $\gamma = 0$.

4.4.3.3 Integrated transmission for excited states

In this section we compare the integrated transmission $T_{\rm int}$ obtained with Eq. (4.22) from numerical diagonalization and with the integrated transmission obtained with Eq. (4.22) using the perturbative eigenstates $|\mu\rangle$ Eq. (4.39).

In Fig. 4.12 we show the average integrated transmission $\langle T_{\rm int}\rangle$ as a function of the disorder strength W for the system size $N = 100$, the coupling strength $\gamma = 10^3$ and the coupling strength to the leads $\nu = 1$.

In order to obtain the integrated transmission from the knowledge of the perturbative eigenstates $|\mu\rangle$ and $|d\rangle$, let us note that the decay widths Γ_μ of each state $|\mu\rangle$ can be obtained from the following expression:

$$\Gamma_\mu \approx \nu(|\Psi^1_\mu|^2 + |\Psi^N_\mu|^2)\,,$$

i.e., the decay widths Γ_μ of the state $|\mu\rangle$ are proportional to the coupling strength ν to the leads at the edges of the chain times the probability of the eigenfunction of the state $|\mu\rangle$ at the edges of the system.

From Fig. 4.12, we can observe that $\langle T_{\rm int}\rangle$ obtained by the two methods are quite similar in the gapped regime. In the non-gapped regime strong differences are easily explained by the fact that our perturbative approach is not valid there.

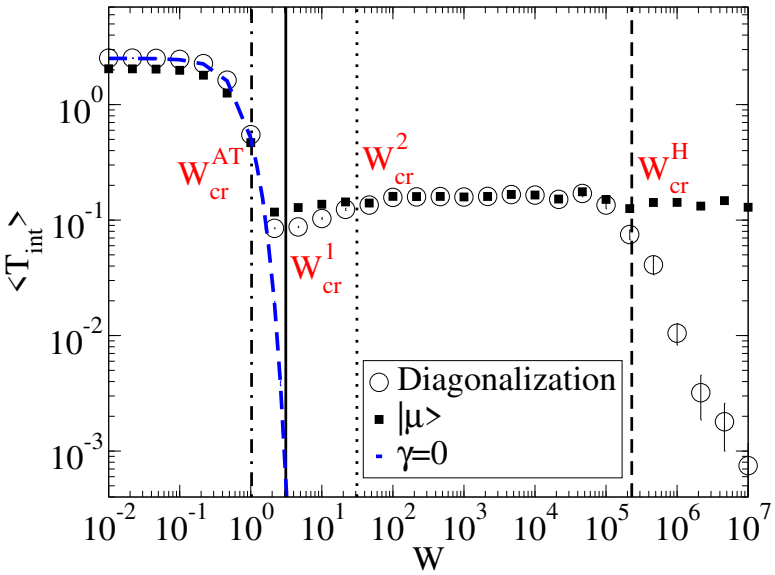

Figure 4.12: Average integrated transmission $T_{\rm int}$ *vs.* the disorder strength W for the $N = 100$, $\gamma = 10^3$ and $\nu = 1$. Here, $N_r \times N = 10^5$ where N_r is number of disorder configurations, the circles indicate the results obtained by the analytical Eq. (4.22) and the squares indicate the results obtained by Eq. (4.39) for all the excited states $|\mu\rangle$. The vertical lines mark the critical disorders strength $\mathrm{W}_{\rm cr}^{\rm AT}$, $\mathrm{W}_{\rm cr}^{1}$, $\mathrm{W}_{\rm cr}^{2}$ or $\mathrm{W}_{\rm cr}^{\rm H}$, see the description in section 4.4.2. The dashed blue curve shows the results for the Anderson model without long range hopping, $\gamma = 0$.

4.5 Non-Hermitian case

For the non-Hermitian coupling $V_0 = i\gamma/2$, the components of the effective non-Hermitian Hamiltonian are

$$(H_{\rm eff})_{k,l} = (H_0)_{k,l} - i\frac{\gamma}{2} - \frac{i}{2}\nu(\delta_{k,1}\delta_{l,1} + \delta_{k,N}\delta_{l,N})\,, \tag{4.42}$$

where H_0 is the Hamiltonian in the Anderson model in Eq. (4.1), the second term is the all-to-all non-Hermitian coupling with coupling strength γ and the third term is the coupling to the leads at the edges of the chain with coupling strength ν.

As we did in section 4.4, let us show the effect of non-Hermitian coupling on the integrated transmission $T_{\rm int}$ and on the variance $\sigma^2(x)$ for all the eigenstates for the same parameters as Figs. 4.5 and 4.6.

4.5.1 Integrated transmission and the variance of the eigenstates

Here we analyze the transport properties of the non-Hermitian long range system as a function of disorder strength W. We will compare the transport properties (integrated transmission $T_{\rm int}$ and variance $\sigma^2(x)$ of the all eigenstates) with the transport properties of the Anderson model in absence of the all-to-all coupling strength γ.

We show that in presence of long range hopping, the emergence of an energy gap Δ_{NH} in the superradiant state is able to change the transmission properties in the system below the critical disorder $\mathrm{W}_{\mathrm{cr}}^{\mathrm{NH}} = \gamma N\pi/2$, correponding to the gapped/superradiant regime. Moreover we will show the emergence of different transport regime in different disorder ranges.

4.5.1.1 Variance of the eigenstates

In Fig. 4.13 we show the average variance $\langle\sigma^2(x)\rangle$ as a function of the disorder strength W for the same parameters as Fig. 4.5. The numerical results were obtained using Eq. (4.23).

The behavior of the average variance for the non-Hermitian all-to-all coupling is almost identical to the behavior for the variance in the Hermitian case, see Fig. 4.5. Indeed also in this case we have 5 different transport regimes and the critical disorders in the two cases are same apart from the critical disorder which determines a transition to a non-gapped regime $\mathrm{W}_{\mathrm{cr}}^{\mathrm{H}}$, which differes from the critical disorder which determines a transition to superradiance $\mathrm{W}_{\mathrm{cr}}^{\mathrm{NH}}$.

4.5.1.2 Integrated transmission

In Fig. 4.14 we show the average integrated transmission $\langle T_{\mathrm{int}}\rangle$ as a function of the disorder strength W for the same parameters as Fig. 4.6. The numerical results were obtained using Eq. (4.22).

The integrated transmission T_{int} shows a similar behavior like the Anderson model in absence of the long range coupling below the critical disorder $\mathrm{W} < \mathrm{W}_{\mathrm{cr}}^{1}$ in the gapped regime, see the dashed

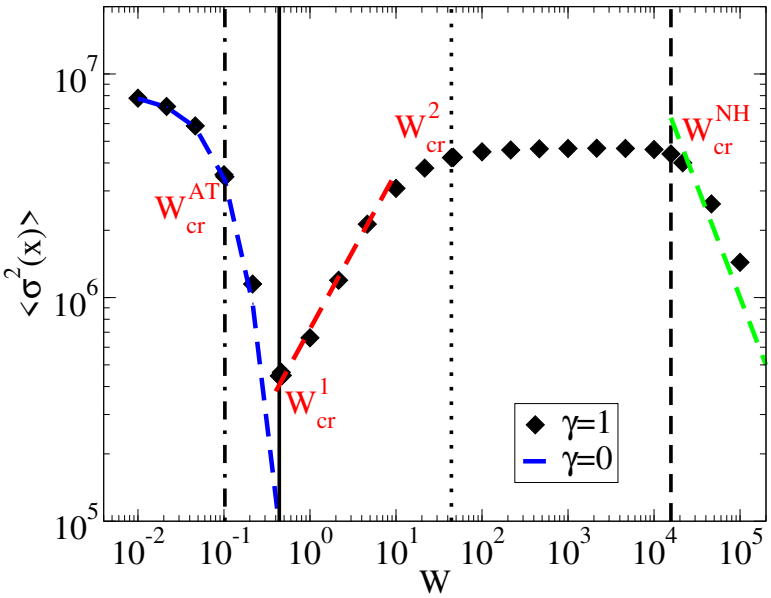

Figure 4.13: Average variance $\langle\sigma^2(x)\rangle$ *vs.* the disorder strength W for the coupling strength $\gamma = 1$ and the system size $N = 10000$ for all the states. Here, $\Omega = 1$, $\nu = 0$, $N_r \times N = 10^5$ where N_r is the number of disorder configurations. The vertical lines mark the critical disorders strength $\mathrm{W}_{\mathrm{cr}}^{\mathrm{AT}}$, $\mathrm{W}_{\mathrm{cr}}^{1}$, $\mathrm{W}_{\mathrm{cr}}^{2}$ or $\mathrm{W}_{\mathrm{cr}}^{\mathrm{H}}$, see the description in section 4.4.2. The dashed blue curve shows the results for the Anderson model without long range hopping, $\gamma = 0$. The dashed red line goes like $\mathrm{W}^{0.7}$ and the dashed green line goes like W^{-1}.

blue curve in Fig. 4.14.

Also for non-Hermitian all-to-all coupling, after the critical value W^1_{cr} the integrated transmission T_{int} increases with W as $W^{0.6}$. Nevertheless, contrary to the Hermitian case, the integrated transmission reaches a maximum and then decreases well below the superradiant transition. This effect is due to the losses present in the system. Indeed an excitation can be lost before reaching the exit lead and this implies a reduction of the integrated transmission due to the fact that as we increase disorder W we also increase the losses from the subradiant states [50].

The existence of the losses in the system implies that there is no disorder regime where the integrated transmission T_{int} is independent to the disorder strength W as we observed in the all-to-all Hermitian coupling, see Fig. 4.6.

Now, as we did in section 4.4, let us check the effect of the non-Hermitian coupling on the shape of the eigenfunctions for fixed coupling strength γ and system size N on different disorder regimes without coupling to the leads, i.e. $\nu = 0$ in Eq. (4.42). This analysis has been already performed in some parameter reagion in Refs. [16].

4.5.2 Shape of the eigenfunctions

In Fig. 4.15 we show the average shape of the eigenfunctions $\langle|\Psi|^2\rangle$ as a function of the site basis k for the coupling strength $\gamma = 1$ and the system size $N = 100$. We use the same procedure to obtain the average shape of the eigenfunctions as we did in the Hermitian coupling, see section 4.4.2 .

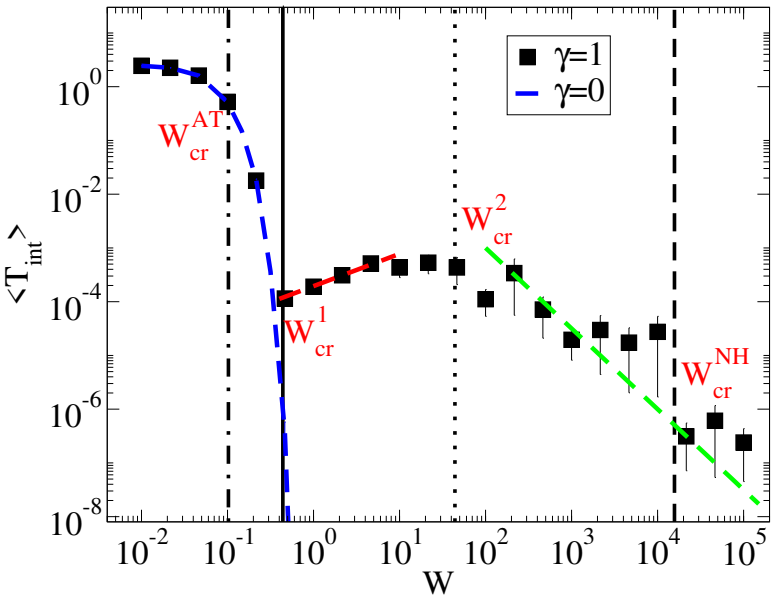

Figure 4.14: Average integrated transmission $\langle T_{int}\rangle$ *vs.* the disorder strength W for the coupling strength $\gamma = 1$ and the system size $N = 10000$ for all the states. Here, $\Omega = \nu = 1$, $N_r \times N = 5 \times 10^5$ where N_r is the number of disorder configurations. The vertical lines mark the critical disorders strength W^{AT}_{cr}, W^{1}_{cr}, W^{2}_{cr} or W^{H}_{cr}, see the description in section 4.4.2. The dashed blue curve shows the results for the Anderson model without long range hopping, $\gamma = 0$. The dashed red line goes like $W^{0.6}$ and the dashed green line goes like $W^{-1.5}$.

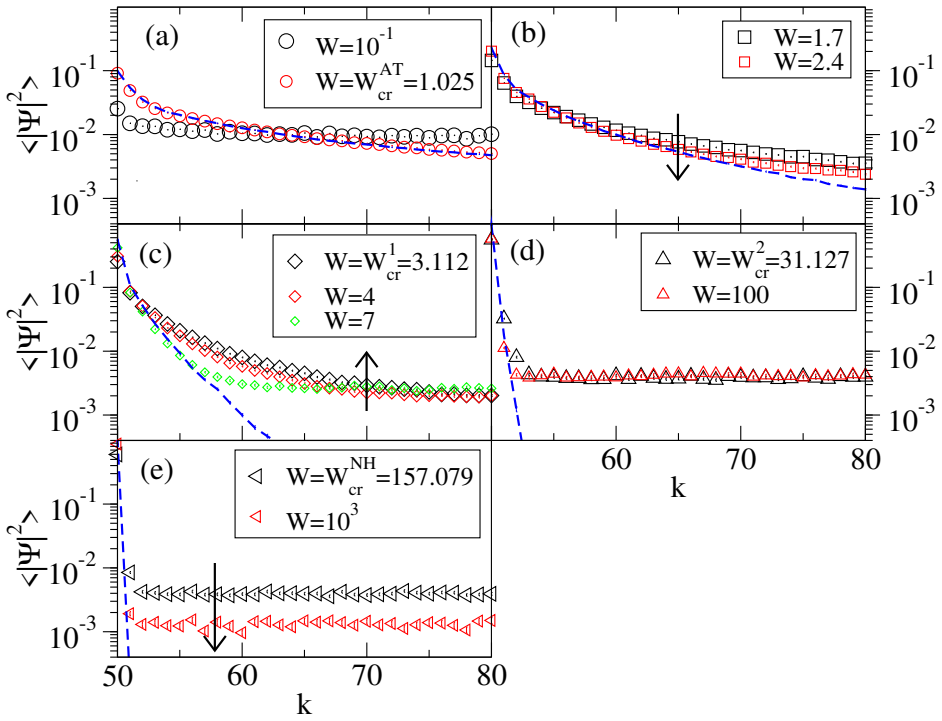

Figure 4.15: Average shape of the eigenfunctions $\langle|\Psi|^2\rangle$ *vs.* the site basis k. In each panel, different disorder regimes are shown: (a) $W \leq W_{cr}^{AT}$, (b) $W_{cr}^{AT} < W < W_{cr}^{1}$, (c) $W_{cr}^{1} \leq W < W_{cr}^{2}$, (d) $W_{cr}^{2} \leq W < W_{cr}^{H}$ and (e) $W > W_{cr}^{H}$. Here, $N = 100$, $\Omega = \gamma = 1$, the number of disorder configurations is $N_r = 1000$. The dashed blue curves indicate the shape of eigenfunctions for $\gamma = 0$.

We can observe that the shapes of the eigenfunctions in Fig. 4.15 are quite similar to the Hermitian coupling case in Fig. 4.7. Note that our results are consistent with the results in Refs. [16]. Note also that the critical disorders have been computed as in section 4.4.2.

In order to verify the scaling of the critical disorders computed above with the system size N, we analyze below the transport properties of the system for difference system sizes N.

So, in Figs. 4.16 and 4.17 we show the average variance $\langle\sigma^2(x)\rangle$ divided by N^2 and the average integrated transmission $\langle T_{\rm int}\rangle$ as a function of the disorder strength W for the same parameters as in Figs. 4.13 and 4.14.

We can observe the critical disorders strengths work quite well for all the system sizes N shown here for the variance $\sigma^2(x)$. On the other hand, only the critical disorders W_{cr}^{AT} and W_{cr}^{1} work well for the integrated transmission $T_{\rm int}$, since, as we discussed above, losses produce a different behavior for the non-Hermitian case.

Nevertheless, more work is needed in the future to understand the effect of losses and to determine the local maximum of the integrated transmission as a function of disorder strength W.

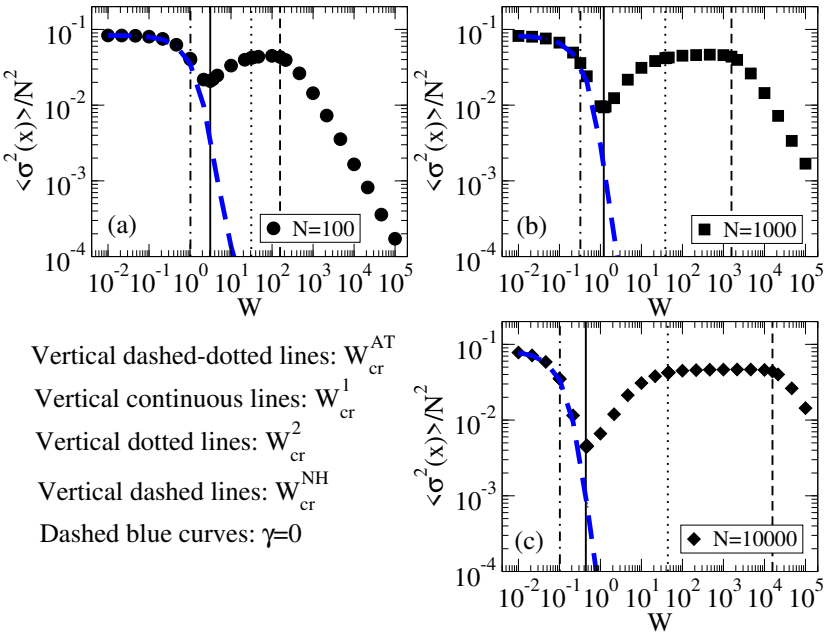

Figure 4.16: Average variance $\langle \sigma^2(x) \rangle$ normalized by N^2 *vs.* the disorder strength W for the coupling strength $\gamma = 1$, the system sizes (a) $N = 100$, (b) $N = 1000$ and (c) $N = 10000$. Here, $\Omega = 1$, $\nu = 0$, $N_r \times N = 10^5$, the vertical lines mark the critical disorder $\mathrm{W}_{\mathrm{cr}}^{\mathrm{AT}}$, $\mathrm{W}_{\mathrm{cr}}^{1}$, $\mathrm{W}_{\mathrm{cr}}^{2}$ or $\mathrm{W}_{\mathrm{cr}}^{\mathrm{NH}}$ indicated in the legends and the dashed blue curves is the case $\gamma = 0$.

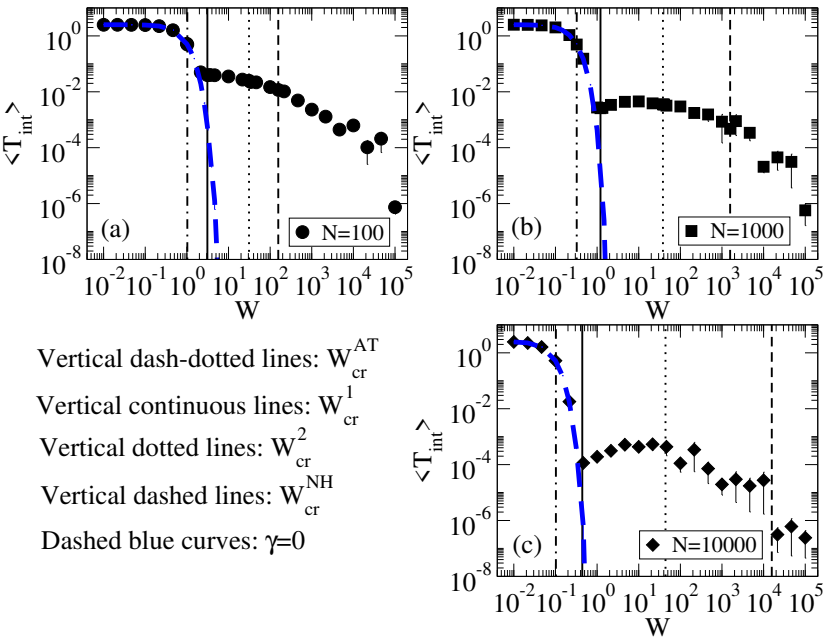

Figure 4.17: Same as in Fig. 4.16 for the average integrated transmission $\langle T_{\mathrm{int}} \rangle$.

4.6 Conclusions of Chapter 4

We demonstrated that the energy gap that arises in the Picket-Fence model, studied in Chapter 3, also emerges in the Anderson model with Hermitian and non-Hermitian long-range hoppings. Indeed, the same formulas for the energy gaps in the Picket-Fence model are valid for the Anderson model in the large disorder limit.

The effect of the emergence of energy gaps on the transport properties of the system was studied by analyzing two transport properties: the average integrated transmision and the average variance over all the eigenstates.

We derived an analytical expression for the integrated transmission which depends on the amplitudes of the eigenfunctions at the edges of the chain, the complex eigenvalues of the effective Hamiltonian, and the coupling strength to the leads. This expression allowed us to evaluate the integrated transmission exactly without relying on numerical integration of the transmission. The integrated transmission represents the overall transmission over a wide spectral energy band.We used this formula to study the transmission properties in the Anderson model with Hermitian and non-Hermitian couplings as the disorder crosses from the gapped regime to the non-gapped regime.

We also analyzed the average variance over all the eigenstates. We have shown that, in our case, this quantity gives a very good approximation to the variance of the stationary distribution obtained by the dynamical evolution of an initial localized excitation in the middle of the chain.

For the Hermitian coupling, the presence of an energy gap in the ground state is able to provide robustness to the disorder to the excited states of the system as we observed the integrated tranmission and the variance over all the eigenstates. More counter-intuitively, the gapped ground state is also able to create a disorder independent transport regime. The transport properties can be explained by analyzing the shape of the eigenfunctions of the system, which, in the gapped regime and in presence of disorder, show an hybrid nature. We obtained an analytical expression for the eigenstates of the system in the gapped regime by means of a perturbative approach, which is able to explain the above mentioned counter-intuitive behavior of the transport properties of the system.

For the non-Hermitian coupling, the presence of an energy gap in the superradiant state is able to change the transmission properties in the system and it is able to improve transport efficiency up to a critical disorder where it reaches a maximum peak connected with the presence of the losses in the system. In the future, we plan to understand better the role of losses in the case of a coupling to an unbounded external environment.

Chapter 5

Conclusions

In this thesis we have studied the effects of coupling a quantum system to external unbounded and bounded environments. Such couplings are able to induce long-range hoppings between the system components. The effect of such couplings on the transport properties of paradigmatic models of quantum transport, such as the Power-law Banded Random Matrix (PBRM) model and the 1D Anderson model, has been analyzed. Two different kinds of long-range hoppings were considered: an all-to-all Hermitian hopping (induced by the coupling to a bounded environment) and an all-to-all non-Hermitian hopping (induced by the coupling to an unbounded environment). Both kinds of couplings can be realized experimentally in ion-traps [5], in photosynthetic antenna complexes [61], or molecular chains in optical cavities [1].

Our general conclusion is that the presence of long-range hopping terms drastically changes the transport properties of a quantum system. Specifically, below we list the most interesting results discussed in this thesis.

In Chapter 2, we considered the PBRM model in presence of a coupling to an external environment. The PBRM model can be considered a paradigmatic model for one-dimensional quantum systems in presence of random long-range hopping terms. One of the most interesting features of this model is the presence of a localization transition characterized by the multifractal nature of the eigenstates. Moreover, at the localization transition the degree of multifractality can be controlled by a parameter that represents the spacial range of the random hopping. The most interesting result obtained here was for the case where the sites of PBRM model are coupled to a common decay channel. This coupling is able to induce a superradiant transition in the model. At the superradiant transition the multifractality of the eigenstates strongly depends on their life time. Thus, the introduction of this coupling adds a whole new parameter axis which is able to control the multifractality of the eigenstates.

In Chapter 3, we compared two paradigmatic models for Superconductivity and Superradiance, focusing on the emergence of an energy gap in the real and complex plane, respectively. We showed that a gap arises also in the Superradiance model and it is equal to the Superconductivity gap in the large coupling regime. We also showed that the usual superradiance transition can be interpreted as a transition to a gapped regime. The energy gap in the complex plane can induce robustness to perturbations in the system, similarly to a gap in the real axis.

The results obtained in the Chapter 3 were included in the article “Real and imaginary energy gaps: a comparison between single excitation Superradiance and Superconductivity and robustness to disorder”, Nahum C. Chávez, F. Mattioti, J.A. Méndez-Bermúdez, F. Borgonovi and G.L. Celardo, Eur. Phys, J. B **92**, 144 (2019).

For the Anderson model studied in Chapter 4, the presence of Hermitian and non-Hermitian all-to-all coupling induces a rich phase diagram in the transport properties of the system controlled by

the strength of disorder. Moreover, it is able to induce very counter-intuitive effects in the transport properties. Specifically, while below a critical disorder strength the transport properties of the system are the same as those of the 1D Anderson model without long-range hoppings, above a critical disorder the transmission efficiency increases with the disorder instead of decreasing exponentially as in the 1D Anderson model. Furthermore, for large disorder strength, the system enters a regime where transport is independent of disorder. Both features can be captured by the shape of the eigenfuctions of the system which we were able to determine analytically using a perturbative approach.

In perspective, our results open the path to a better control of the transport properties of quantum systems that interact with external environments. In the literature there are several works dedicated to scattering properties of the PBRM model [30, 33, 68]. Nevertheless, no study has been done on the multifractal structure of the eigenstates by modulating the decay widths of the system. It would be extremely interesting to verify experimentally the dependence of multifractality on the decay widths of a system. Since the decay widths of a state represents its life time, our results could open the possibility of different transport regimes arising in time.

As far as our results about the 1D Anderson model are concerned, one of the most interesting future research directions is the analysis of the interplay of an unbounded or bounded external environment with a decoherent environment (dynamical noise, inelastic scattering, etc.). The introduction of time dependent noise will be essential to prove, at least theoretically, the possibility of dissipative-less transport. Also, it would be interesting to study the interplay of many body correlations with the coupling to unbounded and bounded external environments.

Clearly, an experimental verification of our results would be very interesting. Indeed, the disorder-independent transport regime we found could be tested in several real systems: in ion trap experiments where all-to-all hopping can be engineered, in molecular aggregates with strong superradiance [69], in perovskites superlattices [70], or in molecular chains in optical cavities [1].

Appendix A

Widths of the subradiant states

In the Chapter 2, we reported the analytic expression of the widths of all the eigenstates for $\gamma < \gamma_{\rm SR}$ (3.27) and of the widths of the subradiant states for $\gamma > \gamma_{\rm SR}$ (3.28). Here we derive those expressions, as well as the critical coupling strength $\gamma_{\rm SR}$, following [13].

Let us consider the case of odd N, so that we can write $N = 2M+1$ with M an integer. Note that the limit $N \to \infty$ corresponds to $M \to \infty$ and in that limit there is no distinction between even or odd values of N. The Hamiltonian (3.1), with E_k given by (3.2) and $V_0 = i\gamma/(2N)$, can be mapped to

$$H = \delta\overline{H} = \delta\left(\sum_{k=-M}^{M} k\,|k\rangle\langle k| - i\alpha\sum_{k=-M}^{M}\sum_{k'=-M}^{M}|k\rangle\langle k'|\right), \tag{A.1}$$

where the center of the unperturbed spectrum is assumed to be at $E_0 = 0$, without loss of generality, and the coupling parameter is

$$\alpha = \frac{\gamma}{2N\delta} = \frac{\gamma}{2S}. \tag{A.2}$$

We now proceed to compute the eigenvalues $\overline{\lambda}$ of $\overline{H}$, which are related to the eigenvalues λ of H by $\lambda = \delta\overline{\lambda}$. Thus, let us consider the matrix $\langle k|\,\overline{H}\,|k'\rangle$. By construction, all column and row vectors, respectively, of the non-Hermitian part of that matrix are linearly dependent. Summing $i\alpha$ times the central row ($k = 0$) to all the other rows ($k \neq 0$), one gets the following expression for the characteristic polynomial:

$$P_M(\overline{\lambda}) = \prod_{k=-M}^{M}(k-\overline{\lambda}) - i\alpha\sum_{k=-M}^{M}\prod_{\substack{j=-M\\ j\neq k}}^{M}(j-\overline{\lambda}) = 0. \tag{A.3}$$

According to Eq. (A.3), $P_M(\overline{\lambda})$ is the sum of two polynomials,

$$P_M(\overline{\lambda}) = Q_M(\overline{\lambda}) - i\alpha R_M(\overline{\lambda}) \tag{A.4}$$

which are related in a simple manner,

$$R_M = -\frac{d}{d\overline{\lambda}}Q_M.$$

Taking the limit $M \to \infty$ and using the infinite product expansion of the sine function we have

$$P_\infty(\overline{\lambda}) = \sin[\pi\overline{\lambda}] + i\alpha\pi\cos[\pi\overline{\lambda}] = 0 \tag{A.5}$$

with $\overline{\lambda} = \overline{E} - \frac{i}{2}\overline{\Gamma}$. Then, we can substitute this expression of $\overline{\lambda}$ to get

$$P_\infty(\overline{\lambda}) = \sin\left[\pi\left(\overline{E} - \frac{i}{2}\overline{\Gamma}\right)\right] + i\alpha\pi\cos\left[\pi\left(\overline{E} - \frac{i}{2}\overline{\Gamma}\right)\right] = 0\,. \tag{A.6}$$

Separating real and imaginary parts one has

$$\begin{cases} \sin[\pi\overline{E}]\left[e^{\pi\overline{\Gamma}}(1-\alpha\pi) + (1+\alpha\pi)\right] = 0 \\ \cos[\pi\overline{E}]\left[e^{\pi\overline{\Gamma}}(1-\alpha\pi) - (1+\alpha\pi)\right] = 0 \end{cases}. \tag{A.7}$$

So there are two solutions:
i) $\sin[\pi\overline{E}] = 0$, $\overline{E} = n \in \mathbb{Z}$

$$e^{\pi\overline{\Gamma}} = \frac{1+\alpha\pi}{1-\alpha\pi}\,, \tag{A.8}$$

from which

$$\overline{\Gamma} = \frac{1}{\pi}\ln\left(\frac{1+\alpha\pi}{1-\alpha\pi}\right) \tag{A.9}$$

under the conditions $e^{\pi\overline{\Gamma}} > 0$, $\alpha < \frac{1}{\pi}$. This result represents the widths of all the eigenstates below the Superradiance transition.
ii) $\cos[\pi\overline{E}] = 0$, $\overline{E} = n + \frac{1}{2}, n \in \mathbb{Z}$

$$e^{\pi\overline{\Gamma}} = \frac{\alpha\pi+1}{\alpha\pi-1}\,, \tag{A.10}$$

which gives

$$\overline{\Gamma}_{\text{sub}} = \frac{1}{\pi}\ln\left(\frac{\alpha\pi+1}{\alpha\pi-1}\right) \tag{A.11}$$

under the conditions $e^{\pi\overline{\Gamma}} > 0$, $\alpha > \frac{1}{\pi}$. This result represents instead the widths of the subradiant states above the Superradiance transition. From these results a critical coupling parameter $\alpha_{\text{SR}} = 1/\pi$ emerges, which marks the Superradiance transition.

Now, let us map our expression for $\overline{\lambda}$ to $\lambda = E - \frac{i}{2}\Gamma$. Multiplying by δ we have

$$E_n = n\delta \qquad (n \in \mathbb{Z}) \tag{A.12a}$$

$$\Gamma = \frac{\delta}{\pi}\ln\left(\frac{1+\alpha/\alpha_{\text{SR}}}{1-\alpha/\alpha_{\text{SR}}}\right) \qquad \text{for } \alpha < \alpha_{\text{SR}} \tag{A.12b}$$

and

$$E_n = \left(n + \frac{1}{2}\right)\delta \qquad (n \in \mathbb{Z}) \tag{A.13a}$$

$$\Gamma_{\text{sub}} = \frac{\delta}{\pi}\ln\left(\frac{\alpha/\alpha_{\text{SR}}+1}{\alpha/\alpha_{\text{SR}}-1}\right) \qquad \text{for } \alpha > \alpha_{\text{SR}}\,, \tag{A.13b}$$

where we can use (A.2) to express the ratio between α and α_{SR} as

$$\frac{\alpha}{\alpha_{\text{SR}}} = \frac{\gamma\pi}{2S}\,. \tag{A.14}$$

Thus, equations (A.12b) and (A.13b) can be rewritten in terms of the parameters of H as

$$\Gamma = \frac{S}{N\pi}\ln\left(\frac{1+\gamma/\gamma_{\text{SR}}}{1-\gamma/\gamma_{\text{SR}}}\right) \qquad \text{for } \gamma < \gamma_{\text{SR}} \tag{A.15}$$

and

$$\Gamma_{\rm sub} = \frac{S}{N\pi} \ln\left(\frac{\gamma/\gamma_{\rm SR}+1}{\gamma/\gamma_{\rm SR}-1}\right) \qquad \text{for } \gamma > \gamma_{\rm SR}\,, \tag{A.16}$$

by defining the critical coupling

$$\gamma_{\rm SR} = \frac{2S}{\pi}\,. \tag{A.17}$$

A.1 Long and short-range interaction

In the Chapter 2, we reported how the energy gap $\Delta_{\rm H}$ changes with the range of the interaction for $\alpha = \{1/3, 1, 5\}$. Here, in Fig. A.1, we show the dependence of $\Delta_{\rm H}$ on γ for some additional values of the range of interaction, namely for $\alpha = \{1/10, 1/2, 3/2, 2\}$. We would like to point out also that the definition (3.36) is equal to $E_2 - E_1$ in the range of γ that we plotted in this figure and in the Chapter 2 (Fig. 3.6).

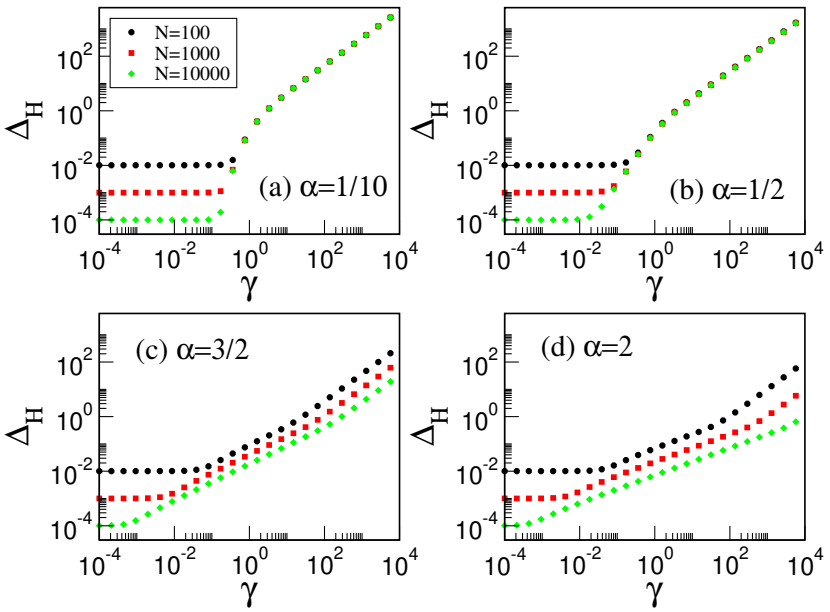

Figure A.1: a) Gap $\Delta_{\rm H}$, as given by Eq. (3.36), *vs.* the coupling strength γ with the interaction (3.47) for different values of the interaction range α. Here we set $\mathrm{W} = 1$.

As we reported in the Sec. 3.4, in order to obtain the gap $\Delta_{\rm H}$ for different range of interaction α, the interaction (3.47) is normalized by the constant $v_{N,\alpha}$ defined as the difference between the maximum eigenenergy and minimal eigenenergy of the matrix V given by the expression

$$V' = -\sum_{\substack{k,k'\\ k\neq k'}} \frac{|k\rangle\langle k'|}{|k-k'|^{\alpha}}\,, \tag{A.18}$$

i.e. $v_{N,\alpha} = V'_{max} - V'_{min}$. In Fig. A.2 we plot $v_{N,\alpha}$ *vs.* N for different values of α and we show that the exact results obtained from the diagonalization of V' (symbols) fit well the scaling (3.48) for all the values of α shown here.

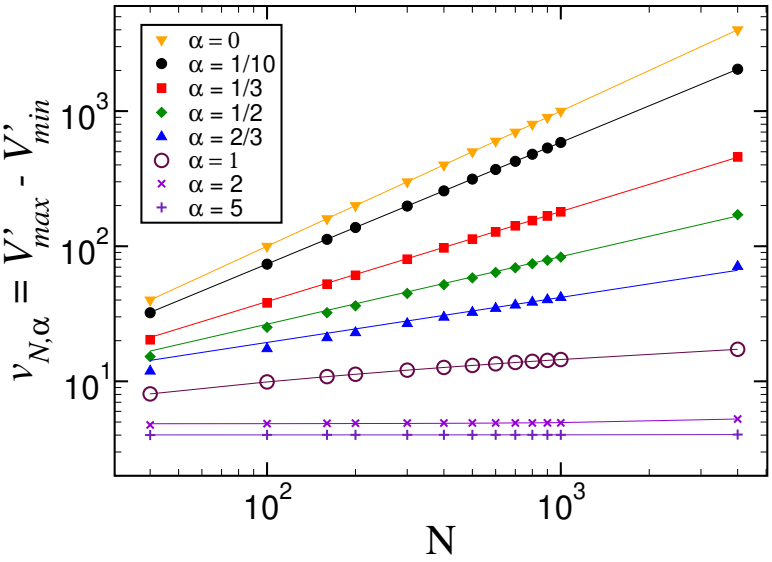

Figure A.2: The energy range of the interaction $v_{N,\alpha}$ *vs.* the system size N for different $\alpha = \{0, 1/10, 1/3, 1/2, 2/3, 1, 2, 5\}$. Symbols are obtained by diagonalizing V (3.47) without the prefactor $\gamma/(2v_{N,\alpha})$, while lines are the best fits with the functions (3.48).

Appendix B

Resonance transmission in the ground state

For the Hermitian coupling, above the critical coupling strength $\gamma_{\rm cr}^{\rm H} = 2{\rm W}/(N \ln N)$, the energy gap $\Delta_{\rm H}$ donates robustness to the disorder to the ground state.

In this large coupling regime, the ground state is fully extended and the resonance of the transmission $T_{E_1}(E)$ for the ground state has the analytical expression

$$T_{E_1}(E) = \frac{(\nu/N)^2}{(E - E_1)^2 + (\nu/N)^2} \tag{B.1}$$

where E_1 is the ground state energy, N is the system size and ν is the coupling strength to the leads at the edge of the system.

In Fig. B.1 we show the transmission $T_{E_1}(E)$ as a function of the energy E around the ground state energy E_1 with only one disorder configuration ($N_r = 1$) for the coupling strength $\gamma = 10^3$, the system sizes $N = \{100, 1000\}$ and the disorders strength ${\rm W} = \{10, 100\}$ comparing them with Eq. (B.1).

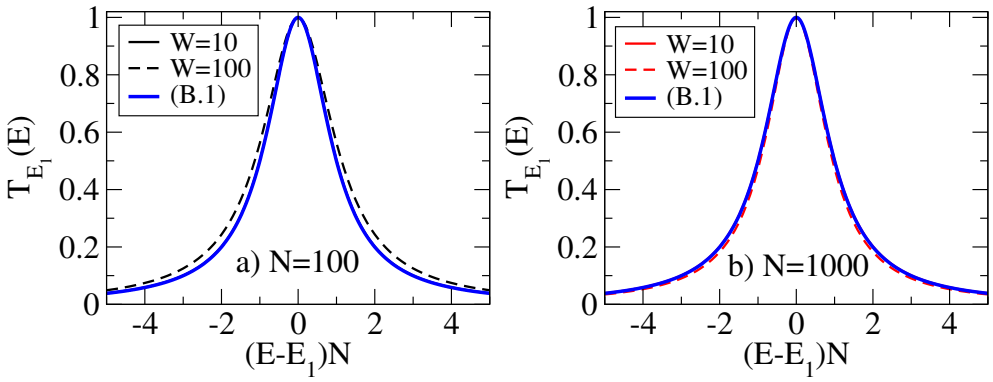

Figure B.1: Transmission $T_{E_1}(E)$ *vs.* the energy $(E - E_1)N$ obtained by the Eq. (C.3) and by the Eq. (B.1) for the system size (a) $N = 100$ and (b) $N = 1000$. Here, $\gamma = 10^3$, $\Omega = \nu = 1$, ${\rm W} = \{10, 100\}$ for one disorder configuration.

We normalized the energy axis by N in order to observe the complete resonance of the transmission because the decay width $\Gamma \approx 2\nu/N$. The blue curves mark the analytical profile of the resonances in Eq. (B.1).

From Eq. (B.1), we observe that transmission for the ground state remains perfect, i.e. $T_{E_1}(E_1) = 1$ for all the values of N and W shown.

Let us note that the value of the ground state energy E_1 changes from random configuration to another but the transmission remains perfect for each realization as we can observe in Fig. B.2 where the case $N = 100$, $\gamma = 10$ and $\mathrm{W} = 10$ is shown.

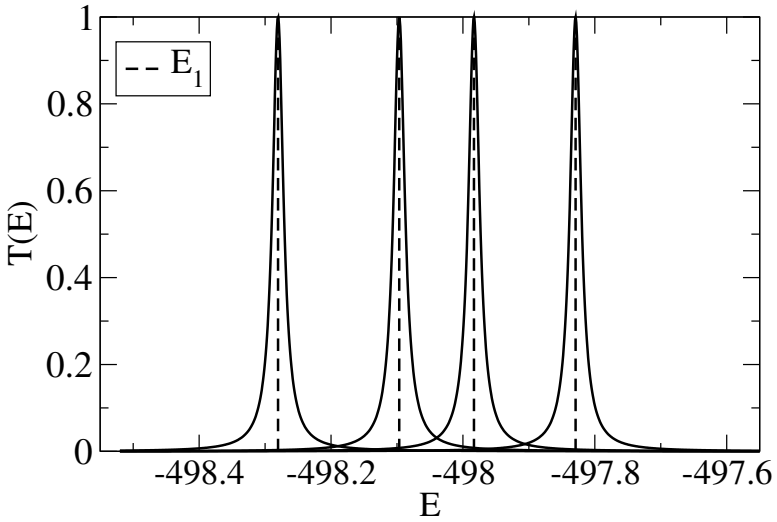

Figure B.2: Transmission $T(E)$ *vs.* the energy E for the ground state energy E_1 with $N = 100$, $\mathrm{W} = 10$ and coupling strength $\gamma = 10$ for four disorder configurations. The vertical dashed black lines indicate the ground state energy E_1 in each disorder configuration.

Appendix C

Integrated transmission: comparison of different numerical methods

In the Chapter 4, we derived the analytical Eq. (4.22) for the integrated transmission $T_{\rm int}$. This equation is valid for the both Hermitian and non-Hermitian coupling. Here, we compare the numerical results obtained by the Eq. (4.22) and by a direct numerical integration of the integrated transmission, obtained applying the composite Simpson's rule.

C.1 Composite Simpson's rule

Suppose that the interval $[a, b]$ is split up into n sub-intervals with n an even number. Then, the composite Simpson's rule is given by

$$\int_a^b f(x)dx \approx \frac{h}{3}\left[f(x_0) + 2\sum_{j=1}^{n/2-1} f(x_{2j}) + 4\sum_{j=1}^{n/2} f(x_{2j-1}) + f(x_n)\right], \tag{C.1}$$

where $x_j = a + jh$ for $j = 0, 1, \ldots, n-1, n$ with $h = (b-a)/n$, $x_0 = a$ and $x_n = b$.

For our simulations: $x_0 = -\mathrm{W} - N\gamma/2$, $x_n = \mathrm{W}$ and we used the length of the bin $h = \Delta E = 10^{-5}$.

C.2 K-matrix method

To obtain a direct numerical evaluation of the integrated transmission, we compute the transmission $T(E)$ as a function of the energy E using the K-matrix method defined as

$$K^{a,b}(E) = \sum_n \frac{A_n^a A_n^b}{E - E_n}, \tag{C.2}$$

where E_n are the eigenvalues of the Hamiltonian in the Anderson model and the elements $A_n^{a,b}$ are the decay amplitudes from the states n to the continuum channels a or b. The transmission amplitude

from channel a to channel b is

$$Z^{a,b}(E) = \left(\frac{K(E)}{1 + \frac{i}{2}K(E)} \right)_{a,b} , \tag{C.3}$$

and the transmission is $T^{a,b}(E) = |Z^{a,b}(E)|^2$.

So that, in the Fig. C.1 we show the integrated transmission $T_{\rm int}$, for both Hermitian and non-Hermitian coupling, for the disorder configurations $N_r = 100$. We use the set of parameters: $N = 100$, $\mathrm{W} = 10$ and the couplings strength $\gamma = 10^2 \gamma_{\rm cr}^{\rm H,NH}$ with $\gamma_{\rm cr}^{\rm H} = 2\mathrm{W}/(N \ln N)$ for Hermitian coupling or $\gamma_{\rm cr}^{\rm NH} = 2\mathrm{W}/(N\pi)$ for non-Hermitian coupling. The black circles were obtained with the numerical integration method in Eq. (C.1) and the red circles with Eq. (4.22). We indicated the averages integrated transmission obtained by the two method in the legends.

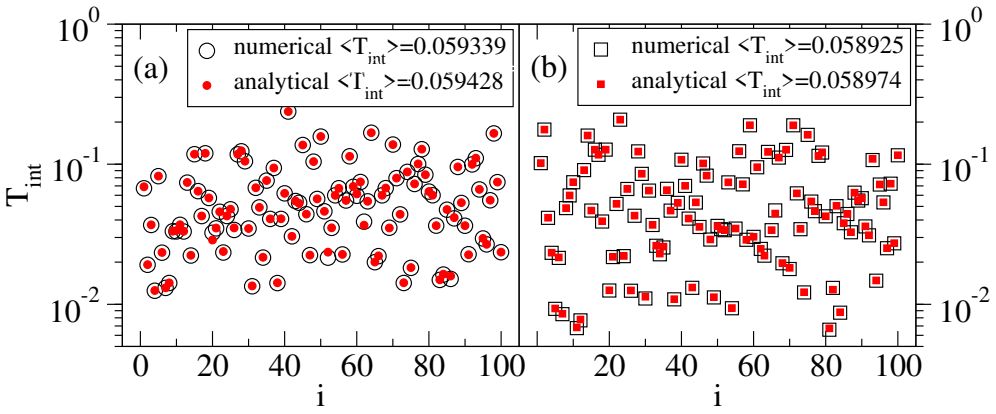

Figure C.1: Integrated transmission $T_{\rm int}$ *vs.* the realization i for disorder $\mathrm{W} = 10$, $N = 100$, $\Omega = \nu = 1$, $\Delta E = 10^{-5}$ and the couplings strength $\gamma/\gamma_{\rm cr}^{\rm H,NH} = 10^2$ comparing the integrated transmission obtained by the composite Simpson's rule in Eq. (C.1) and the Eq. (4.22) for the Hermitian coupling in panel (a) and for the non-Hermitian coupling in panel (b). The average integrated transmission $\langle T_{\rm int} \rangle$ obtained by two methods are indicated in the legends.

From Fig. C.1 we can observe that the numerical results of the integrated transmission obtained by the Eq. (4.22) and by the numerical integration method in Eq. (C.1) are quite similar in all the random realizations.

Meanwhile in Fig. C.2 we show the average integrated transmission $\langle T_{\rm int} \rangle$ as a function of the coupling $\gamma/\gamma_{\rm cr}^{\rm H,NH}$ obtained by the two methods for the same parameters as in Fig. C.1. As you can see, we have a good results for Hermitian and non-Hermitian couplings in all different coupling regimes.

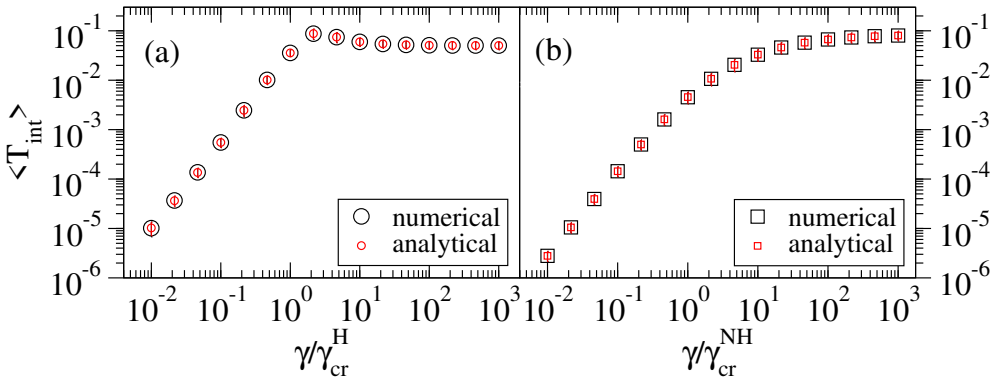

Figure C.2: Average integrated transmission $\langle T_{\rm int} \rangle$ *vs.* the coupling strength $\gamma/\gamma_{\rm cr}^{\rm H,NH}$ for disorder $\mathrm{W} = 10$, $N_r = 100$, $N = 100$ comparing the integrated transmission obtained by the composite Simpson's rule in Eq. (C.1) and the Eq. (4.22) for the Hermitian coupling panel (a) and for the non-Hermitian coupling in panel (b).

Here we verified that we can use the analytical equation of the integrated transmission $T_{\rm int}$ in substitution of a direct numerical integration. Direct numerical integration implies longer computational time and more computational resources.

Appendix D

The dependence of the integrated transmission on system size N and coupling strength γ

In the Chapter 4, we showed the dependence of the integrated transmission T_{int} on disorder for both the Hermitian and non-Hermitian coupling. Here, we will analyze the dependence of T_{int} on the system size N and the coupling strength γ.

For the Hermitian coupling, we will exclude the contribution of the ground state to the integrated transmission T_{int}, while for the non-Hermitian coupling, we have considered the contribution of all the states to the integrated transmission T_{int}.

First, we will analyze the dependence of the system size N and then the dependence of the coupling strength γ for the Hermitian case and then for the non-Hermitian case. Note that for the non-Hermitian case, more work is needed to have a complete picture.

D.1 Hermitian case

D.1.1 Ground state: dependence on system size N

In Fig. D.1 we show the average integrated transmission $\langle T_{\text{int}} \rangle$ as a function of the system size N for the ground state obtained by Eq. (4.22).

From Fig. D.1, we can observe that for large couplings strength $\gamma/\gamma_{\text{cr}}^{\text{H}} \gg 1$, the average integrated transmission $\langle T_{\text{int}} \rangle$ for the ground state is given by the following expression:

$$\langle T_{\text{int}} \rangle \approx \frac{\pi}{N} \tag{D.1}$$

where $\gamma_{\text{cr}}^{\text{H}} = 2\text{W}/(N \ln N)$ for Hermitian coupling. This expression shows that $\langle T_{\text{int}} \rangle$ is independent of disorder strength W in the gapped regime and it depends only on the system size N.

Let us note, we can derive the Eq. (D.1) from the analytical Eq. (4.22) for the integrated transmission T_{int}. To show this, let us consider the ground state eigenfunction components Ψ_g^i with the complex

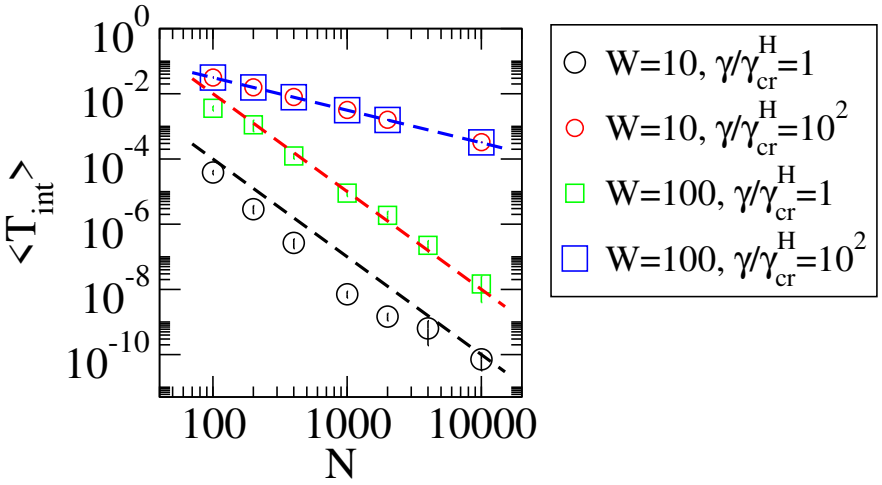

Figure D.1: Average integrated transmission $\langle T_{\rm int}\rangle$ *vs.* the system size N for the ground state, the normalized couplings strength $\gamma/\gamma_{\rm cr}^{\rm H} = \{1, 100\}$ and the disorders strength $\mathrm{W} = \{10, 100\}$. Here, $\Omega = \nu = 1$, the number of disorder configurations N_r is such that $N_r \times N = 10^5$. The dashed black and red lines are W^2/N^3 and the dashed blue line indicates the Eq. (D.1).

energy $\mathcal{E}_g = E_g - \frac{i}{2}\Gamma_g$. It is easy to prove that the decay widths can be written as $\Gamma_g \approx \nu(|\Psi_g^1|^2 + |\Psi_g^N|^2)$, i.e., the decay width Γ_g is approximately the coupling strength ν to the leads times the probability to be at the edges of the chain for each eigenstate. Thus, for the ground state, Eq. (4.22) becomes

$$T_{\rm int} \approx 2\pi\nu^2 \frac{|\Psi_g^1|^2|\Psi_g^N|^2}{\nu(|\Psi_g^1|^2 + |\Psi_g^N|^2)}\,. \tag{D.2}$$

In the gapped regime for large coupling, the ground state is an extended state, i.e. $\Psi_g^i \approx 1/\sqrt{N}$, and we get

$$T_{\rm int} \approx 2\pi\nu \frac{(1/N)(1/N)}{(1/N)+(1/N)} \approx \frac{\pi\nu}{N}\,. \tag{D.3}$$

From Eq. (D.3) we get Eq. (D.1) for $\nu = 1$.

From Fig. D.1, we can observe that for $\gamma = \gamma_{\rm cr}^{\rm H}$, $\langle T_{\rm int}\rangle = \mathrm{W}^2/N^3$, see the dashed black and red lines in Fig. D.1.

We did not show the results for small couplings since for this coupling regime, the ground state is not gapped and it is expected to behave as the other excited states which will be discussed in the next section.

D.1.2 Excited states

D.1.2.1 Dependence on system size N

In Fig. D.2 we show the average integrated transmission $\langle T_{\rm int}\rangle$ as a function of the system size N for the disorder strengths $\mathrm{W} = \{10, 100\}$ and the coupling strengths $\gamma/\gamma_{\rm cr}^{\rm H} = \{10^{-2}, 1, 10^2\}$ for all the states except for the ground state.

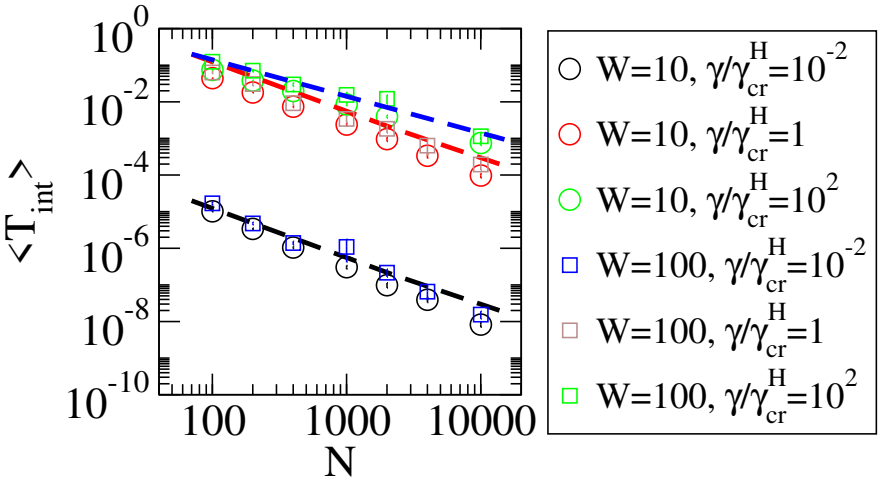

Figure D.2: Average integrated transmission $\langle T_{\rm int}\rangle$ *vs.* the system size N for the normalized couplings strength $\gamma/\gamma^{\rm H}_{\rm cr} = \{10^{-2}, 1, 10^2\}$ and disorders strength $\mathrm{W} = \{10, 100\}$. Here, $\Omega = \nu = 1$, the number of disorder configurations N_r is such that $N_r \times N = 10^5$. The dashed black and red lines indicate the Eq. (D.4). While the dashed blue line indicates the Eq. (D.5).

From Fig. D.2, we can observe that the decay of the average integrated transmission $\langle T_{\rm int}\rangle$ with the system size N, depends on the normalized coupling strength $\gamma/\gamma^{\rm H}_{\rm cr}$ as follows

$$\langle T_{\rm int}\rangle \approx \frac{60\pi}{N(\ln N)^2}\left(\frac{\gamma}{\gamma^{\rm H}_{\rm cr}}\right)^2 , \tag{D.4}$$

see the dashed black and red lines in Fig. D.2. While at large coupling strength $\gamma/\gamma^{\rm H}_{\rm cr} = 10^2$,

$$\langle T_{\rm int}\rangle \approx \frac{9\pi}{2N} , \tag{D.5}$$

indicated by the dashed blue line in Fig. D.2 for the all disorders W shown.

In the following section, we will obtain an analytical estimate of the dependence of $\langle T_{\rm int}\rangle$ on the system size N under the assumption that resonances do not overlap.

D.1.2.2 Estimation of the dependence of the integrated transmission $T_{\rm int}$ on the system size.

It is possible to obtain the dependence of $T_{\rm int}$ on the system size N using the assumption of non overlapping resonance. This assumption requires the decay widths of the eigenstates $\Gamma_k \approx \nu(|\Psi^1_k|^2 + |\Psi^N_k|^2)$ to be smaller than the mean level spacing. Under this assumption, we can neglect interference effects between different resonance and the double sum in Eq. (4.22) becomes a sum over the contributions of all the single resonances:

$$T_{\rm int} \approx 2\pi\nu^2 \sum_k \frac{|\Psi^1_k|^2|\Psi^N_k|^2}{\Gamma_k} \approx 2\pi\nu \sum_k \frac{|\Psi^1_k|^2|\Psi^N_k|^2}{(|\Psi^1_k|^2 + |\Psi^N_k|^2)} . \tag{D.6}$$

In Fig. D.3 we show $\langle T_{\rm int}\rangle$ as a function of the disorder strength W for $N = \{100, 1000\}$ comparing the $T_{\rm int}$ obtained by Eq. (4.22) and by Eq. (D.6).

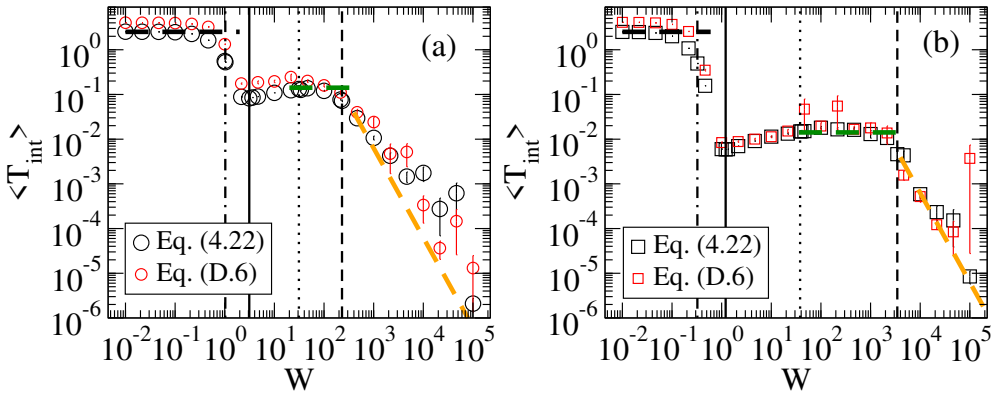

Figure D.3: Average integrated transmission $\langle T_{\rm int}\rangle$ *vs.* the disorder strength W for the system size (a) $N = 100$ and (b) $N = 1000$ comparing the Eqs. (4.22) and (D.6). Here, $\Omega = \nu = 1$, $\gamma = 1$, the number of disorder configurations N_r is such that $N_r \times N = 10^5$. The vertical lines mark the critical disorders strength $\mathrm{W}_{\rm cr}^{\rm AT}$, $\mathrm{W}_{\rm cr}^{1}$, $\mathrm{W}_{\rm cr}^{2}$ or $\mathrm{W}_{\rm cr}^{\rm H}$, see the description in section 4.4.2. The black lines mark the Eq. (D.7), the green lines mark the Eq. (D.9) and the dashed orange lines mark the Eq. (D.10).

We can observe that the numerical results obtained by Eq. (D.6) capture the general behavior of $\langle T_{\rm int}\rangle$ given by the exact results obtained from Eq. (4.22).

Using Eq. (D.6) we can estimate the dependence of $\langle T_{\rm int}\rangle$ on the systems parameters in different disorder regimes as follows:

1. Disorder regime below finite size Anderson transition critical disorder $\mathrm{W}_{\rm cr}^{\rm AT}$. The eigenfunctions are extended, so that the probability to be at the edges of the chain is proportional to N^{-1}, i.e., $|\Psi_k^i|^2 \approx 1/N$. Thus, Eq. (D.6) becomes

$$T_{\rm int} \approx \pi\nu \sum_k \frac{4}{5N} \approx \frac{4\pi\nu}{5} \tag{D.7}$$

   In this regime, $T_{\rm int}$ is independent of N and disorder, see black lines in Fig. D.3.

2. In the disorder regime $\mathrm{W}_{\rm cr}^{2} < \mathrm{W} < \mathrm{W}_{\rm cr}^{\rm H}$, for the majority of the eigenfunctions, the probability to be at the edges of the chain is approximately the same, i.e., $|\Psi_k^1|^2 \approx |\Psi_k^N|^2 \approx |\Psi_k^{\rm edge}|^2$ and Eq. (D.6) becomes

$$T_{\rm int} \approx \pi\nu \sum_k |\Psi_k^{\rm edge}|^2 \,. \tag{D.8}$$

   It is important to determine how the eigenfunctions probability $|\Psi_k^{\rm edge}|^2$ depends on the system size. Since the decay width Γ depends on the eigenfunctions probability at the edges, we can analyze Γ for all the states.

   So, in Fig. D.4–(a) we show the distribution of the logarithm of the decay widths $P(\ln(\Gamma N^2))$ with disorder strength $\mathrm{W} = 10^2$. We use the same system parameters as in Fig. D.3

   We can observe that the decay widths Γ depend on the system size as N^{-2}. This implies that for the typical value of the eigenfunction probability at the edges we have: $|\Psi_k^{\rm edge}|^2 \approx 9/(2N^2)$. Thus, Eq. (D.8) becomes

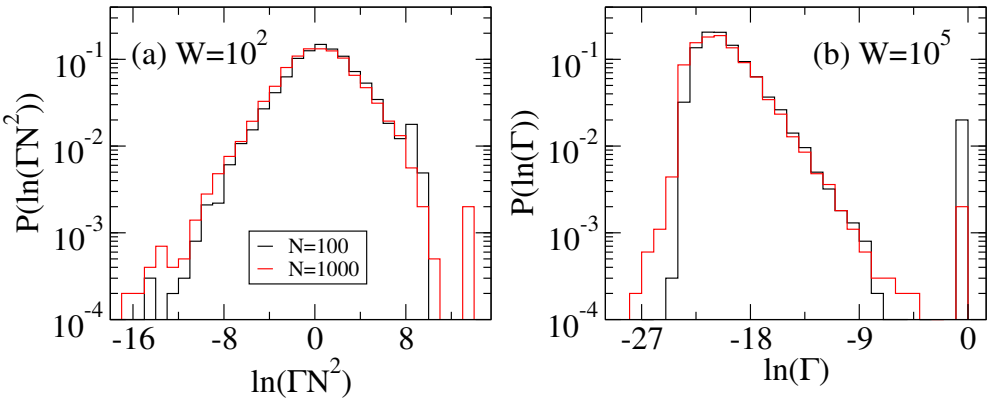

Figure D.4: (a) Distribution of the logarithm of the decay widths $P(\ln(\Gamma N^2))$ for the disorder strength $\mathrm{W} = 10^2$ and (b) distribution of the logarithm of the decay widths $P(\ln(\Gamma))$ for the disorder strength $\mathrm{W} = 10^5$. Here, $N = \{100, 1000\}$, $\Omega = \nu = 1$, $\gamma = 1$, the number of disorder configurations N_r is such that $N_r \times N = 10^5$.

$$T_{\mathrm{int}} \approx \pi\nu \sum_k \frac{9}{2N^2} \approx \frac{9\pi\nu}{2N}\,, \tag{D.9}$$

i.e., T_{int} is independent of the disorder, see blue lines in Fig. D.3. The Eq. (D.9) is in agreement with Eq. (D.5).

3. Above the critical disorder $\mathrm{W}_{\mathrm{cr}}^{\mathrm{H}}$, from Fig. D.4–(b) we observe that the distribution of the logarithm of the decay widths $P(\ln(\Gamma))$ is independent of the system size N for the disorder strength $\mathrm{W} = 10^5$, i.e., the decay widths Γ are independent of the system size N. This result is in agreement with Ref. [16] in which the authors reported that the eigenfunctions probability is independent of N and it goes like $(\gamma/\mathrm{W})^2$. So, Eq. (D.6) becomes

$$T_{\mathrm{int}} \approx 15\pi\nu \sum_k \left(\frac{\gamma}{\mathrm{W}}\right)^2 \approx 15\pi\nu N \left(\frac{\gamma}{\mathrm{W}}\right)^2\,, \tag{D.10}$$

i.e., the integrated transmission T_{int} depends on the parameters set (γ, N, W) for large disorder regime or small coupling strength, see orange lines in Fig. D.3.

Recalling that $\gamma_{\mathrm{cr}}^{\mathrm{H}} = 2\mathrm{W}/(N\ln N)$, the Eq. (D.10) is rewritten as

$$T_{\mathrm{int}} \approx 15\pi\nu N \left(\frac{\gamma}{\gamma_{\mathrm{cr}}^{\mathrm{H}}}\frac{2}{N\ln N}\right)^2 \approx \frac{60\pi\nu}{N(\ln N)^2}\left(\frac{\gamma}{\gamma_{\mathrm{cr}}^{\mathrm{H}}}\right)^2\,. \tag{D.11}$$

Eq. (D.11) is valid for large disorder regime or small coupling strength and it is in agreement with Eq. (D.4).

D.1.2.3 Dependence on coupling strength γ

In order to verify the previous analytical estimates, in the Fig. D.5–(a) we show the average integrated transmission $\langle T_{\mathrm{int}}\rangle$ multiplied by $N(\ln N)^2$ as a function of the normalized coupling strength $\gamma/\gamma_{\mathrm{cr}}^{\mathrm{H}}$, meanwhile in Fig. D.5–(b) we show the average integrated transmission $\langle T_{\mathrm{int}}\rangle$ multiplied by N as a

function of the normalized coupling strength $\gamma/\gamma_{\rm cr}^{\rm H}$ for the disorder strength $\mathrm{W} = 100$ and the system sizes $N = \{100, 400, 1000, 4000\}$ for all the states except for the ground state.

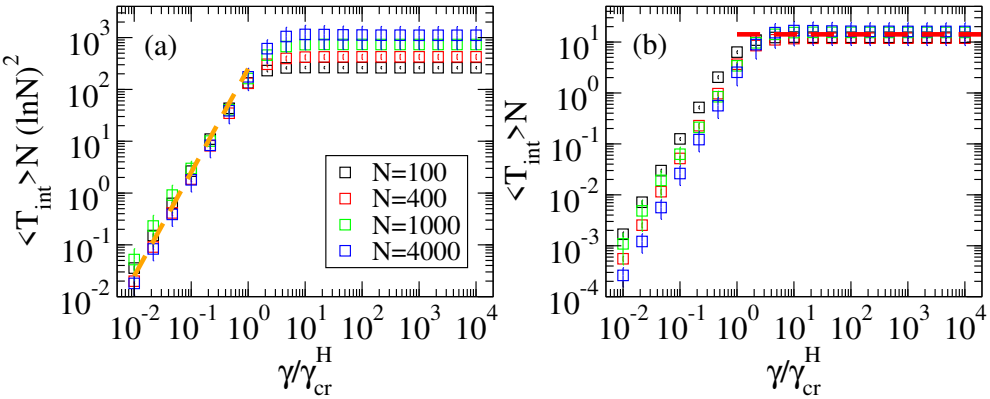

Figure D.5: (a) Average integrated transmission $\langle T_{\rm int}\rangle$ multiplied by $N(\ln N)^2$ *vs.* the normalized coupling strength $\gamma/\gamma_{\rm cr}^{\rm H}$, (b) average integrated transmission $\langle T_{\rm int}\rangle$ multiplied by N *vs.* the normalized coupling strength $\gamma/\gamma_{\rm cr}^{\rm H}$ for the disorder $\mathrm{W} = 100$. Here, we used the system sizes $N = \{100, 400, 1000, 4000\}$, the number of disorder configurations N_r is such that $N_r \times N = 10^5$, $\Omega = \nu = 1$. The horizontal dashed line indicates the Eq. (D.9) and the dashed orange line indicates the Eq. (D.11).

From Fig. D.5–(a), we can observe that the numerical results are in agreement with Eqs. (D.11) for $\gamma < \gamma_{\rm cr}^{\rm H}$. While, from Fig. D.5–(b) we observe agreement with Eq. (D.9) for $\gamma > \gamma_{\rm cr}^{\rm H}$.

D.2 Non-Hermitian case

D.2.1 Dependence on coupling strength γ: all states

In the Fig. D.6–(a) we show the average integrated transmission $\langle T_{\rm int}\rangle$ multiplied by N^2 as a function of the normalized coupling strength $\gamma/\gamma_{\rm cr}^{\rm NH}$, meanwhile in Fig. D.6–(b) we show the average integrated transmission $\langle T_{\rm int}\rangle$ multiplied by N as a function of the normalized coupling strength $\gamma/\gamma_{\rm cr}^{\rm NH}$ for the large disorder $\mathrm{W} = 100$ and the system sizes $N = \{100, 400, 1000, 4000\}$ for all the eigenstates. Recall that the critical coupling strength is $\gamma_{\rm cr}^{\rm NH} = 2\mathrm{W}/(N\pi)$.

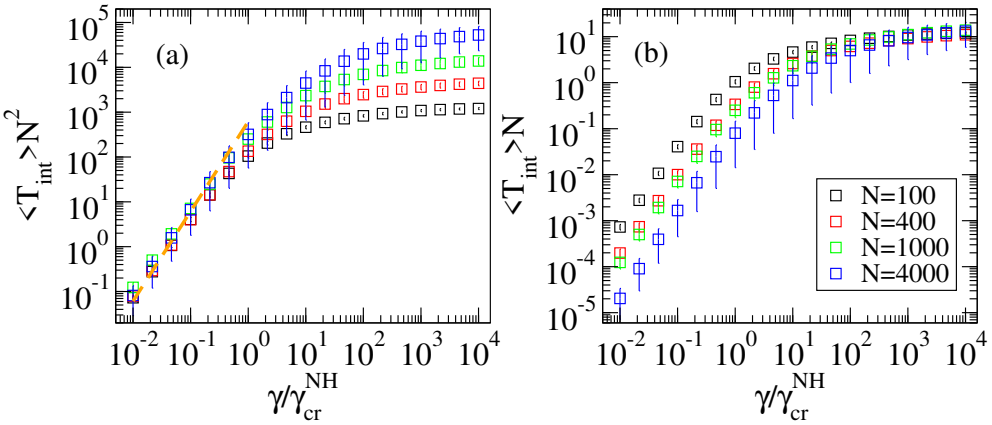

Figure D.6: (a) Average integrated transmission $\langle T_{\rm int}\rangle$ multiplied by N^2 *vs.* the normalized coupling strength $\gamma/\gamma_{\rm cr}^{\rm NH}$ and (b) average integrated transmission $\langle T_{\rm int}\rangle$ multiplied by N *vs.* the normalized coupling strength $\gamma/\gamma_{\rm cr}^{\rm NH}$ the disorder $\mathrm{W} = 100$ and the system sizes $N = \{100, 400, 1000, 4000\}$. Here, $\Omega = \nu = 1$, the number of disorder configurations N_r is such that $N_r \times N = 10^5$. The dashed orange line goes like $\left(\frac{\gamma}{\gamma_{\rm cr}^{\rm NH}}\right)^2$.

From the Fig. D.6–(a) and D.6–(b), we can establish a relation for the average integrated transmission $\langle T_{\rm int}\rangle$ for large disorder $\mathrm{W} = 100$ as follows:

$$\langle T_{\rm int}\rangle \approx \begin{cases} \dfrac{1}{N^2}\left(\dfrac{\gamma}{\gamma_{\rm cr}^{\rm NH}}\right)^2, & \gamma < \gamma_{\rm cr}^{\rm NH} \\ \dfrac{1}{N}, & \gamma \gg \gamma_{\rm cr}^{\rm NH} \end{cases} \tag{D.12}$$

Note that the above expressions are valid only for the very large disorder case. For smaller disorder, more work is needed to find the dependence of the integrated transmission $T_{\rm int}$ on the system size N.

Bibliography

[1] J. Schachenmayer, C. Genes, E. Tignone, and G. Pupillo Phys. Rev. Lett. **114**, 196403 (2015). J. Feist and F. J. Garcia-Vidal, Phys. Rev. Lett. **114**, 196402 (2015). 1, 75, 76

[2] J. Grad, G. Hernandez, and S. Mukamel, Phys. Rev. A **37**, 3835 (1988); F. C. Spano, J. R. Kuklinski and S. Mukamel, J. Chem. Phys. **94**, 7534 (1991); R. Monshouwer, M. Abrahamsson, F. van Mourik, and R. van Grondelle, J. Phys. Chem. B, **101** 7241 (1997); M. Mohseni, P. Rebentrost, S. Lloyd, and A. Aspuru-Guzik, J. Chem. Phys. **129**, 174106 (2008); G.L. Celardo et al., J. Phys. Chem. C, **116**, 22105 (2012); D. Ferrari, G. L. Celardo, G.P. Berman, R.T.Sayre, F. Borgonovi The Journal of Physical Chemistry C **118**, 20 (2014). 1

[3] E. Akkermans, A. Gero, and R. Kaiser, Phys. Rev. Lett. **101**, 103602 (2008); R. Kaiser, J. Mod. Opt. **56**, 2082 (2009); T. Bienaime, N. Piovella, and R. Kaiser, Phys. Rev. Lett. **108**, 123602 (2012); E. Akkermans and A. Gero, Euro Phys. Lett. **101**, 54003 (2013). 1, 33

[4] S. Sorathia, F.M. Izrailev, V.G. Zelevinsky, G.L. Celardo , Phys. Rev. E **86**, 011142 (2012); A. Ziletti, F. Borgonovi, G.L. Celardo , F.M. Izrailev, L. Kaplan and V.G. Zelevinsky, Phys. Rev. B **85**, 052201 (2012). 1

[5] P. Jurcevic, B. P. Lanyon, P. Hauke, C. Hempel, P. Zoller, R. Blatt, and C. F. Roos, Nature (London) **511**, 202 (2014); P. Richerme, Z.-X. Gong, A. Lee, C. Senko, J. Smith, M. Foss-Feig, S. Michalakis, A. V. Gorshkov, and C. Monroe, Nature (London) **511**, 198 (2014). 1, 35, 45, 49, 75

[6] A. F. van Loo, A. Fedorov, K. Lalumiere, B. C. Sanders, A. Blais, A. Wallraff, Science **432**, 1494 (2013). 1, 33

[7] W. Guerin, M. O. Araújo, and R. Kaiser, Phys. Rev. Lett. **116**, 083601 (2016); M. O. Araújo, I. Kresić, R. Kaiser, and W. Guerin Phys. Rev. Lett. **117**, 073002 (2016). 1, 34

[8] F. Evers and A. D. Mirlin, Rev. Mod. Phys. **80**, 1355 (2008). 2, 5, 6

[9] A. D. Mirlin, Y. V. Fyodorov, F.-M. Dittes, J. Quezada, and T. H. Seligman, Phys. Rev. E **54**, 3221 (1996). 2, 5, 6

[10] J. A. Méndez-Bermúdez, V. A. Gopar and I. Varga, Phys. Rev. B **82**, 125106 (2010). 2, 5

[11] I. Varga and D. Braun, Phys. Rev. B **61**, R11859 (2000). 2, 6

[12] Alexander D. Mirlin, Physics Reports **326**, 259 (2000). 2, 6

[13] C. Jung, M. Müller, and I. Rotter, Phys. Rev. E **60**, 114 (1999). 2, 34, 35, 40, 41, 77

[14] L. N. Cooper, Phys. Rev. **104**, 1189 (1956). 2, 35, 37, 38

[15] Nahum C. Chávez, F. Mattiotti, J.A. Méndez-Bermúdez, F. Borgonovi and G.L. Celardo, Eur. Phys, J. B **92**, 144 (2019). 2, 57

[16] G.L. Celardo, A. Biella, L. Kaplan, F. Borgonovi Fortschr. Phys. **61**, No. 2-3, 250-260 (2013); A. Biella, F. Borgonovi, R. Kaiser, G.L. Celardo, EuroPhys. Lett. **103**, 57009 (2013). 2, 5, 11, 15, 33, 49, 50, 59, 61, 70, 71, 91

[17] G. L. Celardo, R. Kaiser, and F. Borgonovi, Phys. Rev. B **94**, 144206 (2016); L. F. Santos, F. Borgonovi, G. L. Celardo, Phys. Rev. Lett. **116**, 250402 (2016). 2, 33, 35, 38, 45, 48

[18] A. D. Mirlin, Phys. Rep. **326**, 259 (2000); Y. V. Fyodorov and A. D. Mirlin, Int. J. Mod. Phys. **8**, 3795 (1994); Y. V. Fyodorov and A. D. Mirlin, Phys. Rev. B **51**, 13403 (1995). 5

[19] V. I. Falko and K. B. Efetov, Europhys. Lett. **32**, 627 (1995); Phys. Rev. B **52**, 17413 (1995). 5

[20] F. Wegner, Z. Phys. B **36**, 209 (1980); H. Aoki, J. Phys. C **16**, L205 (1983); M. Schreiber and H. Grussbach, Phys. Rev. Lett. **67**, 607 (1991); D. A. Parshin and H. R. Schober, *ibid.* **83**, 4590 (1999); A. Mildenberger, F. Evers, and A. D. Mirlin, Phys. Rev. B **66**, 033109 (2002). 5

[21] B. L. Altshuler, V. E. Kravtsov, I. V. Lerner, in *Mesoscopic Phenomena in Solids*, ed. B. L. Altshuler, P. A. Lee, and R. A. Webb (North Holland, Amsterdam, 1991). 5

[22] D. Braun, E. Hofstetter, G. Montambaux and A. MacKinnon, Phys. Rev. Lett. **64**, 155107 (2001); K. Slevin and T. Ohtsuki, *ibid.* **82**, 382 (1999); K. A. Muttalib and P. Woelfle, *ibid.* **83**, 3013 (1999). 5

[23] J. T. Chalker and G. J. Daniell, Phys. Rev. Lett. **61**, 593 (1988). 5

[24] V. E. Kravtsov and K. A. Muttalib, Phys. Rev. Lett. **79** 1913 (1997). 6

[25] V. E. Kravtsov and A. M. Tsvelik, Phys. Rev. Lett. B **62** 9888 (2000). 6

[26] E. Cuevas, M. Ortuno, V. Gasparian and A. Perez-Garrido, Phys. Rev. Lett., **88** 016401 (2001). 6

[27] I. Varga, Phys. Rev. B **66**, 094201 (2002). 6

[28] J. A. Méndez-Bermúdez, A. Alcázar-López and Imre Varga, EPL, **98**, 37006, (2012). 6, 7, 18

[29] J. A. Mendez-Bermudez, A. Alcazar-Lopez, and I. Varga, J. Stat. Mech. P11012 (2014). 6

[30] J. A. Mendez-Bermudez and T. Kottos. Phys. Rev. B **72**, 064108 (2005). 6, 76

[31] J. A. Méndez-Bermúdez, T. Kottos and D. Cohen, Phys. Rev. E **73** 036204 (2006). 6

[32] J. A. Méndez-Bermúdez and Imre Varga, Phys. Rev. B **74**, 125114 (2006) 6, 29, 30

[33] J. A. Mendez-Bermudez, V. A. Gopar, and I. Varga, Ann. Phys. (Berlin) **18**, 891 (2009). 6, 76

[34] A. Alcazar-Lopez, J. A. Mendez-Bermudez, and I. Varga, Ann. Phys. (Berlin) **18**, 896 (2009). 6

[35] J.J.M. Verbaarschot, H.A. Weidenmüller and M.R. Zirnbauer, Physics Report, **129** No.6, 367 (1985). 7

[36] G. G. Giusteri, F. Recrosi, G. Schaller, and G. L. Celardo, Phys. Rev. E **96**, 012113 (2017); G. G. Giusteri, F. Mattiotti, and G. L. Celardo, Phys. Rev. B **91**, 094301 (2015). 7, 35

[37] G.L. Celardo and L. Kaplan, Phys. Rev. B **79**, 155108 (2009). 7, 14, 53

[38] M. L. Mehta, *Random Matrices*, Elsevier, The Netherlands, 2004. 11

[39] G. L. Celardo, F. M. Izrailev, V. G. Zelevinsky and G. P. Berman, Phys. Lett. B **659**, 170 (2008). 13

[40] B. L. Altshuler, I. Kh. Zharekeshev, S. A. Kotochigova and B. I. Shklovskii, JETP **67** No. 3, 625 (1988). 14

[41] Numerical Recipes, The art of scientific computing, Third edition, William H. Press, Saul A. Teukolsky, Willian T. Vetterling, Brian P. Flannery, Cambridge University Press, pag. 781 (2007). 15, 17

[42] C. W. J. Beenakker, Random-matrix theory of quantum transport, Rev. Mod. Phys. **69**, 731 (1997). 15

[43] P. W. Anderson, Science **325** 1510, (1972). 33

[44] E. Dagotto, Science **309**, 257 (2005). 33

[45] T. Laurent, Y. Todorov, A. Vasanelli, A. Delteil, and C. Sirtori, Phys. Rev. Lett. **115**, 187402 (2015). 33

[46] V. N. Pustovit and T. V. Shahbazyan, Phys. Rev. Lett. **102**, 077401 (2009). 33

[47] J. Strumpfer, M. Sener, and K. Schulten, J. Phys. Chem. Lett. **3**, 536 (2012). 33

[48] G. L. Celardo, F. Borgonovi, M. Merkli, V. I. Tsifrinovich, and G. P. Berman, Jour. Phys. Chem. C **116**, 22105, (2012). 33, 35

[49] K. D. B. Higgins, S. C. Benjamin, T. M. Stace, G. J. Milburn, B. W. Lovett, and E. M. Gauger, Nature Communications **5**, 4705 (2014). 33

[50] G. L. Celardo, P. Poli, L. Lussardi, and F. Borgonovi, Phys. Rev. B **90**, 085142 (2014); G. L. Celardo, G. G. Giusteri, and F. Borgonovi, Phys. Rev. B **90**, 075113 (2014). 33, 43, 70

[51] U. Fano, Rev. Mod. Phys. **64**, 313 (1992). 33

[52] "Coherence in Spectroscopy and Modern Physics", Edited by F. T. Arecchi, R. Bonifacio, and M. O. Scully, Nato Advanced Study Institute on Coherence in Spectroscopy and Modern Physics, Versilia, Italy, (1977); DiRienzo A., Rogovin D., Scully M., Bonifacio R., Lugiato L., Milani M. (1978) Superconductivity and Quantum Optics. In: Arecchi F.T., Bonifacio R., Scully M.O. (eds) Coherence in Spectroscopy and Modern Physics. NATO Advanced Study Institutes Series (Series B: Physics), vol 37. Springer, Boston, MA. 33

[53] M. O. Scully and A. A. Svidzinsky, Science **325**, 1510 (2009). 33

[54] R Monshouwer, M Abrahamsson, F Van Mourik, R Van Grondelle, The Journal of Physical Chemistry B **101**, 7241 (1997). 34

[55] V. V. Sokolov and V. G. Zelevinsky, Phys. Lett. B **202**, 10 (1988); I. Rotter, Rep. Prog. Phys. **54**, 635 (1991). 35

[56] J. von Delft, Annalen der Physik **3**, 219 (2001); A. Faribault, P. Calabrese and J. S. Caux, Phys. Rev. B **77**, 064503 (2008); R. A. Smith and V. Ambegaokar, Phys. Rev. Lett. **77**, 24 (1996); M. Schechter, J. von Delft, Y. Imry and Y. Levinson, Phys. Rev. B **67**, 064506 (2003); E. A. Yuzbashyan, A. A. Baytin, and B. L. Altshuler, Phys. Rev. B **71**, 094505 (2005). 35, 36, 38

[57] H. K. Owusu, K. Wagh, and E. A. Yuzbashyan, J. Phys. A: Math. Theor. **42**, 035206 (2009); E. A. Yuzbashyan and B. S. Shastry, Jour. of Stat. Phys. **150**, 704 (2013). 35, 36, 37, 38

[58] G. L. Celardo, V. G. Zelevinsky, F. Izrailev, and G. P. Berman, Phys. Rev. E **76** 031119 (2007); G. L. Celardo, N. Auerbach, F. M. Izrailev, and V. G. Zelevinsky, Phys. Rev. Lett. **106**, 042501 (2011); S. Sorathia, F. M. Izrailev, G. L. Celardo, V. G. Zelevinsky, G. P. Berman, EPL **88**, 27003 (2009). 35

[59] J. R. Schrieffer, Theory of superconductivity, Westview Press (1964); "Superconductivity of Metals and Alloys" G. De Gennes, p 93, Addison-Wesley Publishing Company (1966). 35, 37, 38

[60] G. A. Álvarez, et al. J.Chem.Phys. **124**, 194507 (2006); HM Pastawski, Physica B: Condensed Matter **398**, 278 (2007); AD Dente, RA Bustos-Marún, HM Pastawski, Phys. Rev. A **78**, 062116 (2008); A. Ruderman et al., J. Phys.: Condens. Matter **27** 315501 (2015). 44

[61] M. Gullì, A. Valzelli, F. Mattiotti, M. Angeli, F. Borgonovi and G. L. Celardo, New J. Phys. **21** 013019 (2019) 47, 49, 75

[62] P. W. Anderson, Phys. Rev. **109**, 1492 (1958). 49

[63] P.A. Lee and T.V. Ramakrishnan, Rev. Mod. Phys. **57**, 287 (1985) 50

[64] D. J. Thouless, in *Ill-Condensed Matter*, edited by R. Balian, R. Maynard, and G. Toulouse (North-Holland, Amsterdam, 1979). 50

[65] F. M. Izrailev, S. Ruffo and L. Tessieri, J. Phys. A: Math. Gen. **31**, 5263 (1998). 50, 60

[66] S. Datta, *Quantum Transport: Atom to Transistor*. Cambridge: Cambridge University Press. (2005). doi:10.1017/CBO9781139164313 54

[67] V.V. Sokolov, I. Rotter, D.V. Savin and M. Müller, Phys. Rev. C **56**, 1031 (1997). 63

[68] A. J. Mártinez-Mendoza, J. A. Méndez-Bermúdezz, and I. Varga, AIP. Conf. Proc. **1319**, 41 (2010). 76

[69] J. Yuen-Zhou, D. H. Arias, D. M. Eisele, C. P. Steiner, J. J. Krich, M. G. Bawendi, K. A. Nelson and A. Aspuru-Guzik, ACS Nano **8**, 5527 (2014); D. M. Eisele et. al., Nature Chemistry **4**, 655 (2012). 76

[70] G. Raino, M. A. Becker, M. I. Bodnarchuk, R. F. Mahrt, M. V. Kovalenko and T. Stoferle, Nature **563**, 671 (2018). 76